Pablo Cueto Corral

Propeller Slipstream Characterisation by Large-Scale PIV

An experimental study for Isolated Propeller and Propeller-Wing Interaction

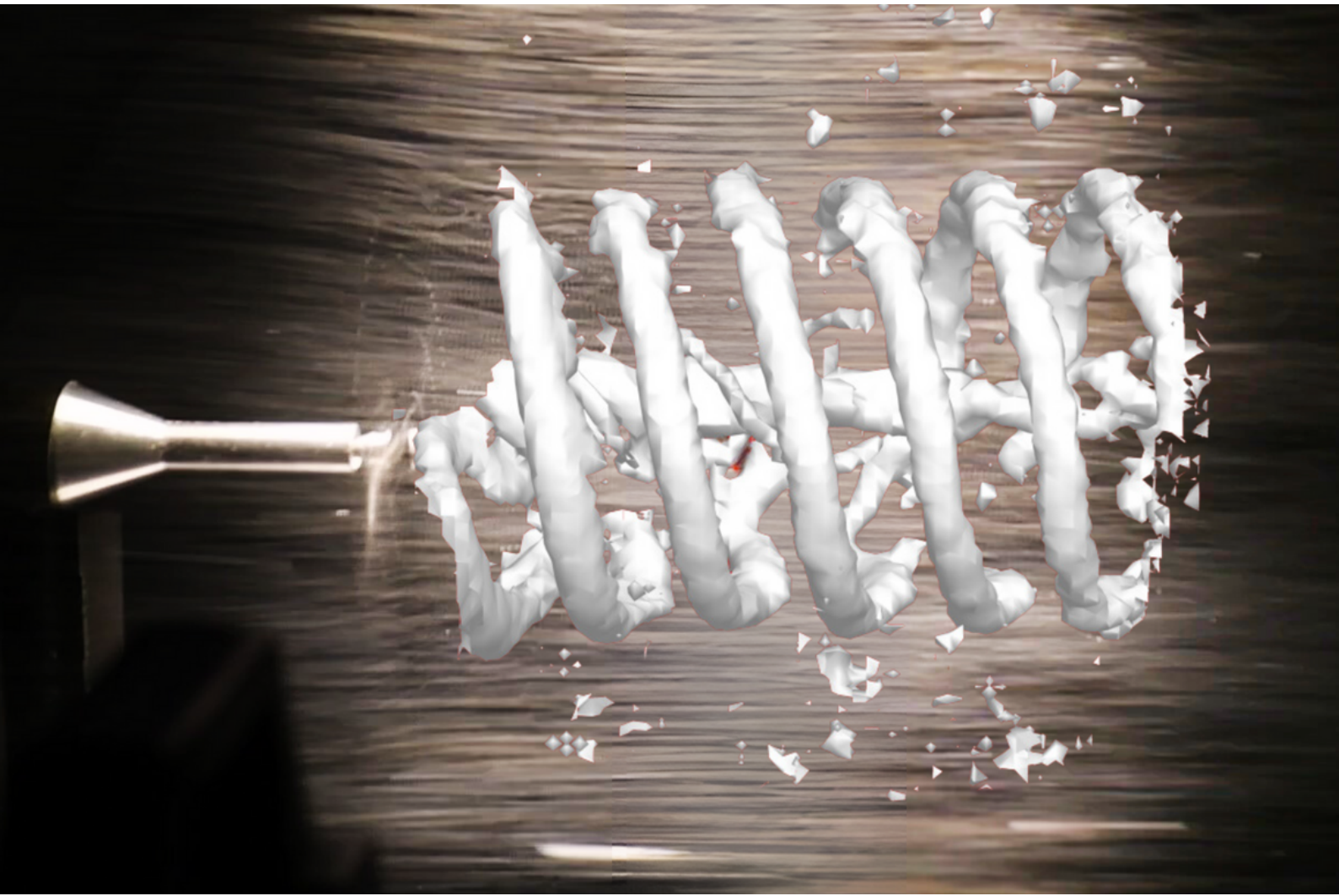

Propeller Slipstream Characterisation by Large-Scale PIV

An experimental study for Isolated Propeller and Propeller-Wing Interaction

Thesis report

by

Pablo Cueto Corral

to obtain the degree of Master of Science
at the Delft University of Technology
to be defended publicly on December 14, 2023 at 9:00

Student number:	5604451
Project Duration:	February, 2023 - December, 2023
Thesis committee:	
Chair:	Prof.dr. F. Scarano
Supervisors:	Dr. A. Sciacchitano
External examiner:	Dr.ir. T. Sinnige

An electronic version of this thesis is available at `http://repository.tudelft.nl/`.

Faculty of Aerospace Engineering · Delft University of Technology

Preface

This thesis marks the end of probably the toughest journey I have embarked on, but also the most rewarding. With this in mind, there are some people that I would like to thank who allowed me to get to the point where I am now.

First and foremost, I would like to thank my family. More specifically, my mom, Maria Mercedes, who was the one that initially pushed me towards this adventure. My dad, Alberto, who was there along the way, helping make my life easier so that I could focus on what mattered. My sister Cristina, with whom I can always count no matter the day or time. And my Grandparents, Vicentina and Rafael, who are the sole reason I am here to begin with.

Secondly, I would like to thank my friends, without whom the way here would not have been worth it. At highs on Thursday Bouwpubs, or though times before big deadlines, we always had a good time and made the best out of every situation.

I want to extend an extra mention to my Aero peeps, who were the key to even surviving the first year of this incredible challenge.

Last but not least, I would like to thank my supervisor, Andrea, who guided me through this project. He was always there to answer my questions and shared the excitement with me on every milestone we achieved.

Pablo Cueto Corral
Delft, December 2023

Abstract

This study explores the flowfield around a pusher propeller-wing configuration using Lagrangian Particle Tracking (LPT). It assesses LPT's capability to characterise propeller-wing interactions, emphasising its ability to resolve complex flow dynamics.

The experiment successfully achieves high particle concentrations downstream of the propeller, with propeller rotation enhancing the uniformity of the particle distribution. Velocity measurements are precise and feature low uncertainty, and vortex dynamics shed by the propeller are effectively resolved.

Furthermore, the study confirms LPT's robustness in characterising wing-propeller flow characteristics, particularly in thrust and torque calculations, highlighting its non-invasive nature for performance measurements.

The investigation reveals how the wing influences the slipstream's vortex structure and identifies the pylon's effects. The method captures the propeller-induced effects on the wing, providing insights into upwash, downwash, and angle of attack variations.

In conclusion, this research demonstrates the utility of LPT in comprehensively characterising propeller-wing interactions, offering valuable insights for aviation and propeller innovations.

Contents

Nomenclature

Abbreviations

Abbreviation	Definition
AoA	Angle of Attack
DVR	Dynamic Velocity Range
DSR	Dynamic Spatial Range
HFSB	Helium Filled Soap Bubbles
LPT	Lagrangian Particle Tracking
PIV	Particle Image Velocimetry
ppp	Particles per Pixel
rms	Root Mean Square
STB	Shake-The-Box
VIC	Vortex In Cell

Symbols

Symbol	Definition	Unit
A	Area of Actuator Disc	[m^2]
C	Particle Concentration	[Particles/m^3]
C_p	Power Coefficient	[-]
C_Q	Torque Coefficient	[-]
C_t	Thrust Coefficient	[-]
D	Propeller Diameter	[m]
d_P	Particle Diameter	[m]
E	Voxel Intensity	[-]
F	Force	[N]
F_f	Acting Force on the Fluid	[N]
g	Gravity Acceleration	[m/s^2]
J	Advance Ratio	[-]
l	Bin Size	[mm]
L	Length of Field of View	[m]
L^2_{inj}	Area of Seeding Rake	[m^2]
M	Magnification Factor	[-]
M	Propeller Thrust	[N]
n	Rotational Velocity	[rps]
n	x Component of Velocity	[m/s]
P	Power	[W]
P_i	Ideal Power	[W]
p	Pressure	[Pa]

Symbol	Definition	Unit
p_0	Pressure at Freestream	[Pa]
p_e	Pressure Far Downstream of Actuator Disc	[Pa]
Q	Propeller Torque	[Nm]
Q	Q Criterion	[-]
R	Propeller Radius	[m]
Re	Reynolds Number	[-]
T	Period	[s]
t	Time	[s]
u	Velocity	[m/s]
u	x Component of Velocity	[m/s]
u	Velocity	[m/s]
u_0	Freestream Velocity	[m/s]
u_b	Velocity at Actuator Disc	[m/s]
u'_b	Induced Velocity at Actuator Plane	[m/s]
u_e	Exit Velocity from the Streamtube	[m/s]
u'_e	Induced Velocity Far Downstream of Actuator Disc	[m/s]
u_h	Velocity Determined Through Radial Basis Functions	[m/s]
u_{ax}	Axial Velocity	[m/s]
u_p	Velocity of Particle	[m/s]
u_θ	Tangential Velocity	[m/s]
u_max	Maximum Velocity	[m/s]
u_{ax}	Axial Velocity	[m/s]
V	Velocity	[m/s]
V	Volume	[m^3]
V	Velocity	[m/s]
x	Position of Particle	[m]
x_p	x Coordinate from Propeller Hub	[m]
x	x Component of Velocity	[m/s]
z_p	z Coordinate From Propeller Hub	[m]
$\mathbf{n}$	Normal Unit Vector	[-]
$\dot{N}$	Particle Production Rate	[Particles/s]
α	Wing's Angle of Attack	[°]
β	Pitch Angle	[°]
δ_z	Focal Depth	[m]
η	Efficiency	[-]
η_P	Propeller Efficiency	[-]
θ	Angle Between Cameras	[°]
θ_{sw}	Swirl Angle	[°]
λ	Wavelength of Light	[m]
μ	Dynamic Viscosity	[N s/m^2]
ρ	Air Density	[kg/m^3]
ρ	Ratio Between the Cross-sectional Area of the Seeding Rake and the Cross-sectional Area of the Seeded streamtube	[-]
ρ_f	Fluid Density	[kg/m^3]

Symbol	Definition	Unit
ρ_P	Particle's Density	[kg/m^3]
σ_u	Root Mean Square of Velocity	[m/s]
$\sigma_{\Delta X}$	Root Mean Square of Displacement Error	[m]
$\bar{\tau}$	Viscous Stress	[N/m^2]
τ_P	Particle Time Response	[-]
ϕ	Inflow Angle	[°]
ω	Propeller's Rotational Velocity	[RPM]
ω_h	Vorticity within Cell	[1/s]
ω_{v}	Vorticity	[1/s]

1 Introduction

If global aviation were a country, it would rank among the top ten greenhouse gas emitters [1]—the reason why there is a need to find more environmentally friendly solutions for this sector. As part of the European initiative to achieve climate neutrality by 2050, a mid-term goal has been set to reduce greenhouse gas emissions by 55% by 2030 with respect to the 1990 emissions [1]. Although only a small portion of the emissions is produced by it currently (5.2% in 2019 in Europe[2]), it is promised to keep growing steadily, directly affecting the aviation industry. To comply with these requirements, newer technologies are being investigated. Among the alternatives, the two most important for this research are electric propulsion and enhancing aerodynamic efficiency to reduce drag.

Although propellers have been around since the beginning of aviation, propeller propulsion interest had a decay with the invention of the jet engine. Nevertheless, it is currently a main research area as part of sustainability goals. Due to the higher efficiencies that propeller-based propulsion has at low to medium speeds compared to jet engines, it presents a great potential to reduce emissions for short-haul and regional flights. New propeller configurations are being tested, such as tail-mounted propellers and tip-mounted propellers [3][4]. However, to better understand aircraft behaviour with propeller propulsion, it is important to have insight into propeller performance at a certain configuration and wing-propeller interaction.

So far, computational methods have been the main resource to reconstruct a flowfield around a propeller fully. These methods provide a great spatial resolution and give a general idea of how the flow will behave, but results must be validated with some experimental data. On the other hand, experimental methods to measure velocities, such as Hot Wire Anemometry or Laser Doppler Velocimetry, only offer point-like spatial resolution, which makes reconstruction of the flowfield a tedious process. Moreover, load cells and balances must be used to measure propeller performance. This is not only a tedious process, but it increases the costs involved in manufacturing a wind-tunnel model. With the introduction of Particle Image Velocimetry (PIV), the ability to reconstruct velocity flowfields experimentally improved, being able to resolve velocities in a plane at high spatial resolution.

More recently, the introduction of large-scale PIV using Helium Filled Soap Bubbles (HFSB) [5] and Lagrangian Particle Tracking (LPT) with methods such as the Shake-The-Box method [6], opens the possibility to reconstruct larger flow fields around complex objects fully. So far, these methods have been tested reconstructing large flow fields around objects such as a full-size cyclist [7] and a hinged folding wingtip [8]. Moreover, it has been proven that object

forces can be extracted based on PIV measurements and a control volume approach based on conservation of momentum[9] [10]. However, the potential use of this technique around propeller flow is yet to be tested, which is the main drive of this research. The specific research questions and objectives will be further discussed later in this chapter.

As part of the initiative to reduce emissions, the Delft University of Technology is aiming to perform research on a Cessna Skymaster 337 flying testbed (see Figure 1.1). This aircraft has a unique configuration of two inline propellers, which create a particular flow between the pushing propeller and the horizontal tailplane. Moreover, it has the opportunity to be converted to electric, as has been demonstrated by Ampaire [11] and Voltaero [12]. Additionally, the unique configuration of propellers causes the aircraft to behave in a particular way. All of the above make the aircraft an ideal testbed for several areas of investigation.

Figure 1.1: Cessna 337D Skymaster. Recovered from Herzog [13].

The main objective of this research is to reconstruct the flow field around a pusher propeller-wing configuration that resembles a 1:10 scaled-down version of the horizontal tailplane and pusher propeller of the Cessna 337 Skymaster. The reconstruction is proposed to employ Lagrangian Particle Tracking in a wind tunnel environment. The research aims to give a first impression of the method's capabilities at a smaller scale, to be later carried in the full-size aircraft.

With this objective in mind, the following research questions are posed. Two main questions are formulated with several sub-questions that are to be answered through an experimental campaign around the aforementioned scaled-down model:

Q I. *To what extent can the Lagrangian Particle Tracking method characterise a propeller-wing interaction flow?*

- **Q** I.i. What particle concentration can be achieved after the propeller?
- **Q** I.ii. What is the velocity resolution achieved for a wing-propeller configuration?
- **Q** I.iii. Can the vortex dynamics shed by the propeller be resolved?

Q II. *How robust is the method to characterise wing-propeller flow characteristics?*

- **Q** II.i. How accurate is load determination through the control volume approach based on LPT method, compared to other methods?
- **Q** II.ii. Can the wing's induced effects be observed on the vortex structure through the LPT measurements?
- **Q** II.iii. Can the propeller's induced effects on the wing be observed through the LPT measurements?

The structure of the report is as follows. First, a literature study on propeller flow characteristics and wing propeller interaction will be reviewed in chapter 2. Second, the working principles of Particle Image Velocimetry and all the subsequent methods used in this research will be addressed in chapter 3. Third, the methodology and experimental setup will be explained in chapter 4. Fourth, the results from the experimental campaign will be presented and discussed in chapter 5. Finally, the research conclusions and further recommendations for future work will be discussed in chapter 6.

2

Propeller Aerodynamics & Vortex Breakdown

Propellers have been in aviation since the Wright Brothers took off in 1903 with the first flight. To this date, propellers remain relevant as propulsion devices due to certain advantages over jet engines. In this chapter, an overview of propeller aerodynamics will be discussed. Starting with the working principle of an isolated propeller in section 2.1. Followed by the general characteristics of the propeller slipstream, including the basics of the actuator disc theory in section 2.2. The fuselage-propeller and wing-propeller interaction effects will be reviewed in section 2.3. Finally, section 2.4 will give an insight into vortex breakdown.

2.1. Working principle of isolated propeller

A propeller is a device capable of converting power from a driving engine to the fluid surrounding it by producing an axial force. As a reaction, thrust is produced in the desired direction, and propulsion is achieved. The consequence of this energy transition on the fluid is an acceleration behind the propeller and vortices created at the tips and roots of the blades. Both factors will greatly influence any surface located downstream of the propeller.

In this case, propeller design is outside the project's scope, so design characteristics such as the chord, angle of attack (AoA) and twist angle distribution of the blade will not be looked upon in detail. The general performance of the propeller is of greater interest; for such, specific parameters can be varied in the operating environment. The main parameters are listed below in Table 2.1.

Table 2.1: Operating parameters of propeller

Parameter	**Symbol**	**Units**
Rotational velocity	n	rps
Flow velocity	u_0	m/s
Diameter of the propeller	D	m
Air Density	ρ	kg/m^3
Pitch angle	β	$^\circ$
Thrust	T	N
Torque	Q	Nm
Power	P	W

Using these variables, a dimensional analysis can be done to obtain certain parameters commonly used to compare the performance between propellers. These are the thrust coefficient, power coefficient and torque coefficient, displayed in equations 2.1, 2.2 and 2.3 respectively[14].

$$C_T = \frac{T}{\rho n^2 D^4} \qquad (2.1) \qquad C_P = \frac{P}{\rho n^3 D^5} \qquad (2.2) \qquad C_Q = \frac{Q}{\rho n^2 D^5} \qquad (2.3)$$

In addition to these three parameters, the advance ratio is commonly used to characterise and compare propellers. The advance ratio represents the distance travelled by the propeller in one revolution, non-dimensionalised by the propeller diameter. The expression for the advance ratio is presented in Equation 2.4.

$$J = \frac{u_0}{nD} \qquad (2.4)$$

Finally, the propeller's efficiency can be calculated as the ratio between the propulsive power produced by the propeller and the power received from the engine, arriving at an expression dependent on the increase in velocity of the fluid induced by the propeller (ΔV): Equation 2.5 [4]. From this expression, it can be noted that the efficiency can be increased by raising the velocity variation induced by the propeller, which also increases the mass ratio.

$$\eta_\mathrm{p} = \frac{2}{2 + \Delta V / u_0} \qquad (2.5)$$

2.2. Isolated propeller slipstream characteristics

2.2.1. Actuator disc theory

A simple yet very useful approach to model a propeller is the actuator disc theory. In this theory, the propeller is modelled as an infinitely thin disc that generates a pressure jump in the flow. This model is a simple way to explain the acceleration of fluid at the slipstream of the propeller. For this model the following assumptions are made [15]:

- There is no rotation imparted to the flow.
- Thrust is uniformly distributed across the disc.
- Flow is incompressible.
- There is no work imparted to the fluid outside the propeller streamtube (has constant stagnation pressure)
- The pressure far in front and far behind the disc matches the ambient pressure.

Figure 2.1 gives a graphical representation of the actuator disc model. Applying conservation of momentum on the control volume, the force (in this case propeller thrust) can be calculated as it is the only acting force on the fluid:

$$F_f = \iint_S (\rho \mathrm{V} \cdot \mathbf{n}) \mathrm{V} dS \qquad (2.6)$$

Since it is known that the pressure everywhere on the control volume is balanced, then the only force acting is due to change in momentum flux across the boundaries. Thus the thrust can be calculated as the change in momentum flux between the boundaries:

$$T = \dot{m}(u_e - u_0) \qquad (2.7)$$

Where u_e is the exit velocity from the streamtube, u_0 is the flow velocity and $\dot{m}$ is the mass flux through the disc. With the power defined as the force kinetic energy imparted to the flow:

$$P = \dot{m} * \left(\frac{u_e^2}{2} - \frac{u_0^2}{2} \right) \tag{2.8}$$

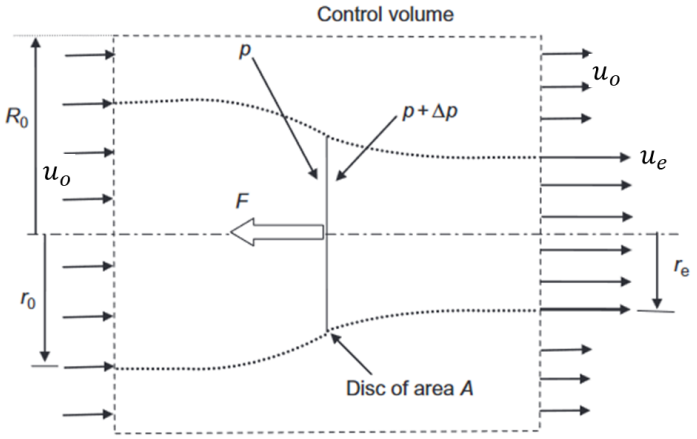

Figure 2.1: Actuator disc theory representation for propeller [15].

By combining equations 2.8 and 2.7 one arrives to a new expression for the power:

$$P = \frac{1}{2} T \left(u_e + u_0 \right) \tag{2.9}$$

Since viscous effects are neglected the power on the fluid is equal to the work done by the propeller:

$$P = T * u_b \tag{2.10}$$

With u_b the velocity at the actuator disc. Taking equation 2.10 and 2.9, it is possible to see that the velocity at the disc is equal to the average between the ones far upstream and far downstream:

$$u_b = \frac{1}{2} \left(u_e + u_0 \right) \tag{2.11}$$

It is possible to represent the velocities at the disc and at the exit as the inlet velocity plus an induced velocity:

$$u_b = u_0 + u_b' \tag{2.12}$$

$$u_e = u_0 + u_e' \tag{2.13}$$

With u_b' and u_e' the induced velocities at the actuator plane and far downstream respectively. Taking the definition of u_b from Equation 2.11 and equations 2.12 and 2.13 leads to:

$$u_e' = 2u_b' \tag{2.14}$$

Which means that the induced velocity far downstream of the actuator disc corresponds to double the one induced at the actuator disc.

Since the ideal power needed to make the disc proceed through the air at a constant speed u_0 is $P_i = T * u_0$. The efficiency can be expressed as:

$$\eta = \frac{P_i}{P} = \frac{1}{1 + \frac{u_b'}{u_0}} \tag{2.15}$$

The thrust at the actuator is due to the pressure difference and as such can be expressed as:

$$T = \Delta p * A \tag{2.16}$$

With Δp and A the pressure jump and the area of the disc respectively. Since the flow is incompressible it is possible to apply Bernoulli's equation in front and behind of the disc. That leads to:

$$\begin{aligned} p_0 + \frac{1}{2}\rho u_0^2 &= p + \frac{1}{2}\rho u_b^2 \\ p_e + \frac{1}{2}\rho u_e^2 &= p + \Delta p + \frac{1}{2}\rho u_b^2 \end{aligned} \tag{2.17}$$

Which means can be used to calculate the pressure jump as:

$$\Delta p = \frac{1}{2}\rho \left(u_e^2 - u_0^2\right) \tag{2.18}$$

Which can be replaced in Equation 2.16 to obtain the following expression for the thrust.

$$F = 2\rho A u_b' \left(u_0 + u_b'\right) = \frac{1}{2}\rho A u_0^2 \left[4\frac{u_b'}{u_0}\left(1 + \frac{u_b'}{u_0}\right)\right] \tag{2.19}$$

Then it is possible to introduce the non-dimensional thrust coefficient as a function of the induced velocity:

$$C_{\mathrm{T}} = \frac{F/A}{\frac{1}{2}\rho u_0^2} = 4\frac{u_b'}{u_0}\left(1 + \frac{u_b'}{u_0}\right) \tag{2.20}$$

In the same way it is possible to introduce a power coefficient for the actuator disc theory:

$$C_{\mathrm{P}} = \frac{P}{\frac{1}{2}\rho A u_0^3} = C_{\mathrm{T}}\left(1 + \frac{u_b'}{u_0}\right) = \frac{1}{2}C_{\mathrm{T}}\left(1 + \sqrt{1 + C_{\mathrm{T}}}\right) \tag{2.21}$$

Using the actuator disc model gives an axial velocity and pressure distribution in the streamtube as depicted in Figure 2.2.

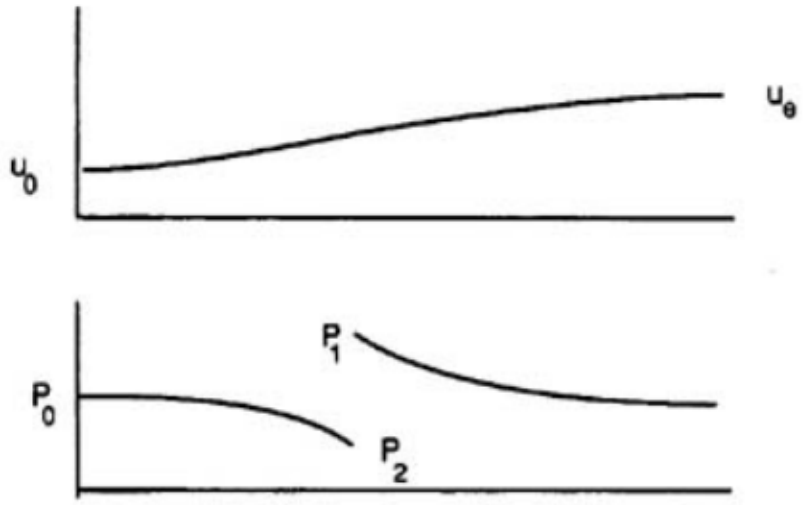

Figure 2.2: Actuator disc theory velocity profile and pressure distribution along the streamtube [16].

2.2.2. Propeller slipstream characteristics

A propeller creates a helical vortex system in its slipstream comprised of a root vortex and blade vortices that roll up into a helical structure. This creates substantial self-induced velocity gradients on the propeller. The general characteristics of the slipstream can be seen in Figure 2.3. Some general characteristics of the propeller slipstream will be explained independently, as explained by Veldhuis [17] in the following subsections.

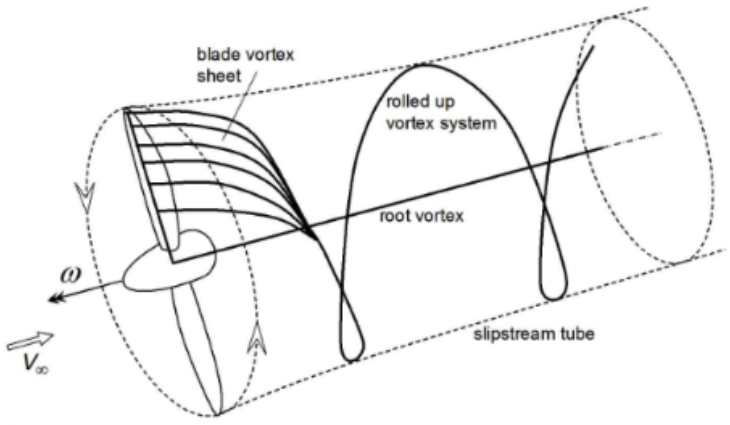

Figure 2.3: Helical vortex system of propeller slipstream [17].

Axial velocity profile

Propeller loads are not evenly distributed along the blade's span, creating a gradient of axial velocity behind the blade. A maximum axial velocity value is usually found at around $\frac{3}{4}R$ of the blade and low velocity close to the root. The typical axial velocity profile is depicted in Figure 2.4 along with the tangential velocity profile, static and total pressure directly behind the blade.

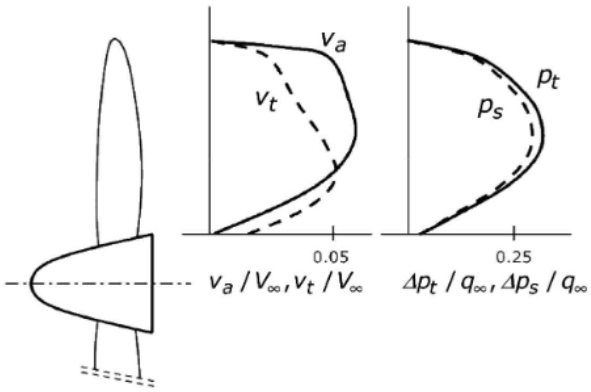

Figure 2.4: Typical distribution of axial and tangential velocity profile and static and total pressure directly behind, a 6-bladed lightly loaded propeller. BEM Analysis [17].

Swirl velocity profile

The bound vortices induce only tangential velocity (often called "swirl velocity") on the slipstream but no axial velocity. This effect can be explained by taking a simple model of infinite number of blades, as it is considered in the actuator disc model. The axial velocity induced at a point by the bound vortex is opposite and has the same magnitude as the one induced by the blade opposite to that point. Such that they cancel each other out, and the induced velocity is zero. The tangential velocity, however, is induced in the same direction by every blade, which creates a tangential velocity in the slipstream in the direction of the propeller rotation. This can be better understood when looking at Figure 2.5, where the induced axial velocities induced at point **P** by the blades **OS** and **OR** (that are evenly spaced from **OQ**) have the exact same magnitude but opposite direction. However, the induced tangential velocities by the bound vortices go in the same direction.

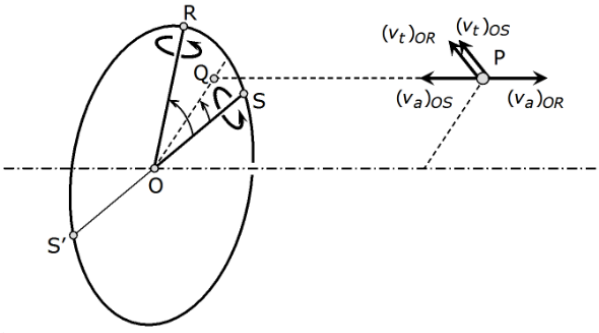

Figure 2.5: Axial and tangential velocities induced by the propeller bound vortices on the slipstream[17].

Different from the axial velocity profile with the same shape for different advance ratios, the tangential velocity profile behind the blade can vary greatly depending on the load condition of the propeller. Additionally, the swirl angle as defined in Equation 2.22 will vary in the axial direction. All this will affect the effective angle of attack of the wing behind depending on the latter's distance from the propeller's plane. The change in the angle of attack occurs because although the swirl velocity stays constant in the axial direction, due to induced velocities of

both free and bound vortices, the induced axial velocity increases along the axial direction.

$$\theta_{sw} = \tan^{-1}\left(u_\theta / u_{\text{ax}}\right) \tag{2.22}$$

Vorticity

The flow is often treated as a steady flow, so the vorticity originally confined is spread over the entire slipstream domain. However, to characterise unsteady loads on the trailing wing behind a propeller, the time-dependent position of the vortex sheets needs to be determined. This is due to the dependency of the vorticity on the blade loading and position in time.

Each blade will produce its own vortex sheet with different strengths and distribution. A high vorticity value is usually found at the tip region where the loading gradients are the highest. An important remark is that the vorticity distribution is axis-symmetrical in the x-vorticity around the propeller but not in the y and z-vorticity components.

2.3. Propeller interaction

Two main interactions will be evaluated in this section. Firstly, the effect of the fuselage on the propeller performance will be studied. Secondly, the interaction of the horizontal tail plane with the propeller slipstream will be discussed, as well as its similarities to a wing-mounted propeller.

An isolated propeller is a useful concept for studying propeller performance, but it is rarely encountered on airframes. Propellers will almost always encounter certain interactions with the airframe or engine that will affect how the propeller performs by creating an adverser inflow condition. Hence, understanding how the propeller behaves with certain non-uniform flow conditions becomes of interest. Some typical cases encountered in general aviation aircraft are depicted by van Arnhem et al. [18] in Figure 2.6.

For this study, the relevant cases are the wing-mounted propeller and the fuselage-mounted pusher propeller. Fuselage-propeller interaction will be discussed in subsection 2.3.1, and wing-propeller interaction will be discussed in subsection 2.3.2.

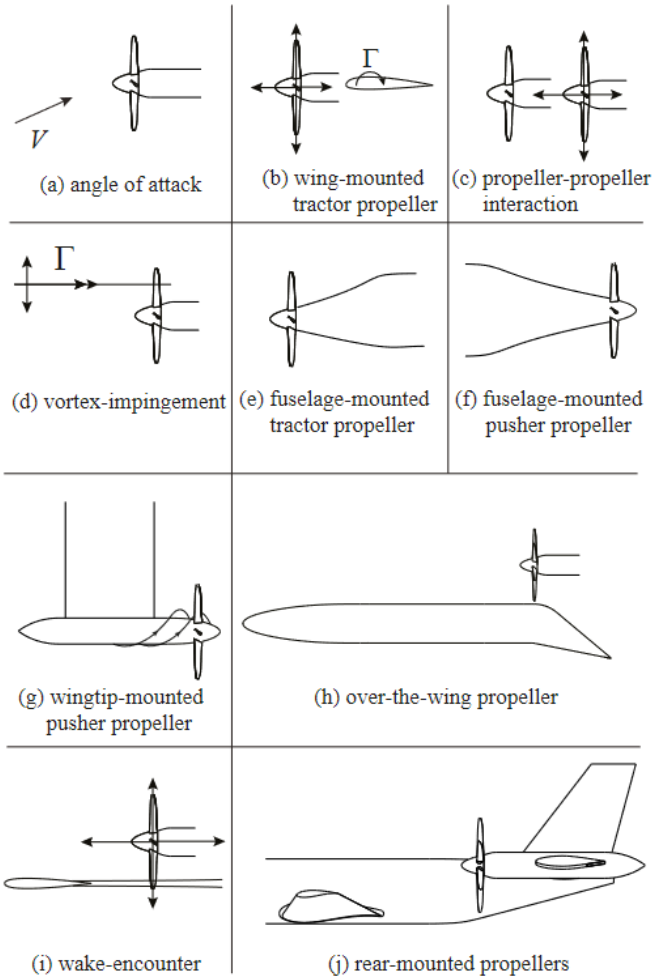

Figure 2.6: Typical cases of propeller non-uniform flow [18].

2.3.1. Fuselage-Propeller Interaction

Although at first sight, the presence of the fuselage could appear negative for the propeller's performance, studies performed in the aerodynamics of a Cessna Skymaster by Thompson [19] show that the effect is the opposite. Single-engine climb and flight performance are superior with the rear propeller than with the front one. Thompson attributes this increased performance to three main factors. Firstly, when looking at the momentum theory of a propeller, it can be seen that a slower inflow velocity will create more thrust, which is the case for the pusher propeller. Secondly, the rear propeller's slipstream is almost clear of any surface, which is explained when looking at a Blade Element Analysis method. When decreasing the axial velocity the inflow angle defined as $\phi = arctan(\frac{u_0}{2\pi * R})$ with R and u_0 the radius of the propeller and the flow velocity respectively, decreases. Which in fact increases the angle of attack that the blade experiences, calculated as $\alpha = \beta - \phi$ with β the pitch angle. The increase in thrust happens considering that the pitch of the propeller is the same as for the front one. Thirdly, the rear propeller tends to make the flow stay closer to the surface on the blunt part of the aft end of the fuselage (see Figure 2.7), thus avoiding flow separation and reducing the fuselage drag. These effects were also studied for pusher configurations by Campbell and Hollingworth [20], later confirmed with more modern geometries present on uncrewed aircraft by Figat and Piątkowska [21].

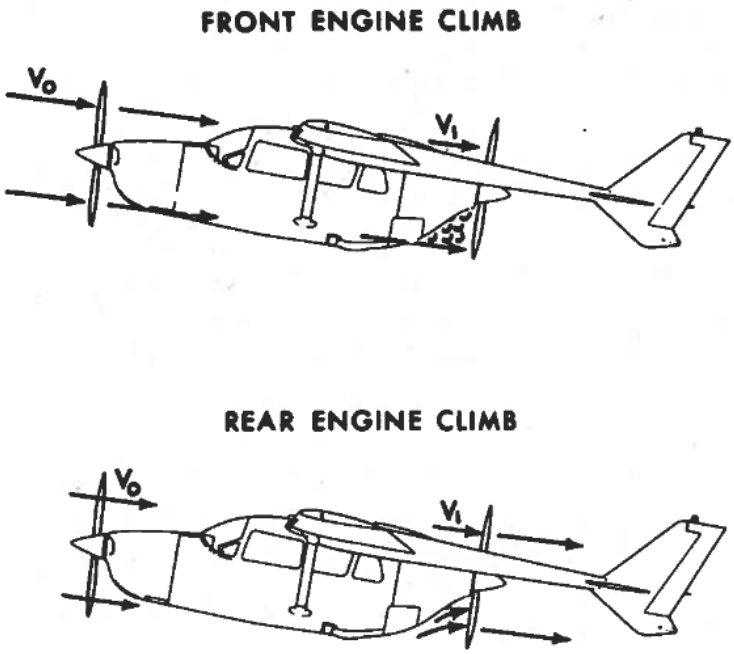

Figure 2.7: One engine climb flow on Cessna Skymaster[19].

2.3.2. Wing-propeller interaction

The vortex system created by the propeller will have a great effect on the wing located behind it. Garmann and Visbal [22] studied the interaction between a tip vortex and a NACA0012 wing at $\alpha = 8°$, which could be assimilated to the propeller wing condition. The vortex interacting with the wing affects the pressure distribution on the surface, which creates a response on the boundary layer. There, despite experiencing an increased effective angle of attack due to the upwash on one side of the vortex, the extent of the separation bubble is reduced. This counter-intuitive response from the boundary layer is a response of earlier transition that promotes reattachment of the laminar separation. On the other side of the vortex, the wing experiences a downwash; here, the flow remains laminar and attached for a longer streamwise distance than in the baseline case without the vortex (Figure 2.8). The effect of the separation can also be seen on the pressure side of the airfoil, on the side that is generating upwash where separation is only visible in the regions away from the vortex. This is compared to the baseline case, where separation is seen at the wing's trailing edge throughout the span.

On the other hand, the effect of the wing on the vortex is a spiral breakdown ahead of the wing. Additionally, the flow decelerates and reverses just upstream of the wing at $x/c = -0.35$. Consequently, there is a slight expansion of the vortex core in the iso-surface time-averaged total pressure. The vortex evolves to a winding structure for the spiral type breakdown [22]. Vortex breakdown will be further discussed later in this chapter.

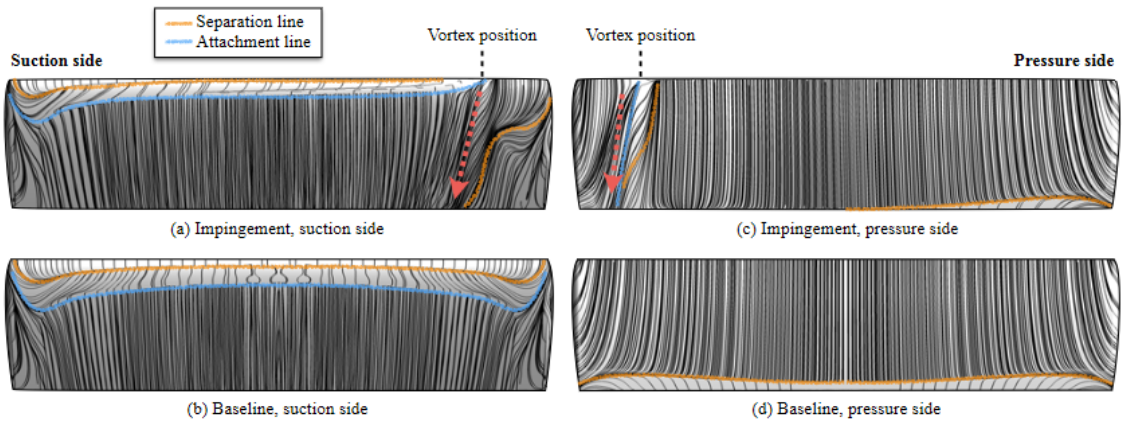

Figure 2.8: Surface streamlines of NACA0012 wing at $\alpha = 8°$[22].

As previously mentioned, the axial position of the wing with respect to the propeller will affect how it performs, which makes it an important factor. Typical position values are shown in Table 2.2 as stated by [17]. The coordinate axis for reference is presented in Figure 2.9.

Table 2.2: Typical values of propeller position relative to the wings leading edge[17].

Value	Typical Value
x_p/R	$0.81 \leftrightarrow 1.56$
z_p/R	$-0.25 \leftrightarrow 0.42$

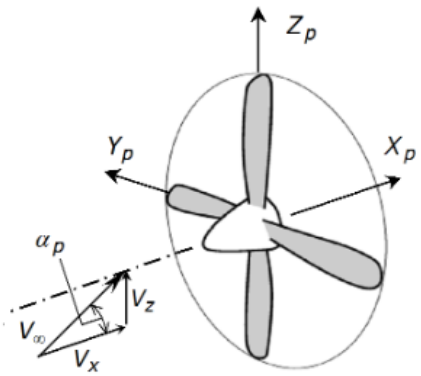

Figure 2.9: Propeller Coordinate System [17].

On a standard wing-mounted propeller configuration, the wing significantly affects the loads of the propeller blade, impacting the effective angle of attack experienced by the blade, which varies when the blade is going up or down. However, this effect is highly influenced by the wing's angle of attack, creating an induced velocity upstream of the airfoil. This consequence has a more significant effect on cambered airfoils than on symmetrical airfoils..

Furthermore, the effect that the propeller slipstream has on the wing is far more significant than its counterpart. The effects experienced will be greater when the propeller is highly loaded and at a high wing angle of attack. The induced velocity and pressure jumps mentioned above affect the wing's lift. The swirl velocity will have a different direction on each side of the propeller. With this effect, the upgoing blade will create an upwash on the wing, and the downgoing blade will create a downwash on it, directly affecting the effective angle of attack perceived by the wing. As the effective lift coefficient produced by the wing is affected by the swirl, the whole load distribution of the wing is changed.

Contrary to the swirl-induced velocity, the axial velocity has an axisymmetrical distribution around the propeller axis. This distribution affects the local loading of the wing by generating a higher effective velocity. The extent of this effect is highly related to the vertical position of the propeller to the wing. For a wing producing positive lift, the distribution considering the propeller's slipstream follows that depicted in Figure 2.10. It is important to note how the distribution also changes for the regions that are not directly inside the propeller's slipstream (W-I and W-IV); this is attributed to the change in inflow conditions to the wing [17].

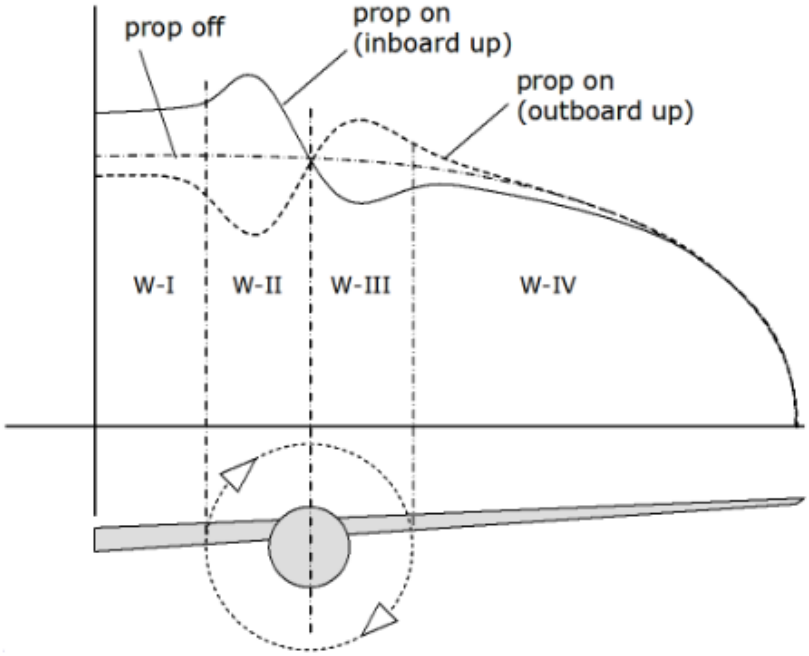

Figure 2.10: Wing lift distribution affected by the induced axial and tangential velocity from the propeller[17].

As a consequence of the induced effective angle of attack by the propeller, there is a reduction in drag in that region of the wing. The reduction happens to both the up-going blade and the down-going blade. In both cases, the resultant vector is shifted to the direction of the flight, which creates a negative drag on the flight direction. This effect can be interpreted as a reduction of swirl losses and an improvement in propeller performance. The wing acts as a stator vane that reduces the swirl velocity and is often mentioned as swirl recovery [23].

2.4. Vortex Breakdown

Vortex breakdown can be defined as “an abrupt change in the structure of the core of a swirling flow” [24]. Before breakdown, the vortex is organised in a nearly cylindrical stable structure with well-defined velocity distributions [25]. This structure rapidly expands into a highly fluctuating structure in which the swirling and longitudinal velocities are reduced in the core. This phenomenon can be observed in Figure 2.11, where the white smoke displays vortex breakdown on an F/A-18 test.

Figure 2.11: F/A-18 smoke and tuft visualisation. NASA Dryden photo EC89-0096-206.

The circumstances for vortex breakdown to occur have been well identified and can be directly linked to the swirl and axial velocity of the vortex. More specifically to the ratio between these two values v_t/v_a and the swirl angle as previously defined in Equation 2.22[25]. The critical value of the ratio cannot exceed around 1.3, corresponding to a swirl angle around 50° [26]. This corresponds to an increase in the swirling velocity compared to the axial velocity. A pressure gradient will have a great impact on vortex breakdown. When an adverse pressure gradient is experienced, the longitudinal velocity could decrease to a point where the ratio surpasses the critical value, and the breakdown occurs. In the same way, a favourable pressure gradient will promote the vortex stability and, in some cases, even create the reformation of the vortex after breakdown [25] [27]. These conditions, however, as stated by Delery [26], do not dictate how and when the breakdown will occur, as it will also depend greatly on the history of the vortex before entering the breakdown. Although, they do give a general idea of the conditions for breakdown. As shown in Figure 2.12, the pressure gradient experienced by the vortex will change the limit ratio of the swirl and axial velocity for breakdown to occur.

To a certain extent, the breakdown relates to the Reynolds number as shown by Delery [26]. As at low Reynolds number the vortex core tends to become more stable and needs a higher swirl number for breakdown. However, the breakdown becomes insensitive to the Reynolds number after $Re > 200$. Although, it does play a key role in the formation of the vortex before it enters the region of adverse pressure. Together with turbulence it will change the shape of the velocity distribution of the vortex.

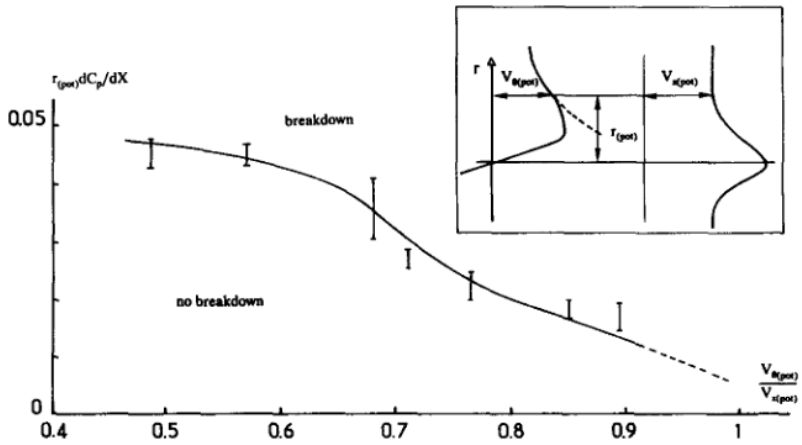

Figure 2.12: Effect of pressure gradient on breakdown limit [26].

It is a matter of debate how many types of vortex breakdowns there are. However, Sarpkaya [28] divides them it into three main ones displayed in Figure 2.13. The top one is a double helix, which occurs at low swirl velocities, in which the central dye filament at the core of the vortex shears into a tape that breaks into turbulence after several revolutions in a helix form. The middle one is the spiral breakdown, found at higher swirl velocities; the dye filament starts to spin around the axis of the core and eventually breaks. This type of breakdown is commonly seen on delta wings. The bottom one is the bubble-type breakdown, found at even higher swirling velocities. In this one, a closed bubble forms axis-symmetrically around the core axis, with the central filament spreading around the stagnation point[29].

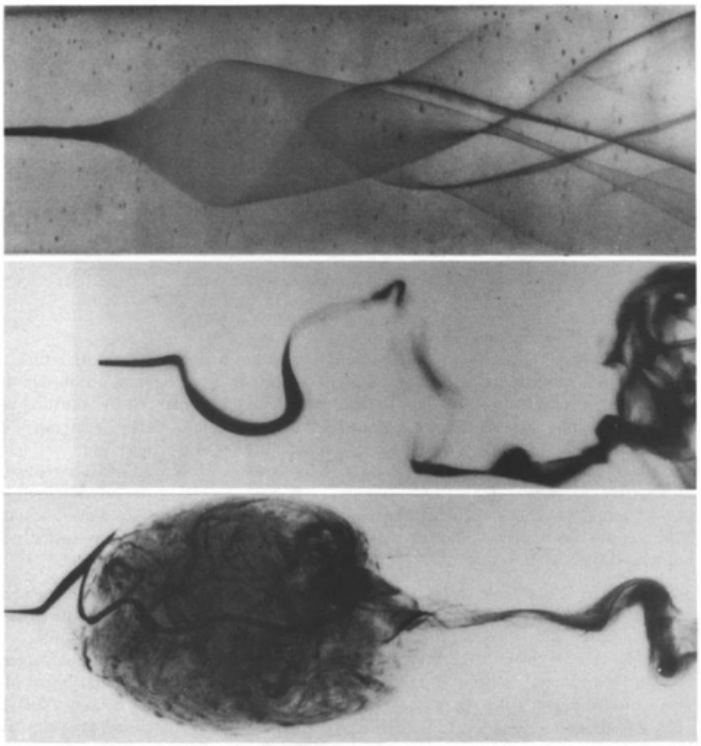

Figure 2.13: Vortex breakdown types. Flow direction from left to right. Double Helix (top, $\theta_{sw} = 38°$)dsa, spiral (middle, $\theta_{sw} = 40°$) and bubble (bottom, $\theta_{sw} = 50°$)[28].

3

Particle Image Velocimetry

This chapter will discuss the flow visualization technique *Particle Image Velocimetry* (PIV). Starting with the working principle in section 3.1, followed by the working principle of Tomographic PIV in section 3.2 and Large Scale PIV in section 3.3. An overview of how Lagrangian Particle Tracking works, including the *Shake the Box* method, will be done in section 3.4. Finally, data interpolation methods used after the *Shake the Box* will be discussed in section 3.5.

3.1. Working principle

PIV is a flow measurement technique that gathers quantitative data on flow velocities based on tracer particle displacements. The particles that have neutral buoyancy and follow the flow with a low time response have the capacity to scatter light. These particles are illuminated homogeneously with a laser shaped to a plane via lens and mirrors. Through a camera, the tracer particles can be pictured in two moments: t and $t + \Delta t$. Having the two images and the time between these two, the flow velocity can be computed. For reference, the typical setup for planar PIV is displayed in Figure 3.1.

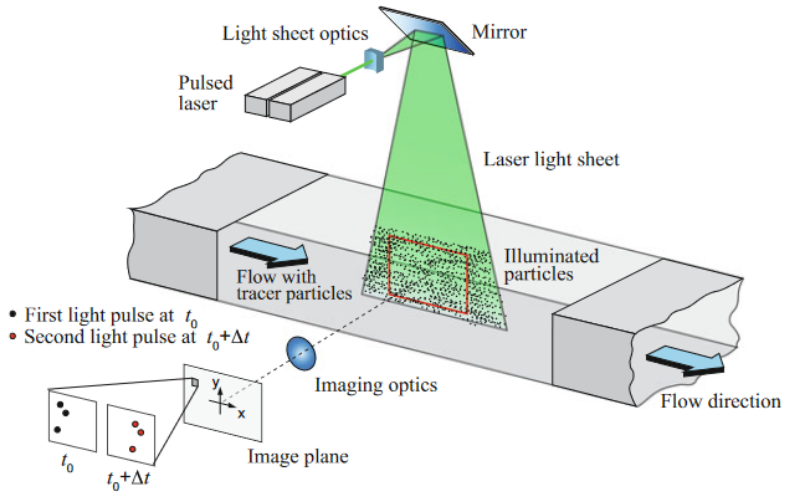

Figure 3.1: Planar PIV standard setup [30].

After acquiring the necessary images, they are divided into smaller domains called interrogation windows. These interrogation windows at time t are cross-correlated with those at $t + \Delta t$, creating a cross-correlation map that will present a peak at the location corresponding to the average displacement of the particles in the window. Since this peak can only be found at an exact pixel location by this method, a Gaussian interpolation is usually performed on the map to get sub-pixel accuracy. After the displacement is calculated, the velocity of the particles can be calculated considering the value Δt and the magnification factor M. This magnification factor is calculated as the ratio between the sensor size and the object size, which is proportional to the distance between the lens and the sensor over the distance between the lens and the object. When only one camera is used, the value of only the two components of velocity parallel to the laser sheet plane can be calculated. In order to obtain the third component, a second camera placed at an angle with respect to the first one must be used. In this sense, the information coming from two different views will enable calculating the velocity in the direction perpendicular to the laser sheet. This technique is called *Stereoscopic PIV*.

PIV has the advantage over other measuring techniques of being non-intrusive in the flow and having a great spatial resolution, capturing the velocity of the entire flow field. However, these advantages come at the cost of a lengthy setup process. In addition to the fact that the flow is not being measured itself, but the particles in the flow are what is being measured.

The basic principles of PIV for a planar 2- or 3-component measurement were discussed above without significant detail. An example of a planar PIV measurement of a NACA 0012 airfoil can be seen in Figure 3.2. However, that is the basic working principle for all the more advanced techniques used currently. More detailed information will be presented in the following sections for these techniques.

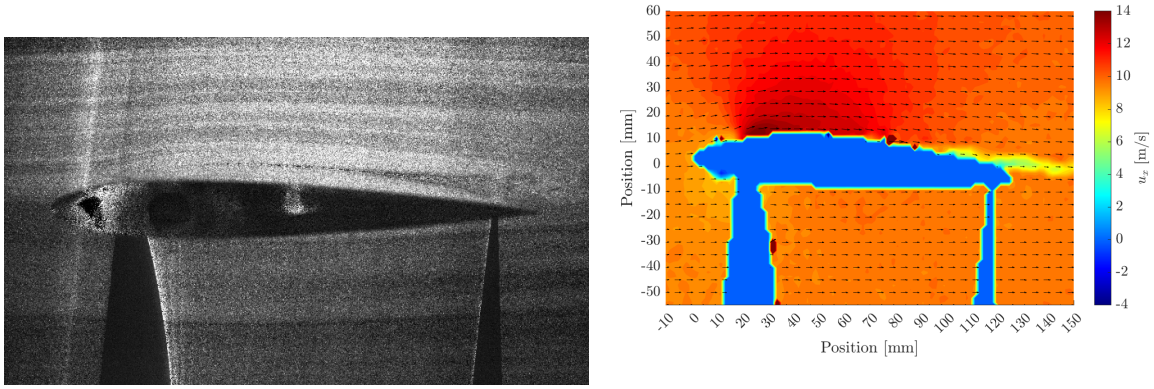

(a) Acquired flow field image.

(b) Instantaneous velocity field after processing.

Figure 3.2: Planar PIV of a NACA 0012 wing at $\alpha = 5°$ and $u_0 = 8m/s$ [31].

3.2. Tomographic PIV

With planar PIV, velocity components can be successfully obtained in three directions when doing stereoscopic PIV. However, this technique only allows one to get the field of a single plane. In order to obtain a 3D or 4D (3D time-resolved) measurement, tomographic PIV (tomo-PIV) introduced by Elsinga et al. [32] has to be employed.

The working principle of tomo-PIV is very similar to planar PIV, adding a few extra elements that allow for the 3D flow visualization. As a starter, the measurement region is no longer a thin laser plane but a volume. Usually, this volume has a thickness of about one-quarter of the length or width of the field of view [33]. In addition to this, several cameras are used to capture the particle from different viewing directions. The fact that the volume now presents a depth also means that the focal depth of the system has to be more extensive to capture particles in all the illuminated volume. A calibration procedure has to be followed before the images are taken in order for the system to correlate the image and object space. Calibration is done using a plate that contains several markers located at different depths. In addition to the physical calibration, a digital self-calibration is performed to reduce calibration errors to below 0.1 pixels. Finally, the images of each camera are analyzed by three-dimensional cross-correlation to obtain the flow field. The standard setup and working principle of tomo-PIV are presented in Figure 3.3.

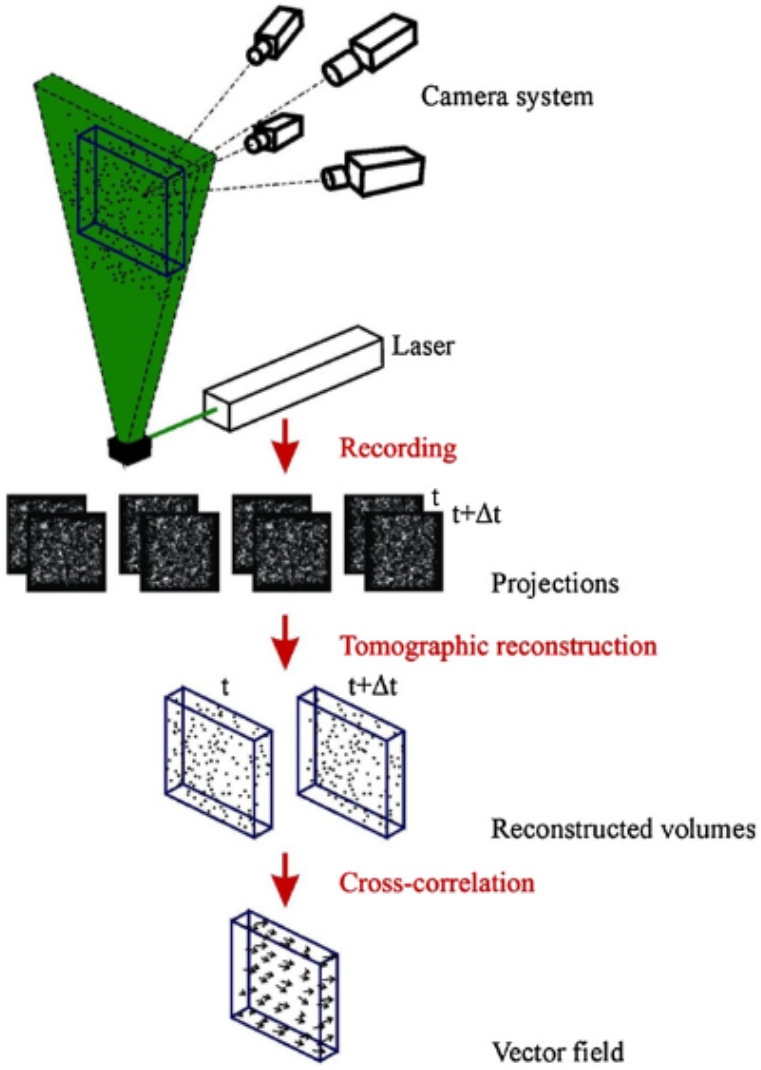

Figure 3.3: Tomographic PIV setup[32].

Volume illumination is most commonly done with laser illumination, just as in planar PIV. Their high pulse energy, short pulse duration, and beam collimation make them a great light

source for tomo-PIV. However, the light intensity necessary to capture the scattering light of the particles increases with the thickness of the measuring volume. This is one of the main limiting factors of tomo-PIV regarding large volumes. The illuminated volume has to be constrained carefully as any light outside the domain will be accounted for in the reconstruction and will increase the noise measurements.

The focal depth in tomo-PIV must be larger or equal to the illuminated area to focus all particles. This focal depth is obtained using diffraction optics as expressed in Equation 3.1 [30].

$$\delta z = 4.88 \cdot \lambda \cdot f_{\#}^2 \left(1 + \frac{1}{M}\right)^2 \tag{3.1}$$

Where λ is the wavelength of light, $f_{\#}$ is the numerical aperture of the lens and M is the magnification factor.

The cameras are placed in a non-colinear arrangement, such as the cross-like and linear configuration depicted in Figure 3.4. In practice, two cameras are considered non-colinear when the angle between them $\theta \gg (d_P/M)/\Delta Z$, where d_τ is the particle diameter, M the magnification factor, and Δz the depth of the measurement domain[33]. From early studies, Elsinga et al. [32] demonstrated that the optimal angle β (depicted in Figure 3.4) lies between 40° and 80°. For smaller angles, the depth resolution decreases, which results in elongated particles. On the other hand angles higher than 80°, the intersection line of sight increases, which causes an increase in the image source density and causes what is referred to as ghost particles. It is important to understand that this is not the only situation where ghost particles are generated, but it is a condition that enhances the appearance of such. Ghost particles will be further discussed later in this section.

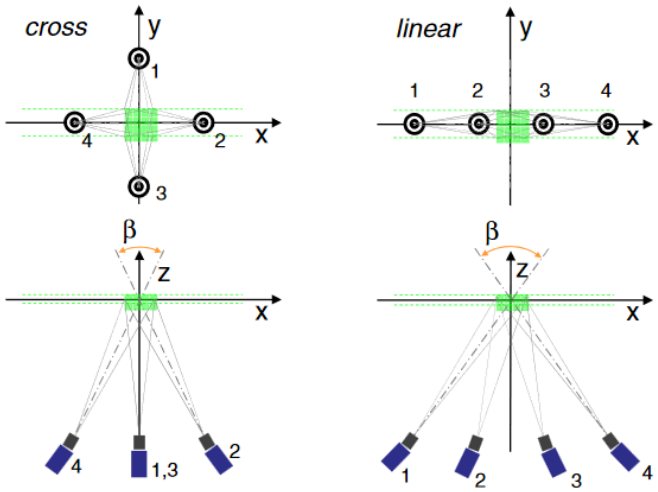

Figure 3.4: Cross-like and linear camera configurations for tomographic PIV based on four cameras [33].

Reconstruction requires the cameras' lines of sight to meet at the particle's exact location. This means that the cameras cannot move more than a fraction of a particle in space before the intensity field cannot be correctly reconstructed [32]. In practice, this is unrealistic as several factors, such as temperature changes, the sturdiness of the mounts, or vibrations due to the cooling systems, among others, can move the cameras during data acquisition. To correct

this, Wieneke [34] introduced a method to correct camera misalignments called volume self-calibration. The method divides the volume into several sub-volumes for which an individual disparity vector will be calculated. Then the possible particle location is calculated through triangulation and compared to the image. The disparity maps can be obtained using this process with many particles (around 10^4) over several images. In these disparity maps, the disparity peak will be the most probable disparity vector used to correct the mapping function. As displayed in Figure 3.5, the disparity maps will display a more significant peak when the number of images used increases. At around ten images, the peak tends to become apparent. This method has proven to reduce the misalignment from several pixels to below 0.1 pixels over the entire domain.

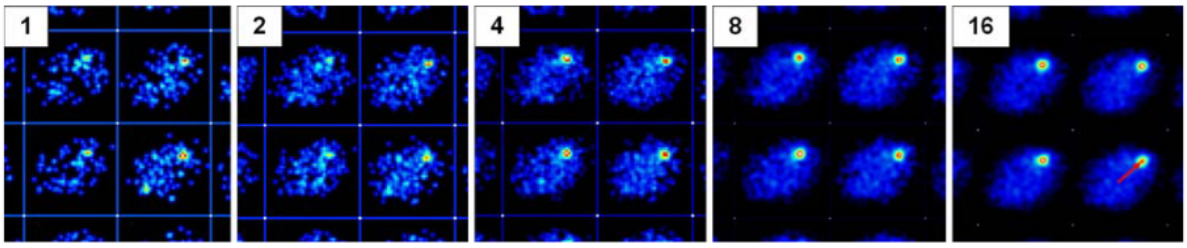

Figure 3.5: Disparity maps comparison for four volumes when augmenting the number of images used[34].

One of the essential factors in tomo-PIV is the reconstruction of the 3D particle distribution, which is based on the mapping function between the images and space. For the reconstruction, the space is mathematically represented by an array of voxels corresponding to the smallest unit solved in a 3D array. This set of voxels discretized the space in a set of coordinates (X, Y, Z) with an intensity $E(X, Y, Z)$[33]. It is important to note that the voxels are represented in the image as spheres; this is how they are treated in most cases as it becomes more practical to calculate the intersection from different lines of sight. Consequently, the line of sight of the pixel is treated as a cylinder. The use of cubic voxels would not be practical for this application.

Furthermore, to clearly understand the formation of ghost particles Figure 3.6 gives a visual representation of the observed particle field with 2 and 3 cameras. It can be noted how the third camera is indispensable in distinguishing a particle from a ghost particle when comparing the left and the center image. Additionally, the right figure displays the effect of too many particles where they cannot be identified clearly from each other.

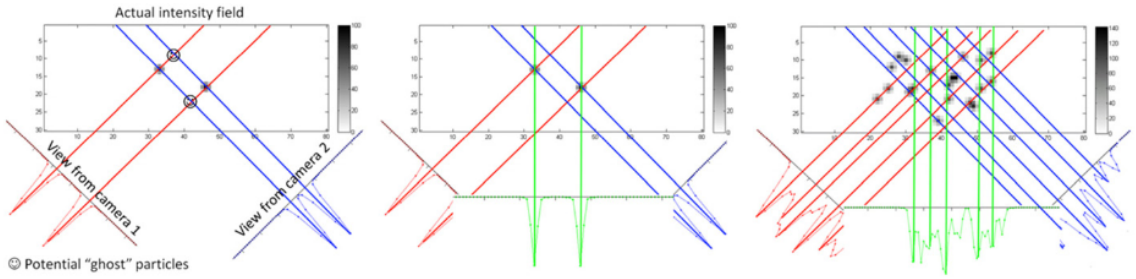

Figure 3.6: Image of 3D particle field. Left: Low particle concentration using two cameras. Centre: Low particle concentration using three cameras. Right: High particle concentration [33].

3.3. Large scale PIV

As previously mentioned, one of the main limitations of tomo-PIV is the light scattering of the particles that require high power and often limits the field of view that the laser can illuminate. Bosbach et al. [35] introduced neutrally buoyant helium-filled soap bubbles (HFSB) to overcome this. By increasing the particle size to increase the scattering capabilities of the same, their time response also increases. This time response is the parameter that indicates how quickly the particles can respond to a change in velocity and is computed as follows [30]:

$$\tau_{\mathrm{P}} = d_{\mathrm{p}}^2 \frac{\rho_{\mathrm{p}} - \rho_{\mathrm{f}}}{18\mu} \tag{3.2}$$

With d_{p} the diameter of the particle, ρ_{p} the density of the particle, ρ_{f} the density of the fluid and μ is the dynamic viscosity . With this definition, it can be seen that increasing the particle diameter will increase the time response. Hence, increasing the diameter proves a challenge for the particle to be able to follow the flow accordingly. This consequence was studied by Scarano et al. [5] by using sub-millimetre HFSB (around 300 microns) and proved to be suitable for use in PIV. The estimated time response of the HFSB lies around $10\mu s$.

The working principle of the bubble generator is displayed in Figure 3.7. The image shows the nozzle that generates the bubbles. The nozzle works by blowing helium through an inner pipe coaxially mounted with an outer one with soap flowing constantly. Air is blown through on the outside of these pipes and pushes the air film through the orifice at the end of the nozzle; this film eventually detaches and generates bubbles. Initially, due to the high costs of producing the nozzles, bubbles were generated in a reservoir and then pushed into the wind tunnel employing a piston actuator as seen in the work performed by Caridi et al. [36]. This technique was replaced with the capability to produce nozzles at a low cost; the current technique generates the bubbles directly at the settling chamber of the wind tunnels through a seeding rake. To avoid the production of double bubbles and ensure the correct size of the bubbles, specific flow rates have to be set; these flow rates are regulated through the inlet pressure [37].

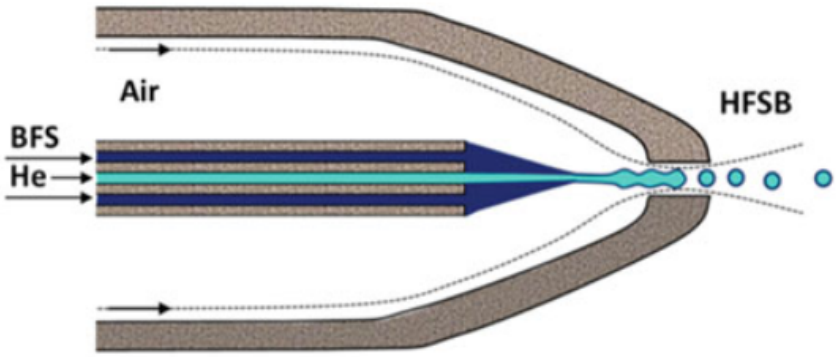

Figure 3.7: HFSB nozzle working principle[30].

The spatial resolution of the measurement can be represented using the dynamic spatial range (DSR) as an indicator. The DSR is the ratio between the largest and the smallest resolvable spatial wavelength. In this case, the ratio between the length of the field of view and the size

of the interrogation volume [36]. The expression can be seen in Equation 3.3, where L is the length of the field of view and Δx is the particle displacement.

$$DSR = \frac{L}{\Delta x} \tag{3.3}$$

Similar to the spatial resolution, the velocity resolution can be measured through the dynamic velocity range (DVR). The latter relates the maximum velocity ($u_{\max}$) to the minimum resolvable velocity defined by the rms of the velocity measurement (σ_u) as seen in Equation 3.4[38]. By eliminating the time component from the equation the right-hand side of the equation is obtained with $\Delta X_{\max}$ the maximum displacement of the particle and $\sigma_{\Delta X}$ the rms of the displacement error. In the same manner as the DSR, a high DVR is desired as it would mean that a smaller displacement in a big range can be resolved.

$$DVR = \frac{u_{\max}}{\sigma_u} = \frac{\Delta X_{\max}}{\sigma_{\Delta X}} \tag{3.4}$$

There are two possible configurations to locate the seeding rake, the first is in the settling chamber of the wind tunnel, and the second is downstream of the contraction (see Figure 3.8). The concentration of particles in the measurement volume can be calculated as [36]:

$$C = \frac{\dot{N}}{L_{\text{inj}}^2 \, (u_0/\rho)} \tag{3.5}$$

Where C is the concentration (number of particles in the measurement volume), L_{inj}^2 is the area of the seeding rake, ρ is the ratio between the cross-sectional area of the seeding rake and the cross-sectional area of the seeded streamtube in the test section and $\dot{N}$ is the particle production rate. This expression shows that to get a higher concentration of particles, it is helpful to place the seeding rake at the settling chamber of the tunnel. However, it comes at the cost of having a smaller seeded stream tube at the measurement location. This equation is handy when an approximate number of particles per pixel (ppp) needs to be calculated (see Figure 3.8).

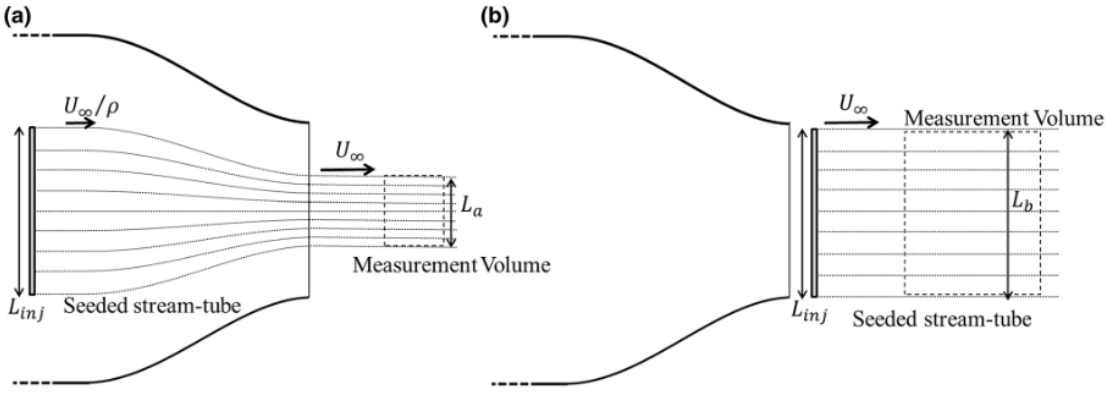

Figure 3.8: Location of particle generator. (a) Generator inside the settling chamber ($\rho > 1$) (b) Generator downstream of the contraction($\rho = 1$)[36].

3.4. Lagrangian Particle Tracking

Lagrangian particle tracking (LPT), sometimes called 3D particle tracking velocimetry, refers to tracking the tracers individually in a Lagrangian reference frame in the three-dimensional domain. More specifically, the Shake-The-Box (STB) method introduced in 2013 by Schanz et al. [6] predicts the position of the tracked particles and refines the position by using image matching schemes. STB permits similar particle concentration as tomo-PIV without the drawbacks of ghost particles affecting the results, high computational times, and the spatial resolution constrained by the average of the interrogation volumes [6]. For reference, Figure 3.9 displays a water jet flow reconstructed with the STB method.

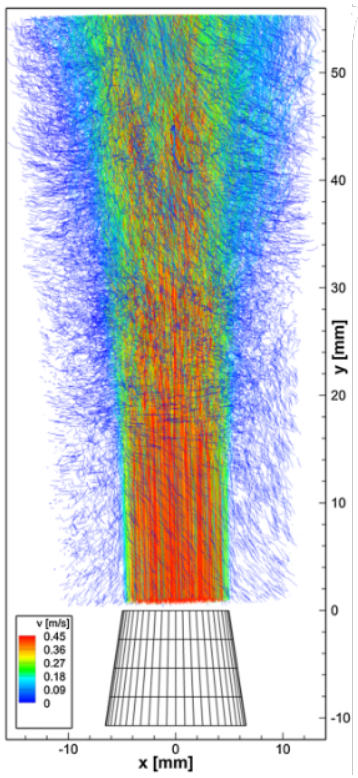

Figure 3.9: Particle tracks of water jet reconstructed with STB method [39].

The STB method, as described by Schanz et al. [39], works in three main phases: The initialization phase, the convergence phase, and the converged phase. Within these three phases, several operations are performed every time-step of the solution. These will be explained within the phases (sections 3.4.1 - 3.4.3).

3.4.1. Initialization phase

No particle information is known inside the experimental domain in the initial stage. Consequently, a system of tracks has to be defined from the images to allow the algorithm to proceed to the convergence stage:

1. Particles are identified by using iterative triangulation from the 2D images.
2. Particles with identified tracks are considered; the rest are deemed potential ghost particles. The number of time steps accounted for the initialisation process is usually set

to 4 but can be manually adjusted. Several methods can be applied to identify the trajectories in these initial time steps, including applying a search radius around already identified tracks, using tomo-PIV as an initialisation method, or CFD results can be used to predict particle tracks, among others.

3. The identified tracks are verified to comply with a specific acceleration and velocity threshold (manually set by the user).

The tracks that are accepted are then added to the system.

3.4.2. Convergence phase

The tracked particles in the previous phase are extended from the current time step to the next using a Wiener filter. For this filter, each particle is treated independently, increasing the prediction's accuracy. After the filter, the particle position will be close to its prediction. However, to find the exact location, the particle is 'shaken' around the predicted position using image-matching techniques. The typical evaluation shake width for every iteration is around 0.1px, except for the initial shake, which has a larger width of 0.4-0.8px to cover for particles with a low temporal resolution that travel a larger distance. The value of the shake width can also be manually adjusted to suit the specific case.

After each shake iteration, the intensity of the particle is calculated. If the intensity falls below a certain threshold, the particle is considered lost and is deleted. Each particle undergoes an initial shake plus five to ten normal shake iterations that prove sufficient for the application.

The tracked particles during the shaking process will be removed from the images creating residual images. New particles are added from these images using the same triangulation method as in the initialization phase but with a lower allowed triangulation error. This process is then done again from the new residual images created. Eventually, it stabilizes for a certain number of particles for the current time step. The candidate particles found in the three previous time steps are used to create tracks of length 4. The difference with the initialization phase is how the particle's position is predicted. In this case, a predictor is constructed from neighbor particles. The particles leaving the domain will be eliminated. This process will continue for the next time step, in which tracking the particles will become easier, and will continue until almost all the particles are tracked. The system is considered converged at that point, and the process advances to the converged phase.

3.4.3. Converged phase

In the converged phase, the number of detected particles is more or less stable. Most tracks are already known such that new tracks come mostly from entering the volume, and tracks are deleted from leaving the volume. Figure 3.10 depicts how STB works in the converged phase. Initially, the residual image is the same as the recorded image, as no particles have been removed, followed by the prediction stage, where most tracked particles are affected in the residual image, and only new particles entering from the bottom and left can be seen. After shaking the particles, the residual images are almost clear except for the newly entered particles. As the particle density is reduced, new particles are detected by triangulation. In some cases, as seen in the last step, overlapping particles can be triangulated by leaving one camera view out of the calculation. In practice, the resulting image is never completely clear as the intensities of the particles are never the same on every camera; this effect is even more significant when the particles are not circular but oval and scatter light differently in every direction.

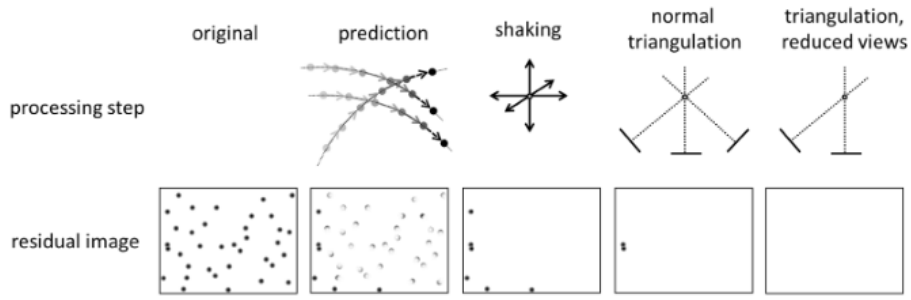

Figure 3.10: Steps of converged STB process [39].

3.5. Data mapping

After obtaining the tracks from the STB method, velocities and acceleration are only available at the exact location of the track. Hence, data needs to be interpolated into a Cartesian grid to obtain a better flow visualisation; this process is called binning. To obtain a higher spatial resolution, it is possible to do a time-averaged interpolation in which all the selected time instants are coupled into a single one. Although very effective, it loses the capacity to visualise unsteady flow fields.

The first step in performing the binning process is to select the grid elements' size, the overlap between each cell and the necessary number of particles inside a bin to be considered. If, for example, a bin of 16 voxels with a 75% overlap is chosen, the result will be a grid with vectors calculated every 4 voxels. The value of these parameters will be very dependent on the case as a bin size too small might not have enough particles for the set threshold, and a too large bin will result in a very low spatial resolution, not allowing to visualise any of the flow characteristics properly. The contribution of a particle to a cell is calculated using a Gaussian weighting function. Afterwards, the cell values are calculated using a polynomial regression with all the particles in the bin. The chosen order of the polynomial will affect the result of the regression. An order zero polynomial will give the Gaussian weighted average with a smooth result but dampened maxima. An order one polynomial will fit the offset and the linear gradients, and an order two polynomial will additionally fit the curvature, preserving the maxima but likely resulting in a noisier fit [40]. In addition, a filter can be applied to use the information from several consequent time-steps. Although this is helpful to achieve a greater number of particles within a bin, it must be selected carefully, as a too-great filter length will dampen the visualised motion.

More complex methods can be employed to achieve finer details when interpolating the data into a grid, such as the Vortex in Cell (VIC) methods. These physics-based methods are able to increase the spatiotemporal resolution of the flow field by taking the tracks' information and running a Navier-Stokes solver[41][42]. The VIC methodology was first introduced by Christiansen in 1973 [43], and the subsequent methods are based on the same principle with certain changes.

The formulation of the VIC methods is set on a grid with spacing h with vorticity ω_h, defined using radial basis functions and a related velocity u_h, through a Poisson equation only valid for incompressible flows [42]:

$$\nabla^2 \boldsymbol{u}_h = -\nabla \times \omega_h, \tag{3.6}$$

With boundary conditions on velocity. The velocity material derivative is defined in the grid as:

$$\frac{\mathrm{D}\boldsymbol{u}_h}{\mathrm{D}t} = \frac{\partial \boldsymbol{u}_h}{\partial t} + (\boldsymbol{u}_h \cdot \nabla)\, \boldsymbol{u}_h \tag{3.7}$$

Where the velocity derivative is calculated from the vorticity derivative by solution of a Poisson equation:

$$\nabla^2 \frac{\partial u_h}{\partial t} = -\nabla \times \frac{\partial \omega_h}{\partial t} \tag{3.8}$$

With boundary condition on velocity derivative. The vorticity derivative in Equation 3.8 is calculated as:

$$\frac{\partial \omega_h}{\partial t} = (\omega_h \cdot \nabla)\, \boldsymbol{u}_h - (\boldsymbol{u}_h \cdot \nabla)\, \omega_h \tag{3.9}$$

The velocity and velocity derivative fields can be calculated from the experimental data. Some boundary conditions could be known beforehand from non-slip or free-stream conditions. The remaining boundary conditions and vorticity values are unknown and must be calculated. For this, the remaining radial basis function weights are set into a vector ξ; these variables will be the optimisation variables that minimise a cost function J constrained by the previously defined motion equations. That is the working principle of the VIC+ algorithm.

From the VIC+ method, Jeon et al. [44] introduced the VIC# method that aims to solve some of the issues from VIC+. The main differences between the two methods are:

- Zero initial condition used for the VIC# method. This aims to avoid a poorly chosen initial condition that could get the process stuck at a weak solution or slow down the convergence of it. Although there are methods to determine the initial conditions, evaluating whether it is smooth enough to avoid a local optimisation minima is a tedious process and thus avoided.
- Additional constraints for the VIC# method. To avoid wrongly set boundary conditions that could represent a physically invalid solution, each grid point is evaluated using the continuity equations, the Navier-Stokes equations and the vector calculus identities.
- Coarse grid approximation on VIC#. This method first computes the solution in a coarse grid and then proceeds to do it in smaller ones, which saves computational time and improves reconstruction stability.

4

Methodology

The methodology used for the experimental campaign will be presented in this chapter. Starting with the experimental set-up in section 4.1. Followed by the method used to calculate thrust and torque produced by the propeller in section 4.2. Finally, the binning parameters used will be discussed in section 4.3, emphasising the phase average in subsection 4.3.1.

4.1. Experimental set-up

4.1.1. Wing-Propeller configuration

As previously stated, the experimental setup is meant to resemble the area between the pusher propeller and the horizontal stabiliser of the Cessna 337 Skymaster. As such, a pusher propeller configuration was chosen with a symmetric wing to resemble the horizontal stabiliser. The chosen propeller is an `APC propeller 7x5`, 2-bladed, constant-pitch propeller with a diameter D = 7 inch/17.7 cm, commonly used for RC aircraft. The propeller was powered by a `Maxon Motor RE310007` 60 W brushed DC motor that produces a maximum rotational speed of 9100 RPM and a maximum nominal torque of 83.5 mNm. The motor is controlled by a DC power source, allowing simple rotational speed adjustment. However, the rotational speed cannot be determined through the power source and had to be controlled with a laser tachometer and a piece of reflective tape placed on the axle to avoid reflections on the cameras. Additionally, the motor is housed in a streamline-like shape that reduces the flow perturbances and resembles the fuselage of the Cessna Skymaster. Furthermore, the leading edge and trailing edge of an extra wing section were cut and adapted to the pylon to reduce vortex shedding from it.

The setup incorporates a load cell that measures the thrust generated when placed in a pulling configuration. The thrust values were measured with the loading cell to compare to the calculated values through PIV (section 5.2). Although the propeller is not set to behave in the same way in tractor or pushing configuration, the values serve as a comparison reference.

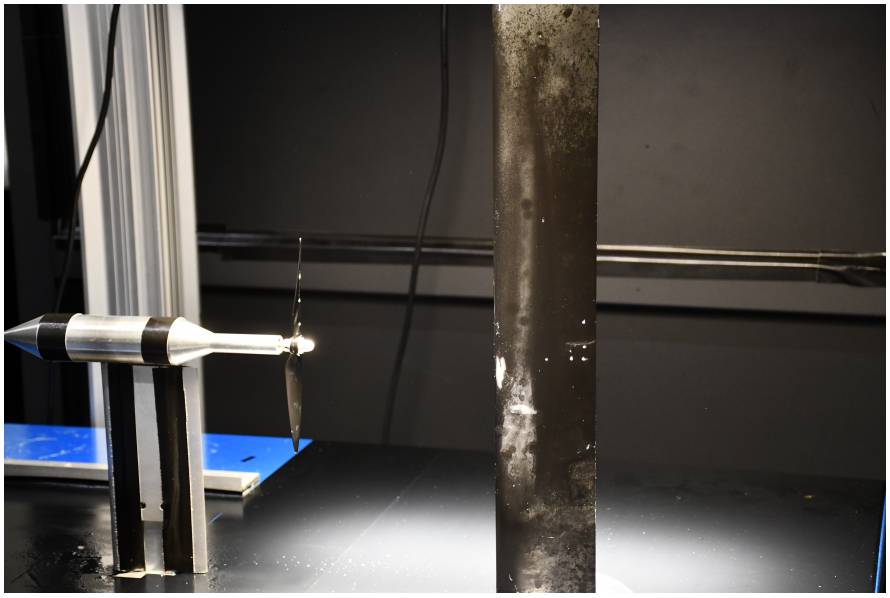

Figure 4.1: Wing-Propeller setup image.

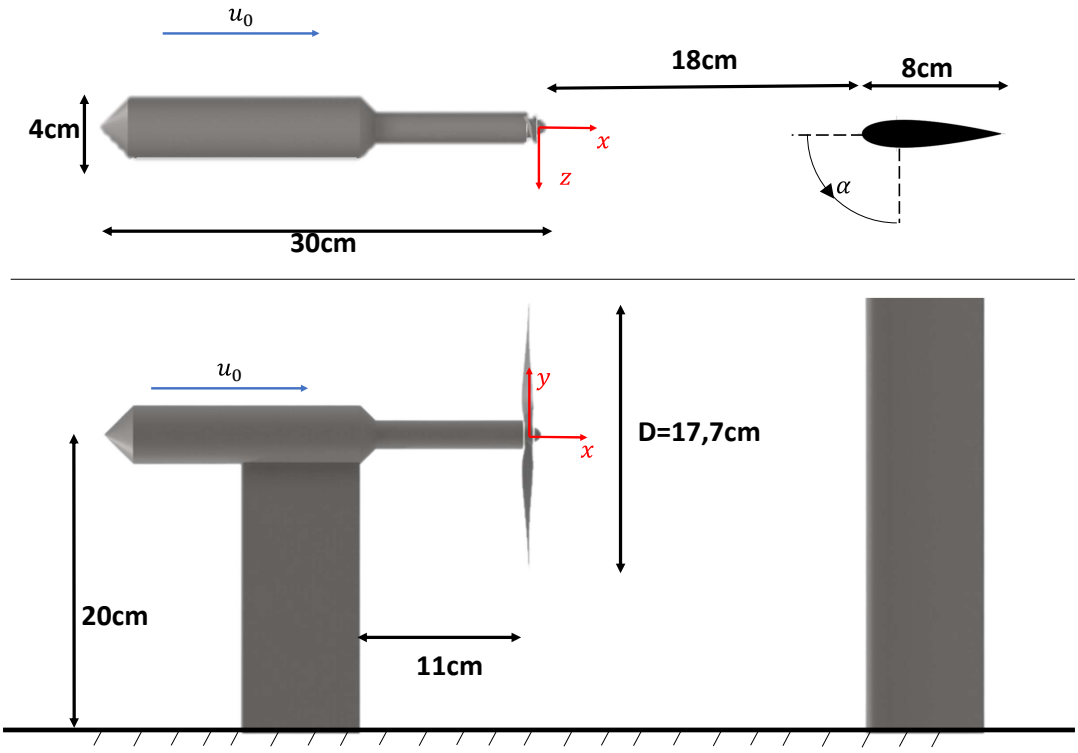

Figure 4.2: Top and side view wing-propeller setup scheme with principal measurements.

Furthermore, the chosen airfoil profile for the wing was a NACA 0020 with a chord length of c = 8 cm and a span sufficiently long to avoid tip effects in the flowfield. The wing was attached to the table with a pivot placed at the quarter chord position and a compass to align the required angle of attack. The placement ensured that the leading edge of the wing was

at a distance of one propeller diameter (1D) from the propeller's plane (i.e. 7 inch/17.7 cm), which resembles that seen on the Cessna [45]. The final configuration leads to a scale-down of 1:10.5 of the aircraft. The propeller and wing were painted in a matte black colour to avoid reflections; however, the pylon could not be painted, but the reflections were deemed acceptable to work with. A picture portraying the wing-propeller configuration and a schematic of the configuration with the respective principal dimensions and reference coordinate axes are shown in figures 4.1 and 4.2 respectively.

4.1.2. Wind tunnel and acquisition equipment

The measurements were performed at the `W-Tunnel` wind tunnel located at the TU Delft High-Speed Laboratory. The `W-Tunnel` is an open-loop, close/open jet wind tunnel with a square exit. The tunnel counts with three square contractions: 40x40cm, 50x50cm and 60x60cm. Only the 40x40cm contraction was used in an open test section configuration for this experimental campaign. In this setting, the maximum achievable velocity is 35m/s, regulated by setting the revolutions per minute of the centrifugal fan at the entrance and measured through pressure taps at the contraction. Depending on the velocity set, the minimum achievable turbulence intensity is 0.5%.

To acquire the images, three `Photron Fastcam sa1.1` cameras were used paired with a `LaVision High-Speed Controller` to synchronise them. These cameras have a sensor of 1024x1024 pixels and a pixel size of 20μm. Furthermore, the maximum acquisition rate is 5400kHz, which can be further increased by cropping the sensor. The cameras were placed in a linear configuration in the horizontal direction, ensuring an angle between them bigger than 40°. Figure 4.3 displays the configuration used for the acquisition system.

Additionally, the cameras were paired with `Nikon` prime lenses. The two outer ones with a 60mm focal length, and the middle one with a 50mm focal length, to ensure that the three cameras had the complete field of view in sight. The resulting measurement volume is 300x300x300mm, with a digital resolution of 3.4 pixels/mm and a magnification factor M = 0.068. Finally, two `LaVision LED Flashlight 300` units were placed on top of the wing-propeller configuration and connected to the same high-speed controller to illuminate the field of view.

4.1.3. Seeding system

To generate the HFSB, a 10-wing, 200-nozzle rake was placed inside the settling chamber of the `W-Tunnel`. The pressure values for air, soap, and helium are controlled by an in-house manufactured Fluid Supply Unit (FSU) that allows the desired pressure for every component to be set independently. Nominally, each nozzle produces between 20,000 to 50,000 bubbles per second, with a diameter between 300 and 500μm [46]. However, this production rate depends on the condition of the nozzle and, in general, of the whole supply system, as nozzles are very prone to block due to dirt in the soap supply. The initial expected concentration calculated according to Equation 3.5 ranges between C = 7.8 particles/cm^3 and C = 19.5 particles/cm^3. Although in the same order of magnitude, this value is somewhat overestimated as the actual measurements achieved concentrations of C $\sim$ 3 particles/cm^3 as will be discussed in section 5.1.

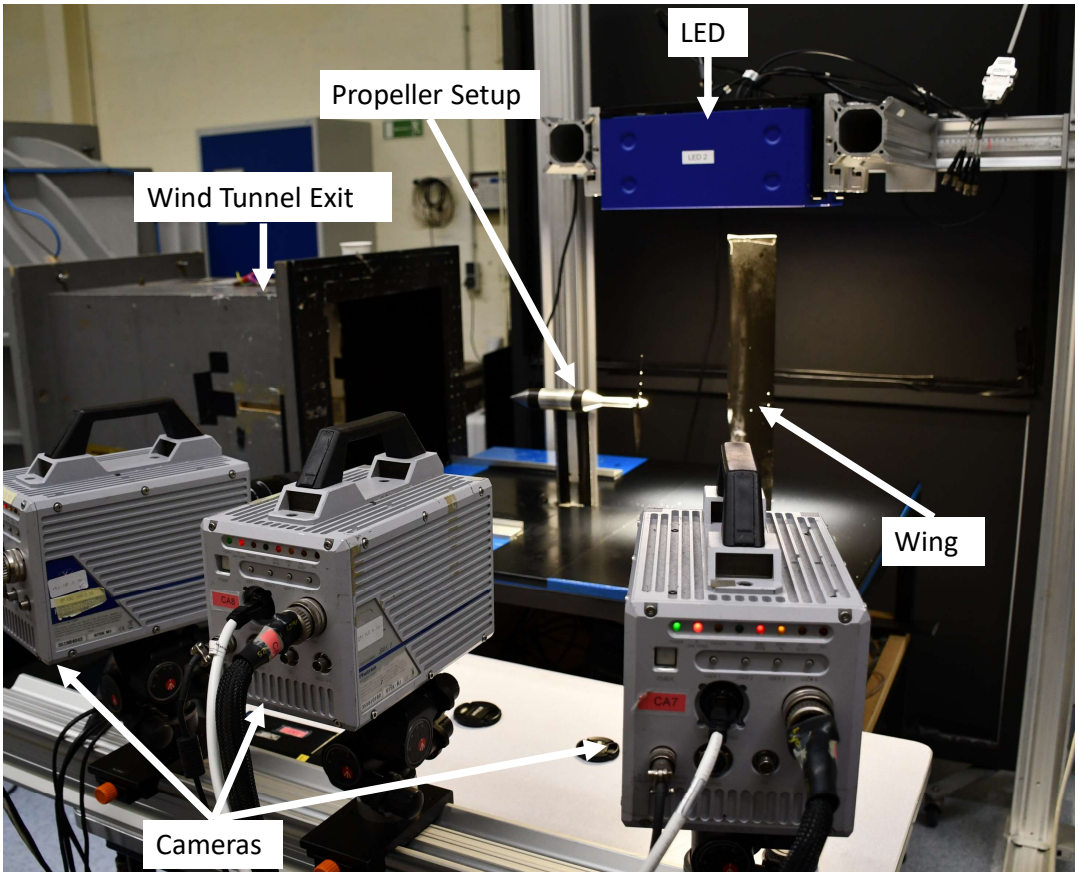

Figure 4.3: Acquisition system configuration.

4.1.4. Studied cases

A total of 5 runs without the wing and 10 runs with the wing installed were carried. The parameters from these runs are summarised in Appendix A. The wing's angle of attack is positive, increasing to the positive z direction as noted in Figure 4.2. All the runs were carried at an acquisition frequency of 5kHz. This value was used based on initial calculations of runs at $u_0 = 10\text{m/s}$, and ensured a small particle displacement close to 1px between images. A total of 5,000 images were acquired for each run. Additionally, a separate calibration procedure was performed for each set of runs. All the images were acquired and processed using the software `DaVis 10`.

4.2. Load evaluation through PIV

Although not directly measured when performing PIV measurements, loads can be calculated through it. In order to evaluate loads first, the pressure has to be derived from the velocity flow field. When the flow is assumed to be incompressible, the pressure gradient can be obtained using the Navier-Stokes equations [47]:

$$\nabla p = -\rho \frac{\mathrm{D}\mathbf{u}}{\mathrm{D}t} + \mu \nabla^2 \mathbf{u} \tag{4.1}$$

Where ∇p is the pressure gradient, ρ is the density assumed to be a known value, $\mathbf{u}$ is the instantaneous velocity, and μ is the dynamic viscosity also assumed to be known. The sub-

stantial derivative $\frac{\mathrm{D}\mathbf{u}}{\mathrm{D}t}$ represents the acceleration from a Lagrangian perspective, i.e., following the particle [48]. It can also be represented as:

$$\frac{\mathrm{D}\mathbf{u}}{\mathrm{D}t} = \frac{\mathrm{d}\mathbf{u}_p(t)}{\mathrm{d}t} = \frac{\mathrm{d}\mathbf{u}\left(\mathbf{x}_p(t), t\right)}{\mathrm{d}t} \tag{4.2}$$

Where $\mathbf{u}_p(t)$ and $\mathbf{x}_p(t)$ are the velocity and the position of the particle at time t, respectively. The substantial derivative can also be computed in Eurelian coordinates as:

$$\frac{\mathrm{D}\mathbf{u}}{\mathrm{D}t} = \frac{\partial \mathbf{u}}{\partial t} + (\mathbf{u} \cdot \nabla)\mathbf{u} \tag{4.3}$$

Composed of the local derivative(first term) plus the convective derivative(second term). The third path to calculate the pressure is to use the Poisson equation by taking the divergence of Equation 4.1 under the assumption that the flow is divergence-free (incompressible) results in[47]:

$$\nabla^2 p = -\rho \nabla \cdot (\mathbf{u} \cdot \nabla)\mathbf{u} \tag{4.4}$$

All three approaches can be taken to compute the pressure from PIV measurements; the difference in each approach is which information is taken from the PIV measurement and will influence the accuracy of the computation. Each method will have a different propagation of the velocity error and sensitivity to the discretisation. These methods of pressure determination through PIV have been proven to provide accurate data in studies such as the one of Ragni et al. [49] and van Oudheusden [47]. In this campaign, the pressure was evaluated through the available option inside the software `DaVis 10`; the software solves the Poisson equation using pressure gradient boundary conditions over the surface (Neumann) and setting at least one Dirichlet condition, using the Bernoulli equation or an average pressure value to offset the pressure field. For the pressure calculations in this research, three points along the freestream flow were selected where the pressure was set to 0 (Dirichlet) .

When the pressure has been determined through the previously described methods, loads can be evaluated from the flow. Flowfield load determination can be done by employing the conservation of momentum in a control volume that contains the body [48]. The control surface and volume can be identified as shown in Figure 4.4.

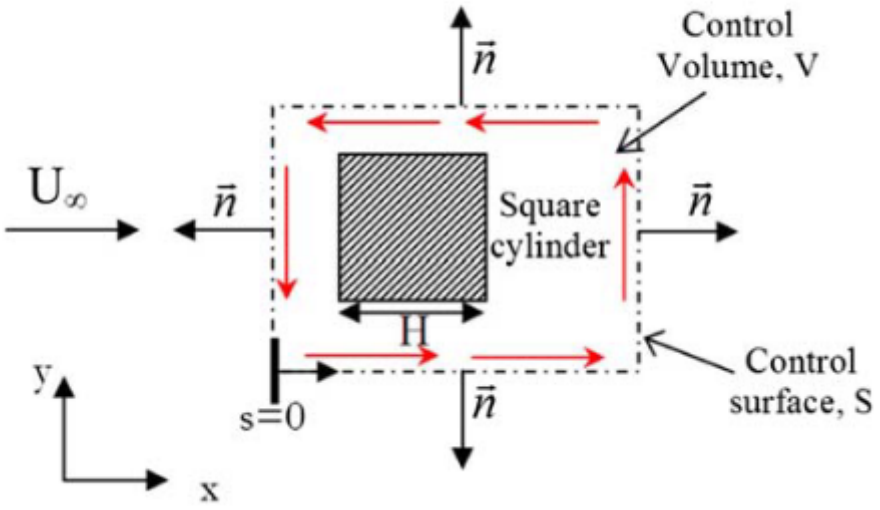

Figure 4.4: Control volume around object for momentum conservation [9].

The balance of momentum is done by employing Newton's second law that states the change in momentum in volume V (right side of Equation 4.5) will equal the net force (left side of Equation 4.5)[9]. The first term of Equation 4.5 represents the momentum change rate due to unsteady momentum variations inside volume V. The second term represents the momentum change due to convection where **n** is the normal direction pointing outside the volume. The third term represents the change in momentum due to pressure on the surface. Finally, the fourth term represents the viscous forces where τ is the viscous stress tensor[10].

$$\mathbf{F}(t) = -\rho \iiint_V \frac{\partial \mathbf{V}}{\partial t}\, \mathrm{d}V - \rho \iint_S (\mathbf{V}\cdot\mathbf{n})\mathbf{V}\, \mathrm{d}S - \iint_S p\mathbf{n}\, \mathrm{d}S + \iint_S \bar{\tau}\mathbf{n}\, \mathrm{d}S \tag{4.5}$$

As demonstrated by Kurtulus et al. [9], the viscous stress contribution at the tested Reynolds numbers is negligible compared to the other terms of the equation when the control surface is taken sufficiently far from the body's surface. In addition to this, the top and bottom boundaries do not need to be considered if they are taken sufficiently far away from the body. This is because the top and bottom boundaries are aligned with the streamlines, which means there is almost no flow through them. Additionally, the flow through the upstream boundary will be uniform with the freestream velocity, and the integral is written in terms of the downstream boundary. In that case, where the wake is the only term evaluated, and the viscous term is neglected, the equation becomes:

$$F_x(t) = -\iiint_V \frac{\partial u}{\partial t}\, \mathrm{d}V + \rho \iint_{\mathrm{S_{wake}}} (u_0 - u)\, u\, \mathrm{dS} + \iint_{\mathrm{S_{wake}}} (p_0 - p)\, \mathrm{d}S \tag{4.6}$$

Where p_0 is not the total pressure but rather the static pressure at the inlet. Often, evaluating the volume integral with the time-dependent term poses a problem due to limitations on the optical access, as the flow needs to be defined for the entire volume in a time instant. In this cases, the time-averaged force acting on the body can be obtained by decomposing the equation into Reynolds averages and averaging both sides. Then, the integrals only need to be evaluated on the wake surface[10]. Finally, since the computed force in this case is thrust, the final equation becomes:

$$T = \rho \iint_{S_{wake}} (u_0 - \bar{u})\,\bar{u}\ \mathrm{dS} - \rho \iint_{S_{wake}} \bar{u'^2}\ \mathrm{dS} + \iint_{S_{wake}} (p_0 - \bar{p})\,\mathrm{dS} \tag{4.7}$$

Where $\bar{u}$ and u' are the time-averaged and fluctuating streamwise velocity terms, respectively.

In the same way that the produced thrust is calculated through a control volume, torque is calculated using angular momentum. It is assumed that all the change to angular momentum in the flow field is due to the propeller movement, and that change will account for the torque exerted on the fluid. The conservation of angular momentum is written down in cylindrical coordinates as follows[50]:

$$\mathbf{r} \times \mathbf{F}_s + \int_{CV} \mathbf{r} \times \mathbf{g}\ \rho\ \mathrm{dV} + \mathbf{Q}_{\mathrm{shaft}} = \frac{\partial}{\partial t} \int_{CV} \mathbf{r} \times \mathbf{V}\ \rho\ \mathrm{dV} + \int_{CS} \mathbf{r} \times \mathbf{V}\ \rho\ \mathbf{V} \cdot \mathbf{dA} \tag{4.8}$$

In this expression, the left side of the equation represents all the torques acting on the control volume, and the right side is the rate of change of angular momentum inside the control volume. The first term is the surface forces due to friction and pressure with $\mathbf{r}$ the position vector and $\mathbf{F}_s$ the surface force. The second term represents the gravity effect integrated over the control volume V, with $\mathbf{g}$ the gravity acceleration. The third term is the torque of the propeller. The fourth term is the change rate of momentum due to unsteady variation inside volume V. Finally, the last term is the angular momentum evaluated at the control surface.

The equation is simplified to calculate only the steady shaft torque. Neglecting the torque that might be generated by surface forces. Additionally, the body forces are neglected due to symmetry. That leaves the equation only with the last term in which $\mathbf{r} \times \mathbf{V}$ will only have a component in the tangential direction since $\mathbf{r}$ only has a component in the radial direction. Similarly to how it was evaluated for the axial momentum, only the control surface of the outflow will affect the torque. That is, considering there is no tangential velocity upstream of the propeller, and the side surfaces are taken several radii away from the propeller. After simplifying the equation, the following expression is encountered [51]:

$$Q = \int_0^R 2\pi r^2 \rho u_\theta u_{ax}\ \mathrm{d}r \tag{4.9}$$

Where R is the radius of the wake at which the flow is being evaluated (note that this value should be large enough to take all of the angular momentum contributions into account), u_θ is the tangential velocity and u_{ax} is the axial velocity component.

4.3. Binning methods

A comparison between a polynomial interpolation, a Vortex in Cell (VIC#) binning method (see section 3.5 for both), and a phase averaging method employed on a modified version from Mitrotta et al. [52], are proposed in this research. The first two methods are implemented through the software `DaVis 10`, and the latter is implemented in `Matlab`. In this section, first, the implementation of the phase averaging method for this case study will be explained in subsection 4.3.1 followed by the chosen processing characteristics for the comparison of the methods in subsection 4.3.2.

4.3.1. Phase average binning

The rotational velocity measurements were performed at the experimental set-up with a laser tachometer. This measurement served as an approximate indication of the velocity but is not robust enough to perform a phase average on this information. Hence, a frequency analysis through the Welch method was used to determine the correct frequency to perform the phase average interpolation. The analysis was done by using the `pwelch` function from `Matlab` that returns the power spectral density and the frequency vectors for the measurements.

To perform the frequency analysis, a binning with large bins (24mm) was performed to ensure the flow field would have no gaps. From this binned data, a plane was extracted where the helical vortex would pass through, as seen on Figure 4.5. With the information from this plane, the analysis was conducted for each individual point for the velocity w, and from these results, the average spectral distribution was computed to obtain the clear peak. Additionally, to avoid a large peak at the zero frequency value, the mean velocity was subtracted before the frequency analysis. An example of the obtained results from the frequency analysis is displayed in Figure 4.6. There is a clear peak at 175 Hz which corresponds to 10,500RPM which is double the actual rotational velocity expected. This is attributed to the two blades of the propeller that each will generate a vortex. As such it is necessary to divide this frequency by half to obtain the actual rotational velocity ω. The calculated values of the propeller frequency used for the phase average are presented in the test matrices in Appendix A.

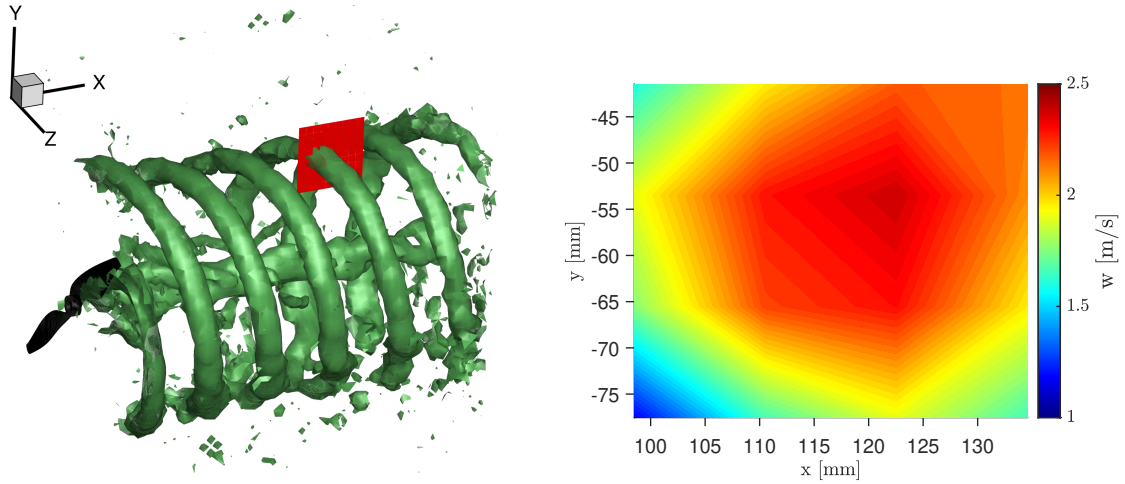

(a) Plane orientation and location.

(b) w velocity plot of cropped plane.

Figure 4.5: Orientation and view of w velocity plane for determining frequency through spectral analysis. In (a) the propeller is seen in black at the left side and the green surface is an iso-surface of vorticity that displays the helical vortex of the slipstream. The displayed red plane is what is seen in (b).

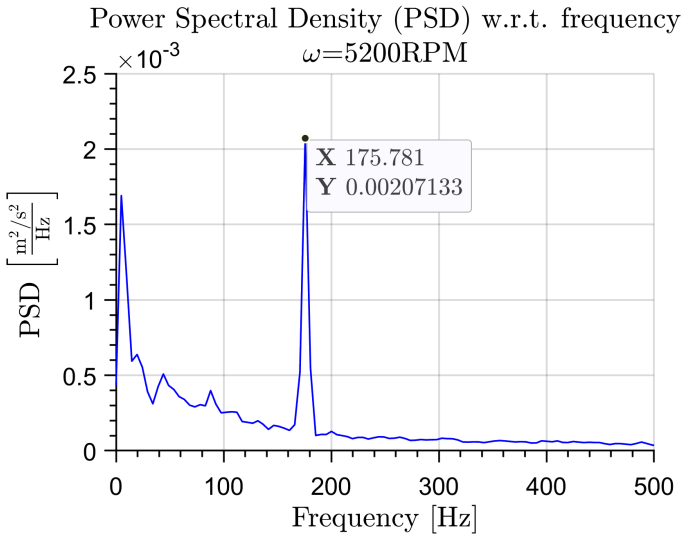

Figure 4.6: Power spectral density w.r.t. frequency, at ω=5200RPM, no wing.

After the frequency had been determined, the phase average binning was performed. The phase averaging binning takes as input the tracks obtained from the STB method and the frequency of the flowfield fluctuations. In this case, the rotational velocity of the propeller ω was used. After selecting the number of desired phases, the algorithm selects all the time instants corresponding to that phase. This time, instants are then treated as a whole to interpolate them into one single frame. The interpolation that the phase-average method performs is very similar to the one explained in section 3.5, with some variations that will now be discussed.

The biggest difference from the polynomial interpolation is the addition of a temporal bin. Similar to the spatial bin, the temporal bin has a length in time, which allows the binning to take into account particles at time steps later and earlier than the desired phase. The addition of this temporal bin adds a temporal component to the weighting function of the particle contribution. This helps to increase the spatial resolution and allows reduction to the size of the spatial bin as demonstrated by Mitrotta et al. [52]. The graphic representation of including a temporal bin can be seen in Figure 4.7.

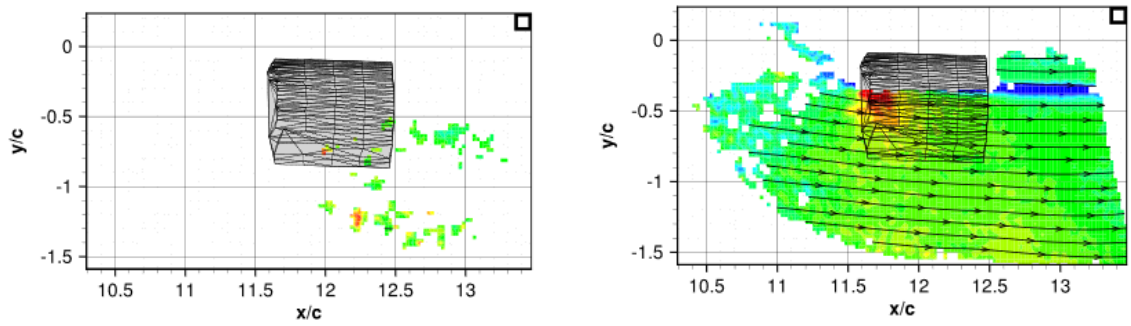

(a) No temporal bin.

(b) With temporal bin of size 1/32 of phase period.

Figure 4.7: Comparison of phase average binning with and without temporal bin. For reference the bin size is displayed at the top right corner of the images.[52].

In addition to the temporal bin, the phase-averaging algorithm also allows selecting the ensemble averaging mode. Incorporating the proposed methods by Agüera et al., [53], the algorithm benefits from a more accurate reconstruction of the flow field. Although the best spatial resolution is obtained with the quadratic polynomial, it comes at the cost of noisier mean flow, especially at regions with low concentration. By implementing an adaptive option, the ensemble method is chosen independently for each bin, considering the number of particles available [54].

4.3.2. Binning parameters

The binning parameters for the polynomial interpolation, VIC# and phase average are similar to obtain a proper comparison. A bin size of $l = 18$mm proved small enough to display the flow field characteristics yet large enough to be computationally efficient and to contain a large enough concentration of particles to fill the flowfield. This was paired with a 75% overlap to ensure a smooth flow field. The threshold to consider a bin was set in all cases at five particles.

For the phase average, a total of 360 phases were chosen, which means there is a time-instant for every propeller rotation angle. With the 5,000 images per run, there are around 10 distinct time instants available at each phase to perform the binning. This value increases to around 50 with the temporal bin selected of 5 degrees, to improve spatial resolution. As discussed in the previous section, the ensemble method was set to adaptative to ensure the best method was used.

5

Results & Discussion

In this chapter, the results of the experimental campaign will be presented and discussed, divided into subcategories aiming to answer the research questions provided in chapter 1. First, the achieved particle concentration will be presented in section 5.1. Followed by the load evaluation done on the propeller through control volume approach will be discussed in section 5.2. Thirdly, three binning methods will be compared in section 5.3. Finally, in section 5.4, the structure of the slipstream vortices and the wing's effects on the vortex dynamics will be reviewed with the selected binning technique from section 5.3.

5.1. Particle concentration

To analyse the achieved concentration after the propeller disc, two x planes are selected where the concentration is evaluated. One is located half a propeller diameter downstream of the propeller (x/D=0.5), and the other at one propeller diameter (x/D=1). The results are presented for two runs at low and high rotational velocity, ω = 4200RPM and ω =6000RPM respectively. The data presented is evaluated with the tracks obtained from the STB process as those account for the true valuable particles in the flow field. Additionally, to obtain a clearer field of view, the concentration is evaluated without the wing installed. The concentration results are displayed in Figure 5.1. At first sight, it is possible to see that the order of magnitude of the concentration is consistent with the anticipated value mentioned in section 4.1 between C = 7.8 particles/cm^3 and C = 19.5 particles/cm^3; nevertheless, a lower value is encountered due to several factors addressed below.

Results show that there is no decrease in particle concentration as a consequence of passing through the propeller disc. Looking at Figure 5.1 it can be noted that the propeller disc does not act as a boundary in any of the depicted cases. The concentration is higher inside and close to the propeller's streamtube. Meanwhile, the blank spots representing the bins where the particle number did not meet the set threshold are away from the propeller disc. This is considered to be a consequence of the propeller's streamtube, as it likely influenced the streamlines even outside of the streamtube in such a way that at the observed region, the particles are more concentrated close to the propeller disc.

The fact that the concentration values are higher at high RPMs is not in any way attributed to the higher propeller rotational velocity. However, it is a consequence of the non-constant production rate of the seeding system for the different runs. Furthermore, the higher concentration located at the upper right side of the figures is attributed to two leading causes. The first

is the same cause as before and is attributed to the seeding rake. It is likely that the nozzles responsible for feeding this area are in better condition and work more continuously than in other regions, and as such, there is a higher concentration achieved in this region. The second cause is the accessibility of the cameras, as they were placed at a positive z value. This means that the line of sight of the camera to the particles at the positive z location is less obstructed. In contrast, the particles in the background are likely obstructed by other particles. The effect of the cameras translates to what is observed in the concentration results, with more tracks being captured closer to the camera. It can then be concluded that if the propeller harms any particles, it is only a negligible amount, and it is independent of the propeller rotational velocity for the tested values. However, the concentration value is strongly influenced by the position and status of the seeding system.

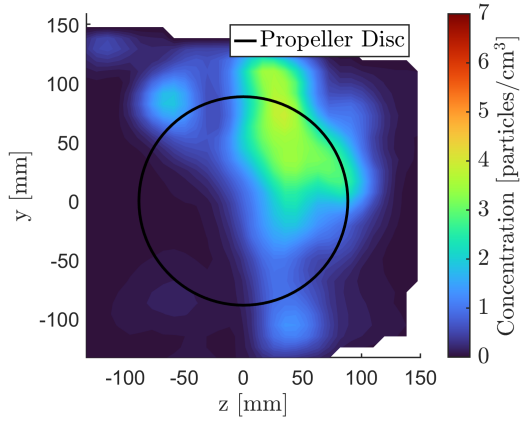

(a) Particle concentration at x/D=0.5 & ω = 4200RPM.

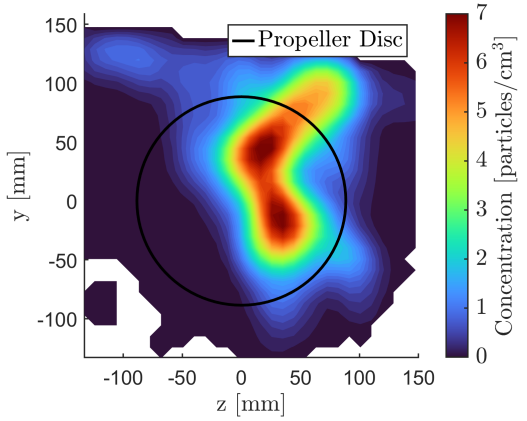

(b) Particle concentration at x/D = 0.5 & ω = 6000RPM.

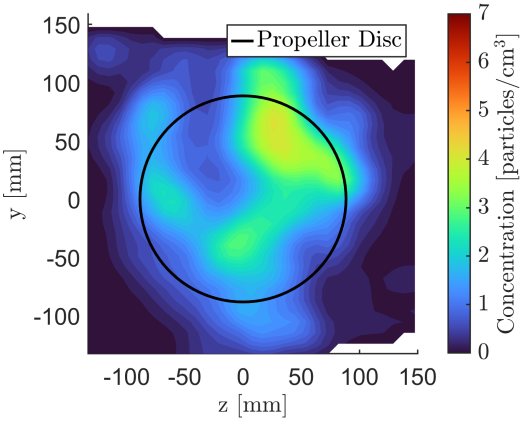

(c) Particle concentration at x/D = 1 & ω = 4200RPM.

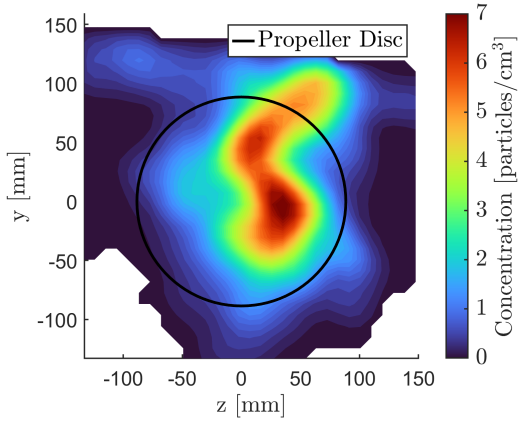

(d) Particle concentration at x/D=1 & ω = 6000RPM.

Figure 5.1: Time averaged particle concentration from 500 time instants at various x locations and rotational velocity values. The black circle represents the propeller disc located at x/D=0. The white blanks are bins where the particle threshold of 5 particles was not met.

Furthermore, when comparing the concentration results close to the propeller and further downstream (Figure 5.1 (a) and (c) & (b) and (d)), it can be noted that the concentration

values stay around the same values, which means that the bubbles do survive for the entire length of the field of view. Although the particles do spread more evenly throughout the slipstream as a result of the flow's rotation, balancing the accumulation of particles on a specific zone caused by the seeding system to a certain extent. This effect is likely more noticeable compared to the plane just downstream of the propeller and far downstream; however, since the method compares obtained tracks from the STB method, it is not able to resolve tracks across the propeller accurately as the propeller acts as a kind of boundary from which tracks have to be computed again.

5.2. Thrust and torque evaluation

The thrust and torque were evaluated through conservation of momentum, as addressed in the previous chapter. The displayed data was evaluated without the wing and with the time-averaged data from the 5000 images of each run. First, the thrust will be discussed in subsection 5.2.1, followed by the torque in subsection 5.2.2.

5.2.1. Thrust evaluation

Figure 5.2a shows the evaluated thrust taking the outflow surface at different x locations calculated according to Equation 4.7. Note that the dotted line represents the full equation, and the solid line neglects the fluctuating term from the Reynolds decomposition (Second Term). The evaluated value from the PIV measurements will be referred to as calculated from now on. The reported thrust value by the manufacturer for the respective conditions is displayed for reference and is addressed as *Reported* with the * marker on the legend. This value will be addressed as reported from now on. Moreover, the value labelled as *Tested* with the $\triangle$ marker corresponds to the measured value with the loading cell. This value will be addressed as tested from now on.

Before going deeper into the discussion, there are two important remarks to make about the reference values. First, the reported value from the manufacturer is based on a computational simulation employing vortex methods for the isolated propeller. For this reason, it is not a definitive value of the propeller's performance but only a reference. It is likely to vary depending on many factors, such as the nacelle used and the inflow conditions, among others. Second, the tested value corresponds to the propeller behaviour in tractor configuration, which is likely to vary from the performance in pulling configuration, which was tested in these measurements. Nevertheless, results show the expected behaviour of the propeller obtaining a lower thrust value for the tested cases than the reported ones.

From Figure 5.2a, it can be noted that the values are first calculated from $x/D = 0.12$; it is not possible to go further upstream as the reconstruction from the tracks is very scarce in that area. As mentioned in the previous section, the reconstruction of the flowfield becomes better further downstream because of the particle distribution and reconstruction of the tracks. Furthermore, it can be seen that the fluctuating term increases the difference between the calculated value and the tested and reported ones. This value also stays somewhat constant along the axial direction. The cause of this behaviour is believed to be the STB method itself, and it is not entirely attributed to the unsteadiness of the propeller slipstream, as the standard deviation measured at the freestream is already too great. As such, it is decided to do further calculations and discussions without considering the fluctuating term (solid line).

The thrust calculation becomes more stable further away from the propeller plane and comes closer to the reference values. Looking at Figure 5.2a, it can be seen that the calculated thrust value shows a plateau after $x/D = 1$. This is attributed to the ability to reconstruct the flowfield away from the propeller's disc fully. Hence, the thrust values used to calculate the thrust coefficient displayed in Figure 5.2b are averaged from the values obtained between $x/D = 1$ and $x/D = 1.25$. Additionally, it can be noted that for both low and high RPMs, the calculated thrust value is in the order of magnitude of the reference values and is close to them, especially when considering that the reference values only stand as a general guide for the previously mentioned reasons. Moreover, it must be considered that the drag from the pylon is being considered in the calculations. The drag has the effect of measuring a lower momentum on the wake and underestimating the thrust. At higher RPMs, the thrust calculation is not as smooth, attributed to the stronger fluctuations encountered, especially closer to the propeller. Nevertheless, the calculated value is much closer to the tested one when calculating far downstream at higher values of ω than at lower ones.

Although the calculations were also performed for different freestream velocities, they are not displayed in Figure 5.2a as they display the same behaviour as the rest and would also result in an overlap. However, they are used for the thrust coefficient evaluation, shown in Figure 5.2b that will now be addressed.

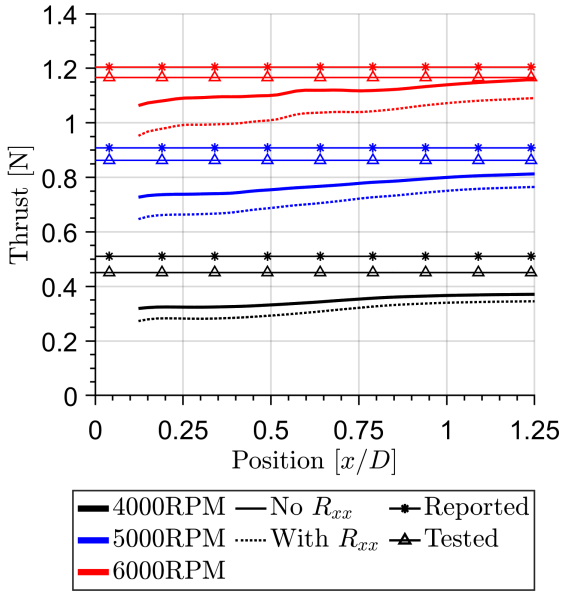

(a) Propeller thrust evaluated at different x positions at u_0=5m/s. Computed values are represented with the solid and dotted lines. * the reported value by the manufacturer and △ the tested value with the loading cell.

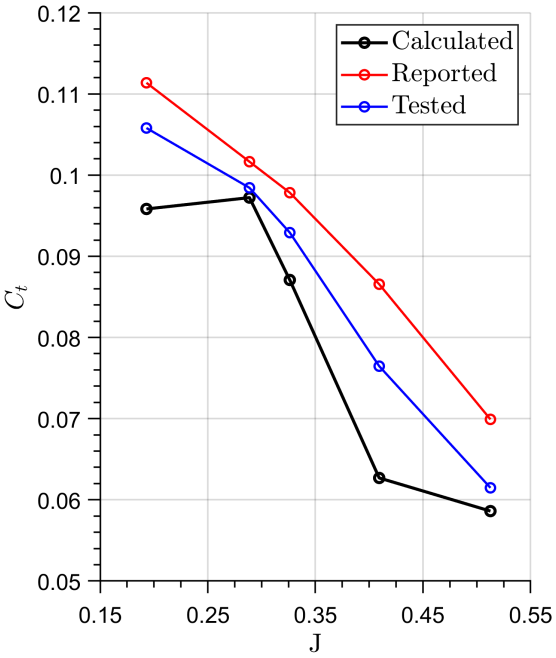

(b) Thrust coefficient w.r.t. the advance ratio for the calculated, tested and reported values.

Figure 5.2: Evaluated thrust values comparison employing net thrust of the propeller and the thrust coefficient.

As mentioned, the thrust coefficient values were computed from the calculated thrust values

far downstream. The results from this calculation for five different advance ratios are displayed in Figure 5.2b. The calculated values show the same tendency as the reference values, equal to the displayed for the computed thrust. However, the tendency resembles the tested one better than the reported one. It can be noted that the second marker from the calculated value is the one that better approximates the tested value. This point represents the run at $\omega = 6000$RPM and $u_0 = 5$m/s that also approaches closer to the tested value in Figure 5.2a. Likely, this can be linked to the previous section (section 5.1), where it was seen that this run, in particular, had a larger particle concentration, which would result in a more accurate reconstruction. Additionally, it is possible that at higher rotational velocity, the particles spread more evenly across the slipstream's streamtube, allowing a more accurate reconstruction of the flowfield. This, however, is only a hypothesis that would need to be further studied by measuring the thrust value with the propeller set in pusher configuration.

It can be concluded that the thrust calculated from the flowfield acquired through PIV measurements and reconstructed through the STB method is accurate within 10% uncertainty to give a correct idea of the propeller's performance. The method benefits from not being invasive and has the advantage of not requiring modifications of the propeller setup.

5.2.2. Torque evaluation

Similar to the previous evaluation done on thrust, torque is calculated at different outflow surfaces and different distances, using Equation 4.9. The results of this calculation are displayed in Figure 5.3a. An important remark is that in this plot, there is no reference value for the tested torque. The reason for this is the lack of measuring equipment for the shaft torque. As such, the only reference value used in this case is the one reported by the manufacturer.

Calculated torque results show a similar behaviour to those of the thrust. The torque reaches a stable value far downstream when $x/D > 1$. Only in this case do the calculated values match the reported values much closer, as seen on Figure 5.3a. Additionally, it can be seen that although far downstream the calculated value is more accurate than the thrust, when closer to the propeller the value fluctuates more aggressively, especially at high RPMs. This is once more a consequence of the inability to reconstruct the flow field in those areas fully, only now the torque calculation is much more sensitive to this effect as it only depends on the rotational value. Thus, at high RPMs, the flowfield close to the propeller will only be partly reconstructed and will fluctuate more.

The torque coefficient is calculated in the same way as the thrust coefficient, averaging the values obtained at $x/D > 1$. The calculated values are displayed in Figure 5.3b. The calculated values follow the same tendency as the reported ones, except for the value at a high advance ratio that shows a larger difference than expected. This value corresponds to the run performed at $u_0 = 8$m/s. The reason for these results is likely the averaging of the flowfield in which the fluctuating term was not accounted for in the torque calculation, after being disregarded in the thrust calculation. It is possible that this term plays a bigger role at higher freestream velocities. Nevertheless, this would have to be tested at higher velocities to ensure this is the case and it is deemed as a methodology error in this measurement. Furthermore, the graph displays that the most accurate data point is the second value of J. This resembles the behaviour of the thrust evaluation, and the reason is most likely the same regarding the concentration.

Finally, it can be concluded that the calculation from the torque values through the evalu-

ation of the flowfield represents an accurate value within 5% uncertainty when the flowfield is completely reconstructed. In this case, evaluating further downstream improves this reconstruction. Since evaluating torque directly at the shaft is usually a complex procedure, this method presents a viable alternative in a non-intrusive way. Nevertheless, increasing the advance ratio from the tested values should be treated with care as the method was not fully tested at high advance ratios.

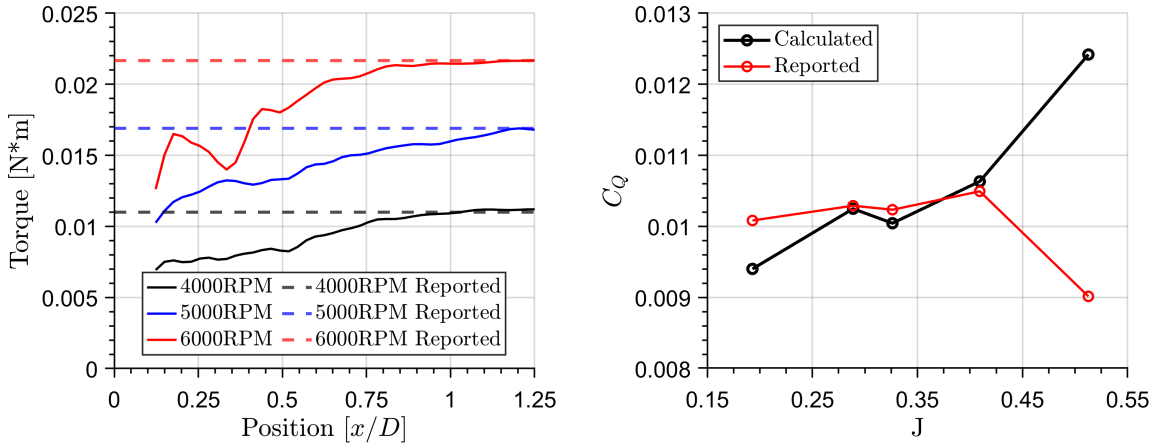

(a) Propeller torque evaluated at different x positions at u_0=5m/s. The computed value is represented with solid lines, and the reported value is represented with a dashed line.

(b) Torque coefficient w.r.t. the advance ratio for the calculated and reported values.

Figure 5.3: Evaluated torque values comparison through torque and the torque coefficient.

5.3. Processing method comparison

The results of the three processing methods are presented in this section. First, a qualitative comparison is made that later leads to a quantitative comparison of the methods to choose the best one for further visualisation. All comparisons are performed with the same STB data acquired at $u_0 = 5$m/s and $\omega = 5200$RPM; as such, these two quantities are not mentioned in the following presented data.

The initial visualisation of the three methods is presented in Figure 5.4, where the iso-surface of the vorticity magnitude $|\omega_v| = 350$ 1/s is plotted to display the vortex system of the propeller's slipstream. Ideally, a vortex system like the one presented in Figure 2.3 should be seen in the flow. It is, however, an experimental method and as such, noise or inconsistencies are expected. Nevertheless, it can be seen that Figures 5.4a, 5.4b and 5.4c display the helical vortex geometry. An important remark is that the binning case contains more noise in the flowfield, the reason why it is decided to present it with a cylindrical mask around the slipstream (5.4a) to visualise the actual slipstream better. After applying the mask, the helical vortex can be recognised among the noise. The technique manages to reconstruct the flowfield as expected, which is why a more thorough analysis has to be made before discarding it. On the other hand, both the VIC# and the phase average reconstructions (Figures 5.4b and 5.4c respectively) display a smooth and cleaner reconstruction of the vortex system. Both had some noise around, with VIC# displaying higher noise concentration, but in a less intruding way

than the binning. This initial analysis gives a good idea of the expected results with every technique, yet it is not enough to draw any conclusions about any of the methods.

Following the initial analysis, a second qualitative analysis is made for the different methods. Figure 5.5 displays a vorticity contour for each reconstruction method. The contours are reconstructed from a slice at z = 0mm, and the white area displays the regions where each method could not reconstruct the flow. For reference, the bin size is displayed at the upper right corner of each contour. The ideal visualisation from this slice would be the well-defined helical vortices on the top and bottom and the root vortex in the middle.

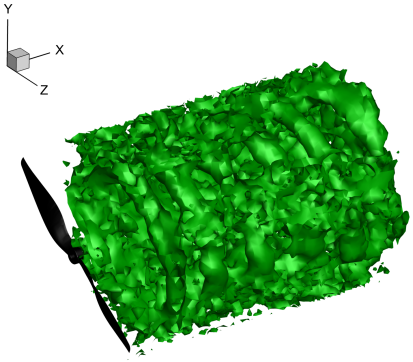

(a) Voriticy iso-surface for binning with a circular mask around the slipstream vortex.

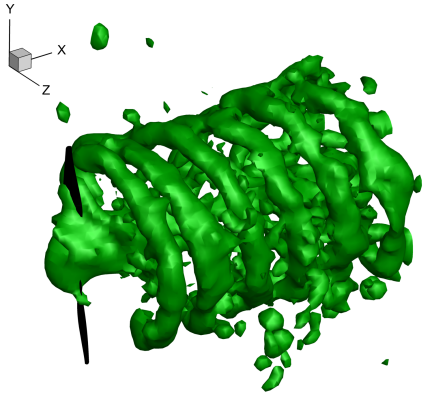

(b) Vorticiy iso-surface for VIC# method.

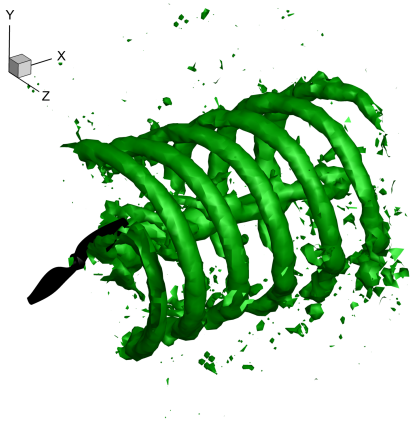

(c) Vorticiy iso-surface for phase average method.

Figure 5.4: Vorticity iso-surface at ω_v = 350 1/s, for polynomial interpolation (top) and VIC# and phase average (bottom).

At first sight, the binning method contour stands out from the other two when looking at Figure 5.5. Not only are the helical vortices not as defined as with the other two methods, but it is able to reconstruct a smaller portion of the flowfield, and the noise seen at the iso-surfaces is also translated to the 2D visualisation. Hence, it is deemed the least robust reconstruction

method of the three tested ones. Although it is able to reconstruct the flow in a way that the main flow characteristics are visible in a less resource-demanding way than the other two methods, the noise found in the result combined with the low spatial resolution makes it the weakest method among the three.

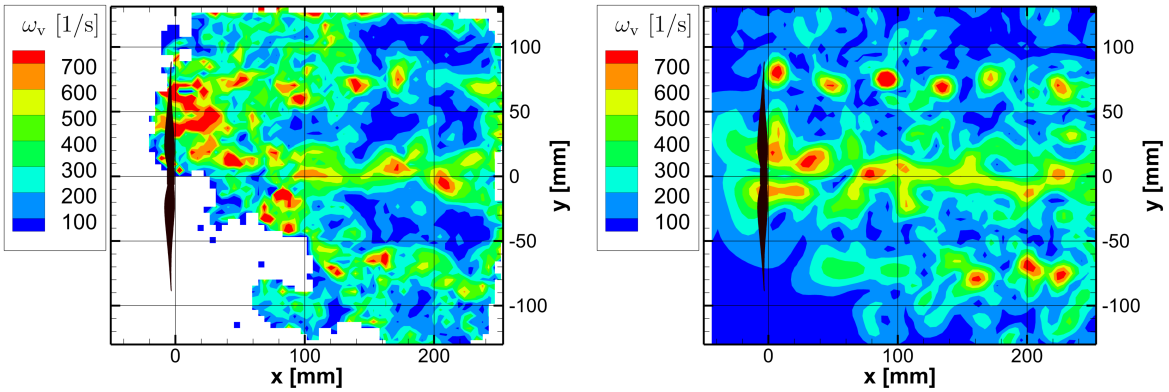

(a) Vorticity contour for binning method.

(b) Vorticity contour for VIC# method.

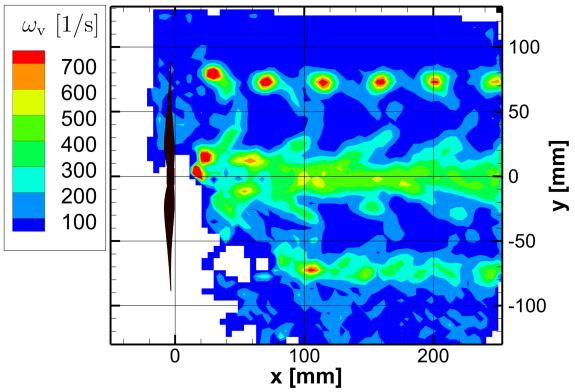

(c) Vorticity contour for phase average method.

Figure 5.5: Vorticity contours at z=0 planes for binning, VIC# and phase average reconstructions methods. Bin size is presented in the upper right corner for reference. White zones are where reconstruction was not possible.

On the other hand, VIC# and phase average vorticity contours display similar results for the flow field reconstruction (Figures 5.5b and 5.5c respectively). Both methods display the helical vortices on top and some at the bottom, as well as a nicely defined root vortex. It is important to remark that the lower definition of the helical vortices passing through the bottom is a consequence of both lower particle concentration and the effects of the pylon. In contrast to the binning and phase average contour, the VIC# results show an entirely filled flow field. This is a consequence of how the method operates by solving the Poisson equation as discussed in section 3.5, which ultimately fills up the entire volume with the computed solution. In conclusion, both methods display a smooth and clear reconstruction of the flow field. Even though the spatial resolution is greater using the VIC# method than the phase average, the computational time and extra noise prevent it from being the best candidate. As such, a more thorough analysis of these two methods is proposed by analysing how some parameters are reconstructed and the methods' precision through statistical analysis.

Initially, velocity and vorticity magnitudes are analysed over time as encountered from a slice plane at the helical vortex location (for reference, see Figure 4.5). These results are depicted in Figure 5.6. It is an initial remark that the VIC# method for both cases displays a noisier trend, with less precision all around. This is especially true for the case where the velocity is compared; in that case, the plot barely shows the expected sinusoidal behaviour. In the case of the vorticity magnitude, the VIC# shows a somewhat similar tendency, but from the phase average results, it is clear that it contains noise. To quantitatively assess the precision of both methods, a statistical analysis with uncertainty is proposed.

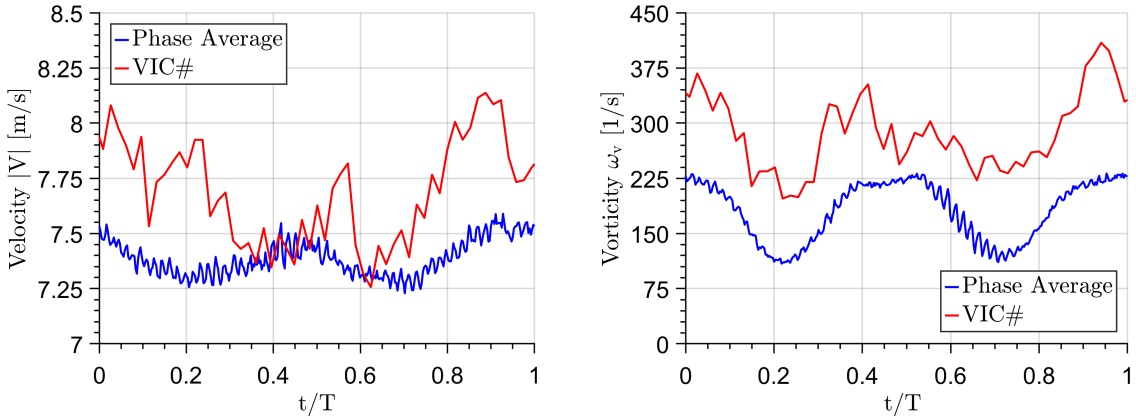

(a) Velocity magnitude at helical vortex location over one period T.

(b) Vorticity magnitude at helical vortex location over one period T.

Figure 5.6: Averaged velocity and vorticity magnitude at helical vortex location as displayed in Figure 4.5 over one period T.

The precision is evaluated through a statistical analysis. The mean and the standard deviation are computed at a z-plane slice at x=0. The values are computed from the 360 phases in the case of the phase average and 150 time instants for VIC#. With the standard deviation, the uncertainty is calculated for a 95% confidence interval assuming the distribution is normal. The results are displayed in Figures 5.7 and 5.8.

From the previous analysis, there was a higher expected uncertainty for the VIC# than for the phase average. Contours displayed in Figure 5.7 show that this is true for almost the entire flow field, and the phase average method has lower uncertainty overall. In the region where the phase average could not reconstruct at low z values, VIC# still performs the reconstruction with a high level of uncertainty caused by the low number of particles.

Looking at the slice taken in the middle of the contours displayed in Figure 5.8, a more detailed analysis can be obtained. Although from the mean velocity, it can be seen that both methods accurately reconstruct the flow field, the uncertainty for VIC# method is triple that of the phase average (0.9 m/s and 0.03 m/s respectively), with a more significant difference at the regions where the helical vortex is located.

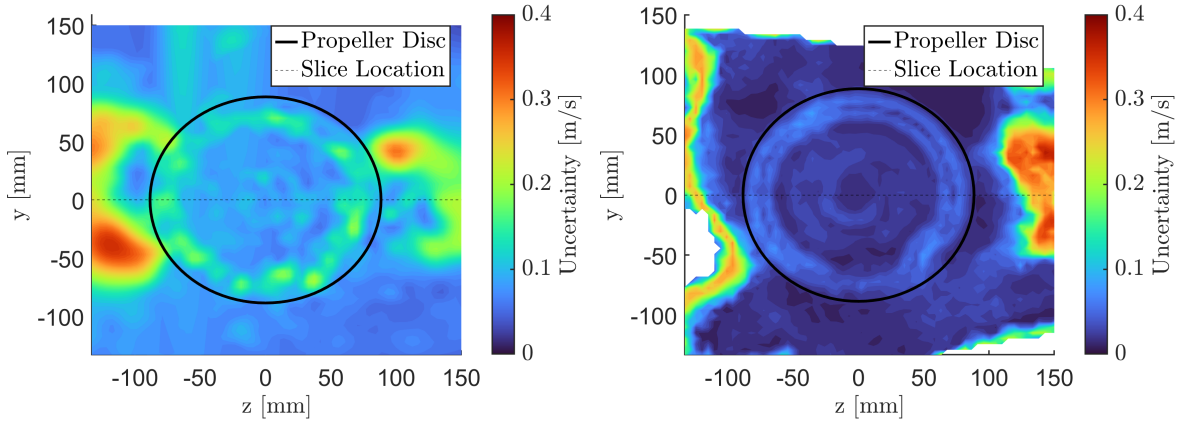

(a) Velocity u uncertainty at 95% confidence VIC# method.

(b) Velocity u uncertainty at 95% confidence phase average method.

Figure 5.7: Velocity u uncertainty at 95% confidence contours at x=0 for VIC# and phase average methods. Dashed line marks the location of Figure 5.8.

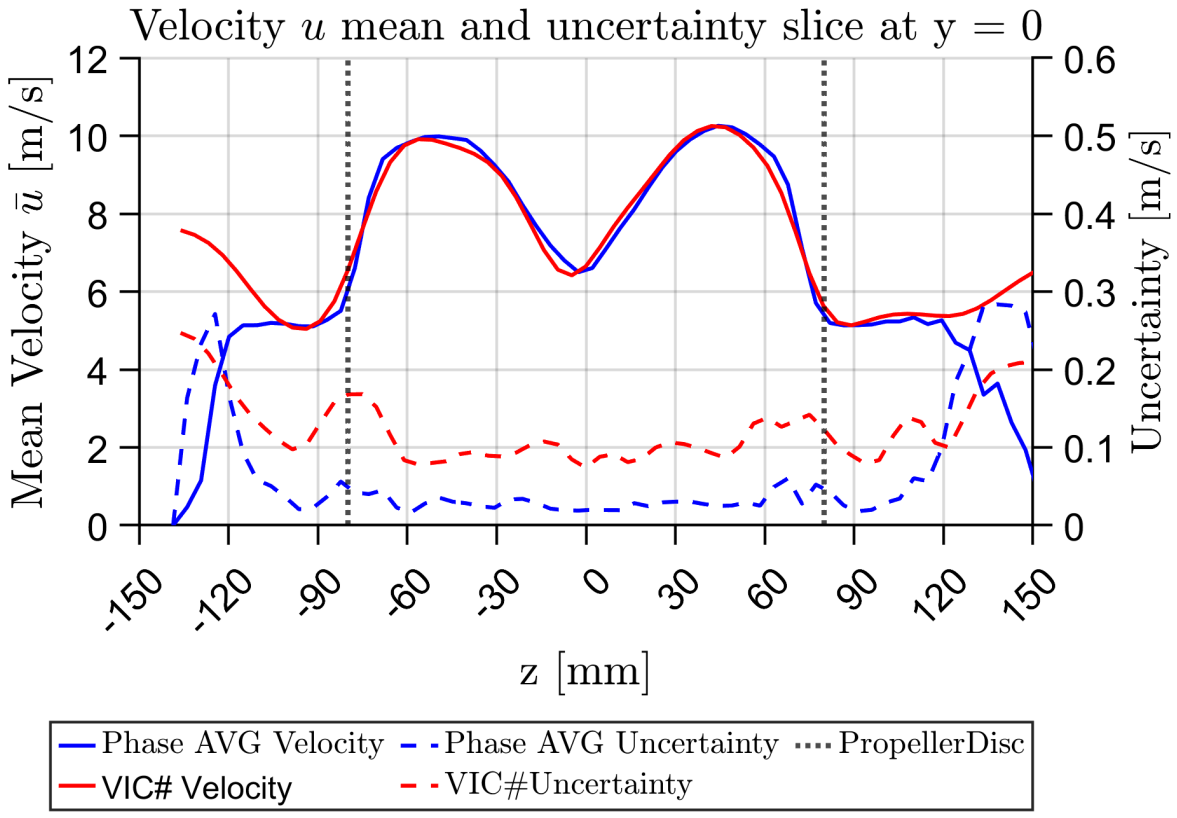

Figure 5.8: Mean axial velocity $\bar{u}$ and its uncertainty for VIC# and phase average methods at x=0, y=0.

From the previous analysis in this section, it can be concluded that the best reconstruction method is the phase average. Instantaneous binning is soon discarded for the inability to reconstruct the flow field accurately. Although it is still a good option considering the computing time and the simple implementation, the post-processing would be more tedious due to the

high noise. Moreover, VIC# displays an accurate and smooth reconstruction of the flow field. However, two main factors make phase average a better option. First is the computational time, as processing of one time-instant takes around 2000 times longer than the phase average. Second is the uncertainty of the reconstructed field. This uncertainty is a result of the used time instants for the method. While the phase average uses around 50 for each computed propeller's angle, VIC# only uses 1. Thus, the effective number of particles available for the reconstruction is 50 times lower. Overall, VIC# is a robust reconstruction method that falls behind the phase average in the mentioned two aspects. Nevertheless, it should not be disregarded as it dramatically improves the results from the polynomial interpolation in both accuracy and spatial resolution, and represents the best option for non-periodic flows. Finally, it is decided that the phase average will be the reconstruction method used for further analysis of the time-resolved flow in the following sections.

5.4. Vortex dynamics and wing-propeller interaction

The visualised effects related to vortex dynamics and wing-propeller interaction will be discussed in this section. First, the results of the slipstream effect on the wing will be presented in subsection 5.4.1, relating to the up- and downwash produced by the propeller and the effects that the wing experiences from this. Secondly, the effect of the wing on the propeller's tip helical vortices will be discussed. Thirdly, the visualised root vortex characteristics and breakdown induced by the wing will be analysed in subsection 5.4.3.

5.4.1. Propeller slipstream interaction

The rotating effect of the propeller will affect the flow encountered by the wing. As discussed in chapter 2 the up-going blade will create an upwash effect on the wing while the down-going blade will generate a downwash. The up- and downwash produced by the propeller can be seen at a location in front of the wing in Figure 5.9. The figure plots the w velocity component that is entirely produced by the rotation of the wing. Regions shown in green are where the velocity is going up, and hence, an upwash is generated. At the same time, the red colour represents velocity going in the negative z direction where a downwash is generated. The results show that a stronger up- and downwash is produced at a distance between y = $\pm$15 and y = $\pm$30. Although the case displayed is with the wing at $\alpha = 0°$, the behaviour is similar in all cases.

The up- and downwash produced by the propeller would essentially generate a positive and negative AoA respectively, when the wing is at $\alpha = 0°$. Thus producing lift in the opposite directions that would compensate one side with the other. The results are able to display this behaviour; in fact, Figure 5.10 shows that there is an increase in velocity over the wing at the location where upwash is being produced (negative y). This increase in velocity resembles the increase produced at the suction side of an airfoil generating lift. Although camera accessibility does not allow to watch what would be the suction side of the wing, the flowfield should show similar behaviour as it is a symmetric wing profile.

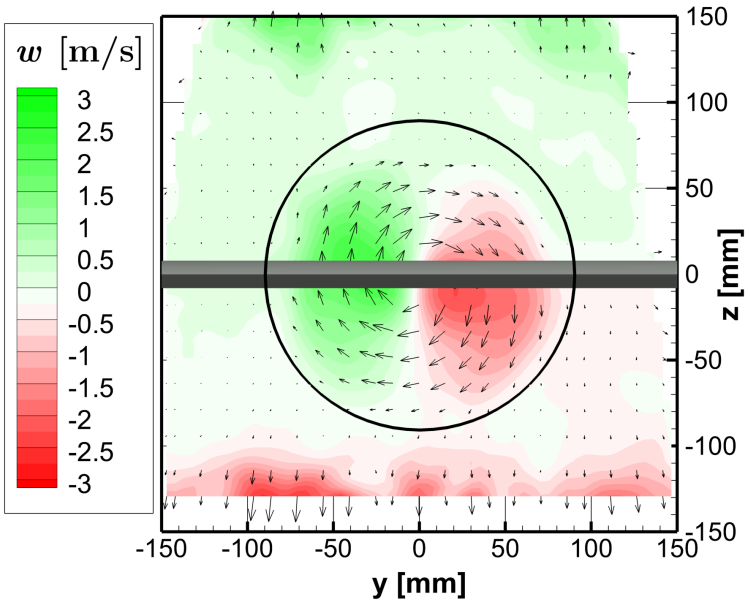

Figure 5.9: w velocity contour at x = 155mm just in front of the wing at $\alpha = 0°$ and $\omega =$ 5200RPM. Wing and propeller shades are presented for reference in grey shade and black line respectively. Green represents upwash, while red represents downwash. In plane vectors show flow direction.

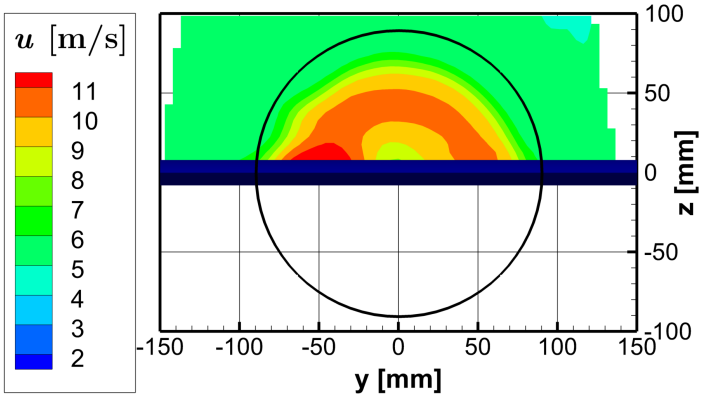

Figure 5.10: Axial velocity u time-averaged contour over the wing at $\alpha = 0°$ at the quarter chord location x = 200mm and propeller rotational velocity $\omega =$ 5200RPM.

With vertical velocities as high as those presented in Figure 5.9, the effective angle of attack could change up to 18 degrees depending on the local streamwise velocity. Thus, it is decided to further analyse this effect with the effective angle of attack produced by the propeller when the wing is at $\alpha = 0°$. The effect can be better understood when looked upon throughout the slipstream as displayed in Figure 5.11. Here, the computed angle is visualised at the spanwise locations of the wing where the highest vertical velocity is encountered (y = $\pm$20 mm). Although the effect of the downwash region producing lift could not be seen in Figure 5.10, Figure 5.11b shows a downwash region on the wake of the wing, this downwash is encountered on the wake of wings producing lift. This confirms the expected conclusion that the effect is

symmetrical for the up- and downwash region of the wing.

Furthermore, as displayed by the AoA distribution, the effective flow velocity can vary more than 16° at some locations in either direction. However, this increase is not experienced throughout the whole inlet of the airfoil which results in a decreased impact on effective AoA of the wing. Consequently, the effective change is, in fact, smaller than 10°. This can be confirmed as no characteristics of positive lift were visualised in any area of the wing when placed at $\alpha = -10°$. The effect, however, is likely large enough to stall the wing at the upwash region at $\alpha = 10°$; this consequence is further discussed later on.

It is important to remember that the position of the cameras at positive z means that the cameras did not have access behind the wing, and as such, any information there is unreliable. Hence, no conclusions should be made from flow information there.

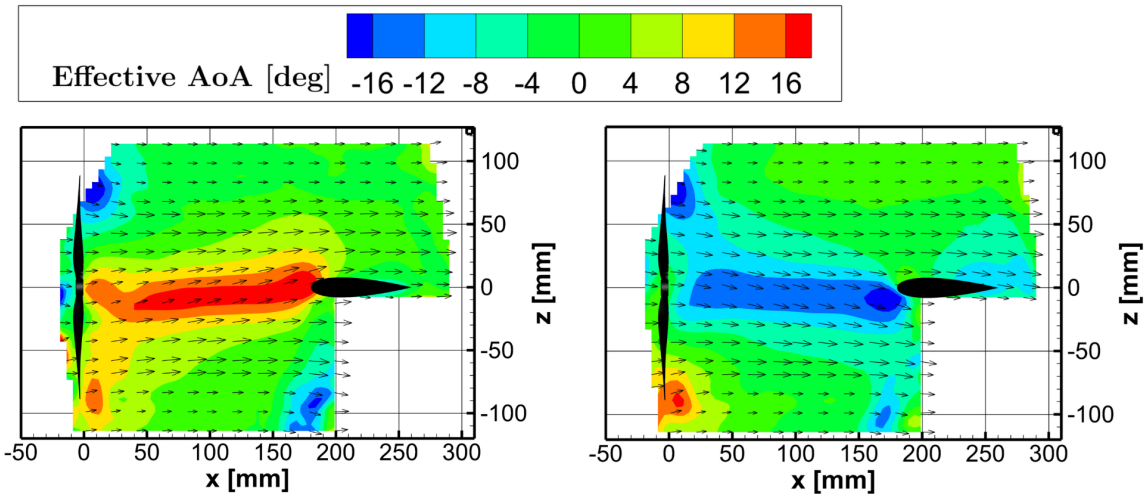

(a) Computed AoA at y = -20mm. **(b)** Computed AoA at y = 20mm.

Figure 5.11: Effective AoA altered by the propeller's rotation at locations y = ± 20mm where the vertical velocity is highest. Contours are displayed for time-averaged flowfield with the wing at $\alpha = 0°$ and $\omega = 5200$RPM.

The effect of the propeller's rotation creates an upwash that could stall the region where the highest vertical velocity is experienced. To analyse this behaviour, the streamwise velocity contours for the wing at $\alpha = 10°$ are displayed in Figure 5.12. A NACA 0020, as tested by De Paula [55] at a Reynolds number of the same magnitude as the present one (Re = 500,000), will begin to stall beyond $\alpha = 12°$. Being a thick airfoil, it will likely stall by trailing edge separation, as seen in Figure 5.12a. Although the flow reversal on top of the airfoil cannot be seen, there is a large decrease in velocity from the mid-chord location downstream. The lack of definition for the flow reversal is due to the large-scale PIV (for reference bin size is shown at the top right corner of Figures 5.12a and 5.12b). As mentioned in chapter 3, using HFSB does not allow to resolve small vortical structures and is not very accurate in defining flow close to the wall. Moreover, to be able to assess the separation over the airfoil, Figure 5.12b shows the same flow at the location where downwash is encountered. It can be seen from the figure that the flow in this case is attached; hence, a greater velocity peak is also encountered on top of the airfoil.

It can be concluded that the slipstream rotation effect on the wing may seem high at first glance, with the effective angle of attack reaching values higher than 18 degrees. However, after a deeper analysis, it is confirmed that the effective value experienced by the wing is lower than 10°. Although the effect will likely be balanced by both sides of the propeller, it must not be undermined as it has the potential to stall the wing when placed at high angles of attack.

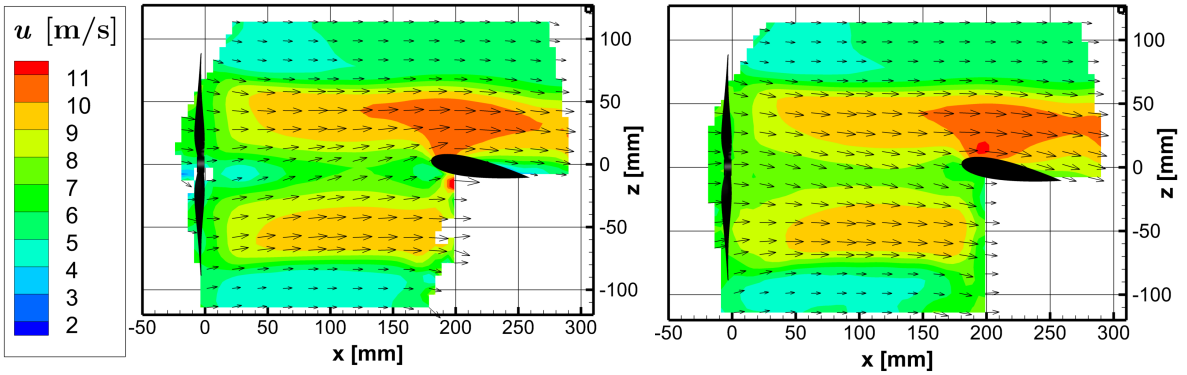

(a) Axial velocity at location y = -20 mm.

(b) Axial velocity at location y = -20 mm.

Figure 5.12: Axial velocity u time-averaged contours at locations y = ± 20mm where higher up- and downwash is encountered. Wing placed at $\alpha = 10°$ and rotational velocity of $\omega =$ 5200RPM.

5.4.2. Wing's effect on helical vortex system.

The phase-averaged flow field is used to understand how the wing affects the helical vortex system. Figure 5.13 shows the helical vortices displayed as contour lines at three different y-plane locations and three different wing AoA. An important consideration to take into account is that the slices are taken at positive y locations; as a consequence flow is located at the region where downwash is present. Although downwash is low at the edge of the streamtube, it is still a factor that must be considered when looking at these results. The vortices at negative values of y are not presented, as the effect of the pylon's wake does not allow the helical vortices to be accurately seen.

It can be seen that the contour lines are evenly spaced for all cases when close to the propeller. This remains true for the entire length of the flowfield when looking at y/R = 0.47 (Figure 5.13a). However, moving further away from the propeller centerline, the helical vortices start to be closer to the wing, where the latter induces velocities in the flowfield that affect the vortex structure.

At y/R = 0.58 (Figure 5.13b), the last visible vortices at x = 240mm are not aligned anymore as an effect of the wing's favourable and adverse pressure gradient at the wing's pressure and suction side respectively that alter the flow velocity. The green vortex has a larger distance with respect to the second to last one, whereas the red vortex shows a shorter distance. In this case, the black vortex with the wing placed at $\alpha = 0°$ serves as a reference in the middle of both vortices.

The wing's induced effect on the helical vortex system becomes even clearer when the vortices get closer at y/R = 0.7 (Figure 5.13c). Here, the induced velocities by the wing affect both the last and second-to-last vortices in the flowfield in the x and z directions. It can be seen that the suction side of the wing has a higher impact on the location of the vortex closer to the leading edge (second to last vortex) than further downstream. On the other side, the red vortex shows that the suction side of the wing has a lower effect closer to the leading edge. Further downstream, the position of the red vortex is likely altered by both the wing's induced velocity and the downwash created by the propeller, which is also reflected by the wing's wake. The latter is believed to be also the reason why in Figure 5.13a, the last red vortex is misaligned with the other two.

It can be concluded that it is possible to see the wing's induced effect on the helical vortex system and that this effect becomes much clearer when the vortices are closer to the wing. Moreover, the wake's rotation effect also has an apparent effect on the helical vortices when combined with the wing's induced effects.

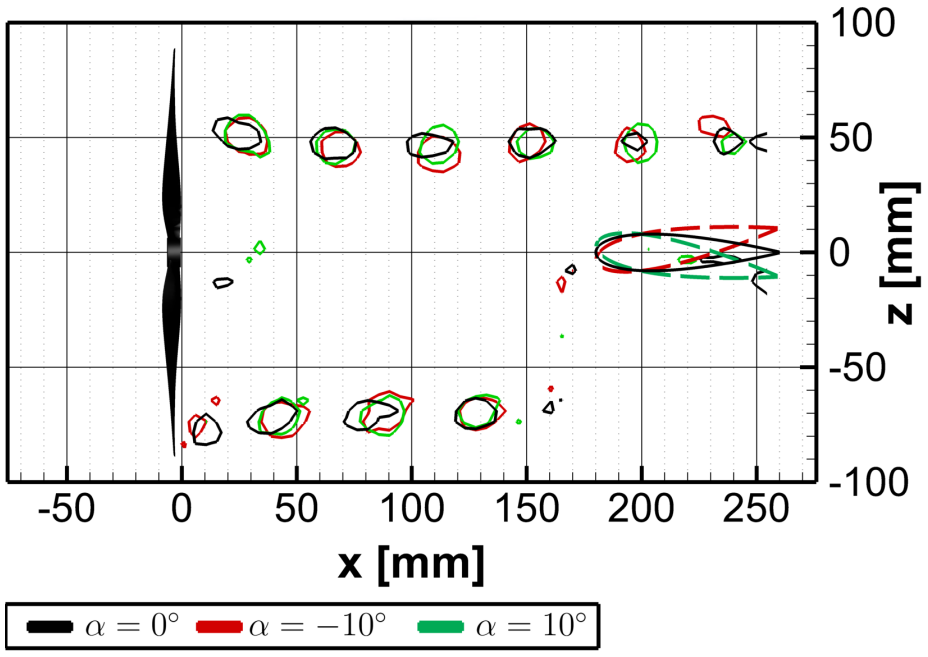

(a) Slice at y/R = 0.47 .

Figure 5.13: Vorticity Contour Lines at various y locations and $|\omega_v|$= 400 1/s for wing angles of attack of $\alpha = 0°$, α = -10° and $\alpha = 10°$. (continues on next page)

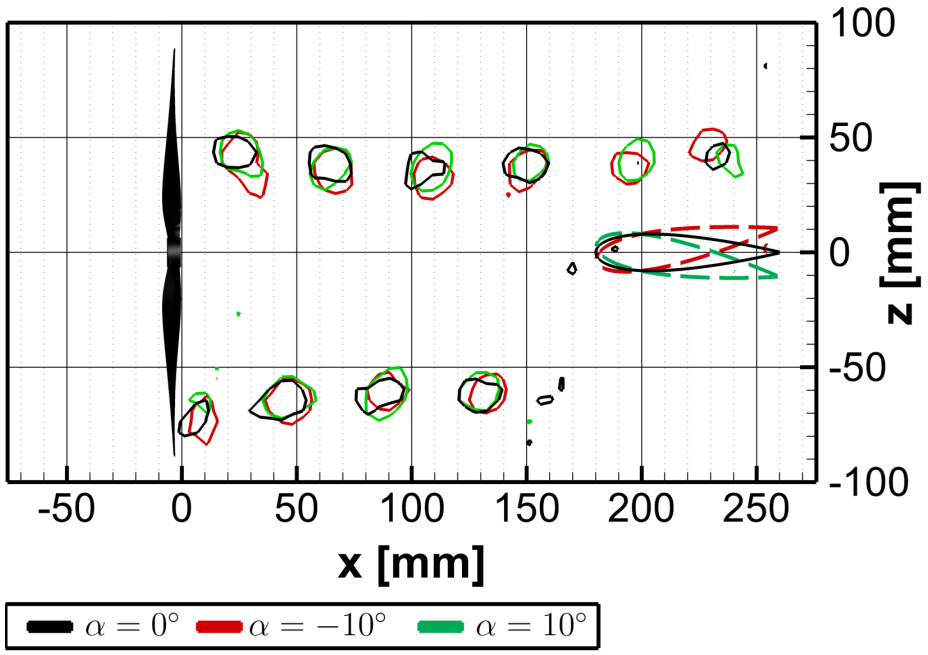

(b) Slice at y/R = 0.58.

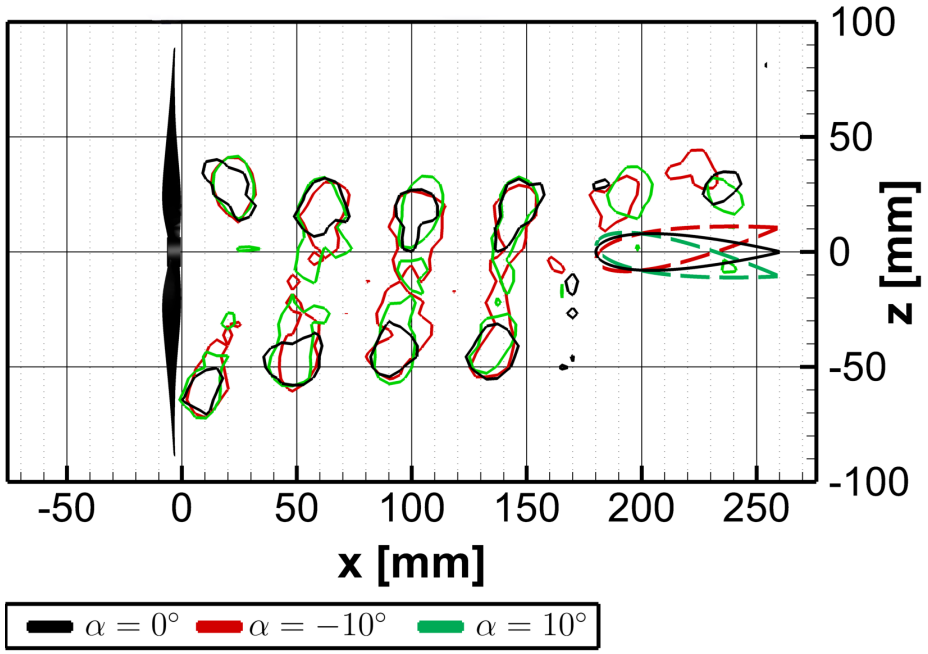

(c) Slice at y/R = 0.7.

Figure 5.13: Vorticity Contour Lines at various y locations and $|\omega_v|$= 400 1/s for wing angles of attack of $\alpha = 0°$, α = -10° and $\alpha = 10°$.

5.4.3. Root vortex visualisation

Depending on the propeller's loading conditions and the geometry of the blades, the root vortices could rapidly fade away and not be clearly identified from the hub vortex [56]. In this case, with a straight-blade propeller and medium disc load, the two vortices can be identified from each other. Figure 5.14 displays the root vortex system when plotting the iso-surface of the Q criterion at Q = 7000 $1/s^2$ when no wing is installed. It can be seen that the root vortices are affected by the tangential velocity of the propeller and, as a consequence, roll up in a helical structure similar to the tip vortices. Root vortices in the aerospace field are not commonly identified separately from hub vortices as the propeller is most commonly placed in tractor configuration. In this case, the root vortices are greatly affected by the nacelle, and the encountered vortex downstream is a mix of both effects.

Furthermore, Figure 5.14 shows how the trailing vortices from the blades merge into the root vortex. When looking at the tangential velocity cuts at various x locations (see Figure 5.15), it can be seen more clearly the three vortices with a peak in tangential velocity followed by a dip on the other side of the core. Although the vortices have some interaction and the changes in tangential velocity are not as clear, the peaks of the Q criterion clearly show where the vortex core is located. As expected and also taken from the iso-surface, the root vortices (smaller peaks left and right of the biggest peaks) have a smaller core radius and show a lower tangential velocity. Beware that the base tangential velocity is not zero but a negative value due to the propeller's rotation.

From this data, it is insightful to understand that the vortex structure does not merge or breakdown in the entire field of view. This will become of interest later on when the wing is placed, as any disturbance to the vortices will be caused by the presence of the wing. This is shown in the iso-surface and confirmed when looking at the tangential velocity profiles.

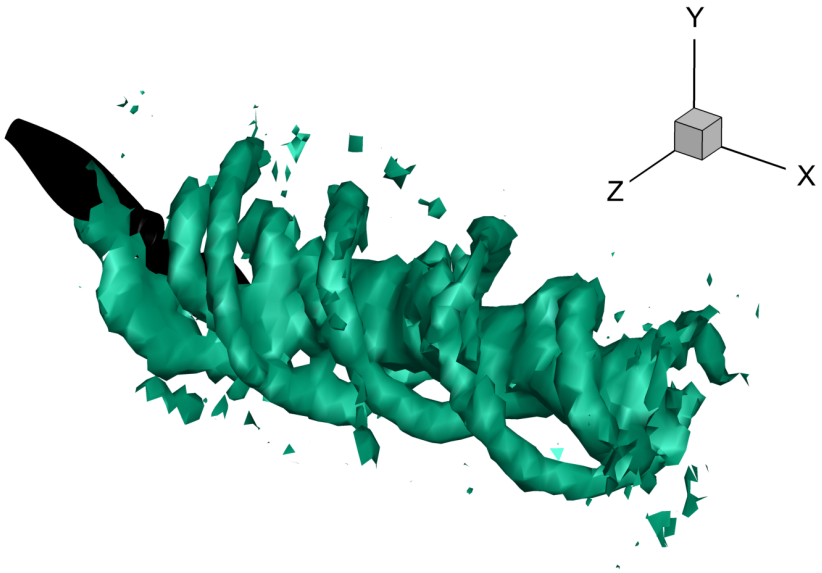

Figure 5.14: Root vortex structure displayed as an iso-surface of the Q criterion at Q = 7000 $1/s^2$ for the phase-averaged no wing case at ω = 5200RPM.

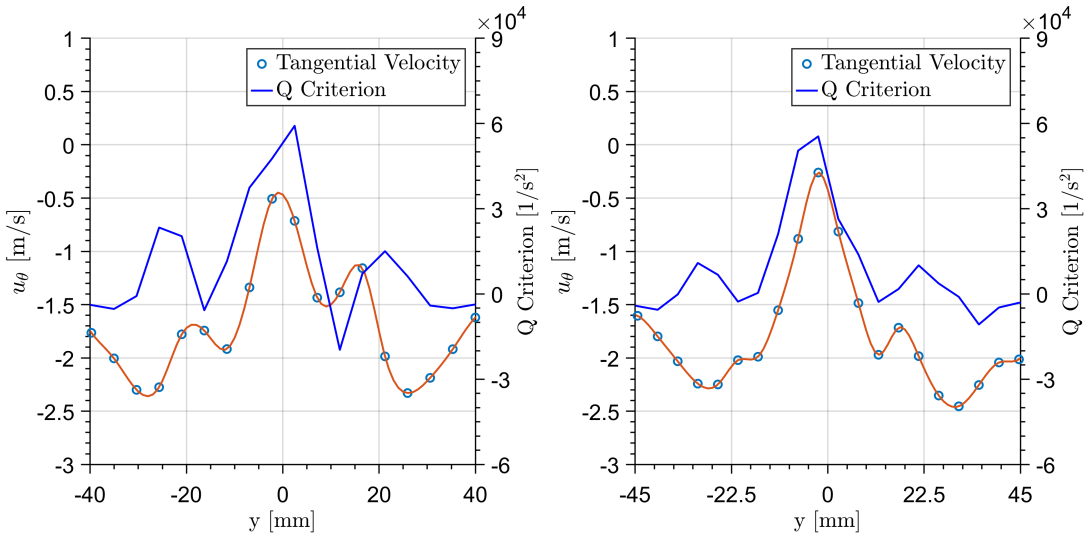

(a) Tangential velocity and Q criterion at x = 168mm and ω = 5200RPM.

(b) Tangential velocity and Q criterion at x = 235mm and ω = 5200RPM.

Figure 5.15: Root vortex tangential velocity and Q criterion at two different x locations.

With the wing placed in the flowfield, vortex breakdown caused by the adverse pressure gradient of the wing can be identified. Figure 5.17 shows the iso-surface of axial vorticity $\omega_{v\_x} = -250$ 1/s at different wings' angle of attack. It is important to remark that although both iso-surfaces show a vortical structure, the Q criterion used in Figure 5.14 must not be confused with the axial vorticity shown here. In each case, the correspondent parameter is chosen arbitrarily, choosing the one that displays the desired visualisation of the vortex in a better way; hence, both plots should not be directly compared.

The vortex breakdown caused by the wing is believed to happen in a similar way as reported by Gordnier and Visbal [57] where a flat plate breaks a delta wing vortex and later by Garmann and Visbal [22] where a tip vortex impinges on a NACA 0012 wing. In both cases, the vortex bifurcates in a double spiral that ends with a smaller vortex on each side of the surface. The results from Gornier and Visbal [57] are shown in Figure 5.16 for reference. It can be seen how the adverse pressure divides the vortex into two spiral structures, and one goes to each side of the plate, where it later breaks.

It is possible to see at $\alpha = 0°$ (Figure 5.17a) how the vorticity keeps going on top of the wing with a smaller and weaker vortex core. The vortex is most likely breaking due to the adverse pressure gradient in front of the wing and later recovering partly on top of the wing with the favourable gradient. Although, due to visual access, it is not possible to confirm that the other side of the wing shows the same behaviour, it is believed to be happening since it is a symmetric profile. Additionally, a similar vortex ramification is seen on the underside front of the wing, which suggests the double spiral breakdown is happening.

When the wing is placed at $\alpha = 10°$, the adverse pressure gradient in front of the wing will increase. In this situation, the vortex will certainly break down as shown in Figures 5.17b and 5.17c. In this case, it is possible to confirm more accurately the double spiral breakdown as both the suction and the pressure side of the wing are shown. Although both iso-surfaces do not display the exact same run, having the wing at $\alpha = -10°$ should represent the same as

looking at the bottom of the wing at $\alpha = 10°$ and thus, the comparison is deemed acceptable. The presence of the vortex on top of the wing was confirmed by looking at time-averaged values from the flowfield.

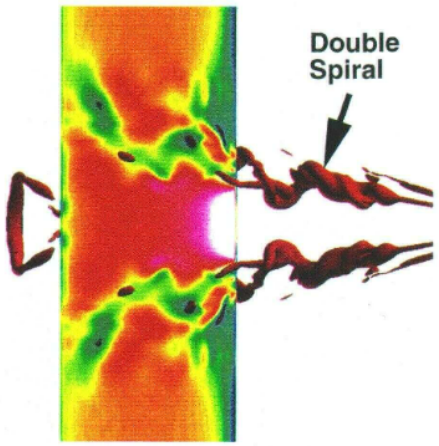

Figure 5.16: Double helical vortex breakdown in front of flat plate [57].

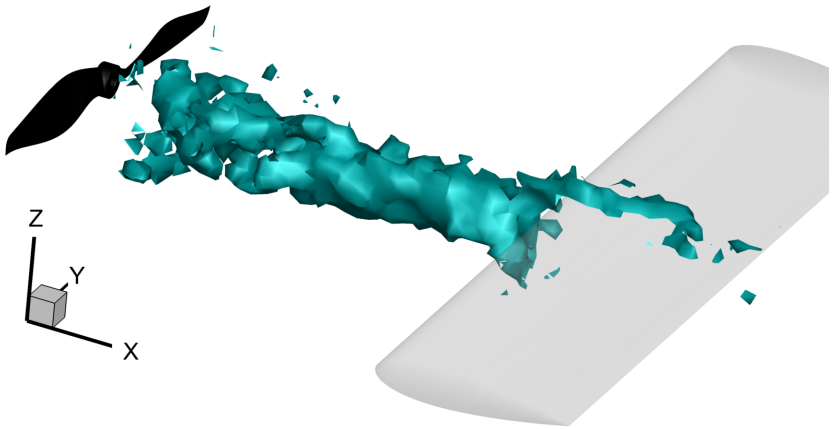

(a) Vortex breakdown iso-surface of $\omega_{v\_x} = -250$ [1/s] and wing at $\alpha = 0°$.

Figure 5.17: Root vortex phase averaged iso-surfaces of axial vorticity at $\omega_{v\_x} = -250$ 1/s and $\omega = 5200$RPM displaying the vortex breakdown caused by the wing different angles of attack. (continues on next page)

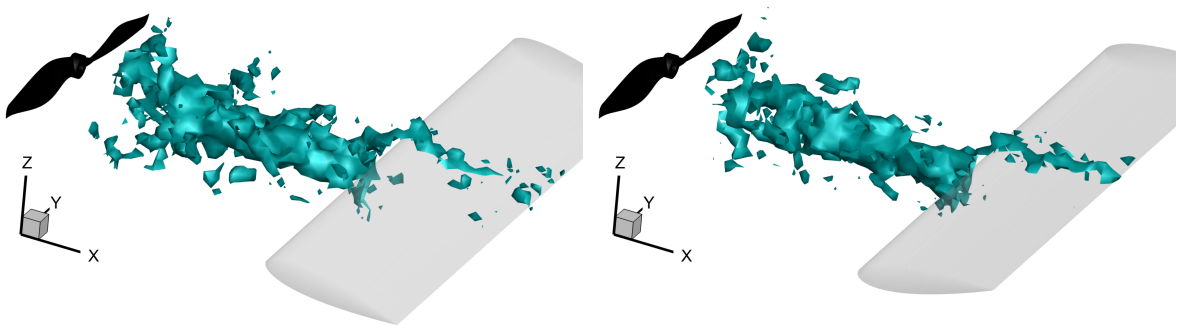

(b) Vortex breakdown iso-surface of $\omega_{v\_x} = -250$ [1/s] and wing at $\alpha = 10°$.

(c) Vortex breakdown iso-surface of $\omega_{v\_x} = -250$ [1/s] and wing at $\alpha = -10°$.

Figure 5.17: Root vortex phase averaged iso-surfaces of axial vorticity at $\omega_{v\_x} = -250$ 1/s and $\omega = 5200$RPM displaying the vortex bifurcation caused by the wing different angles of attack.

When the bifurcation is looked at from the top of the wing, some extra information can be seen. Figure 5.18 shows both the pressure and suction side of the wing ($\alpha = -10°$ and $\alpha = 10°$ respectively) with the vorticity iso-surface from the top. Garmann and Visbal [22] reported that the resulting vortices will move in the spanwise direction of the wing in opposite directions. This effect can be seen on the suction side (Figure 5.18b) where the vortex moves in the negative y direction from the leading edge to the trailing edge. Moreover, this effect is not as clearly seen on the suction side (Figure 5.18a); the reason behind this is that the vortex does not survive until the trailing edge, but it dissipates along the chord. The cause of the breakdown is very likely the adverse pressure gradient present on top of a NACA 0020 wing at $\alpha = 10°$. It is believed that the vortex breaks in front of the wing, then it reforms at the leading edge of the wing with the favourable pressure gradient; however, at this point, it is not strong enough to sustain the adverse pressure gradient further downstream of the wing.

It is important to emphasise why the double spiral breakdown is not as clearly seen in the experimental results as the reference one. Since the results presented are phase averaged, it is possible that the frequency of the breakdown is not the same as the propeller rotation. As such, the breakdown is seen more as time-averaged than time-resolved. The breakdown was analysed with the VIC# results to get a time-resolved flow accurately. However, the lower spatial resolution, due to the lower number of particles per time instant, also does not allow to clearly see the double spiral breakdown as in the reference image.

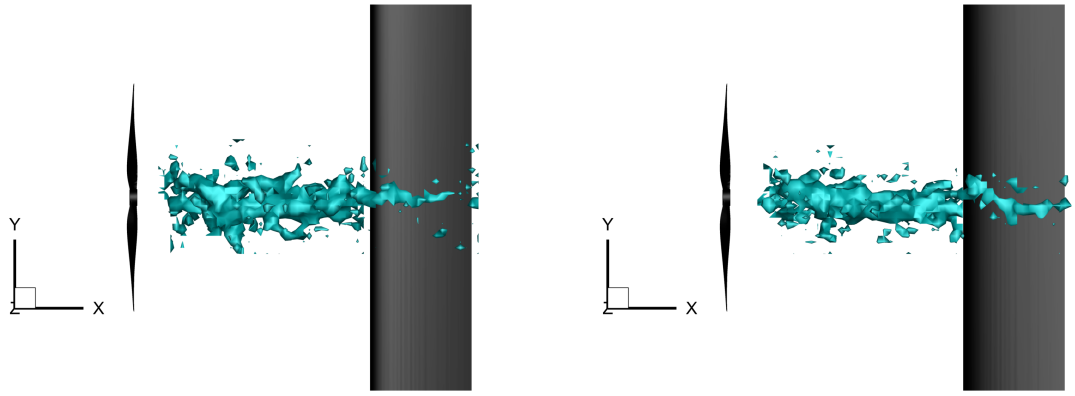

(a) Vortex breakdown top view with wing at $\alpha = 10°$.

(b) Vortex breakdown top view with wing at $\alpha = -10°$.

Figure 5.18: Root vortex phase averaged iso-surfaces of axial vorticity at $\omega_{v\_x} = -250$ 1/s and $\omega = 5200$RPM displaying the vortex breakdown over the suction and pressure side caused by the wing at $\alpha = 10°$.

To further analyse how the breakdown is occurring, it is useful to look at the axial vorticity contours on an x-plane. This is presented in Figure 5.19 at three different x locations. One far upstream of the wing where the wing's effect is not yet visible (Figure 5.19a). The second one is 10mm upstream of the wing, where the adverse pressure gradient affects the vortex (Figure 5.19b). Moreover, the third one is on top of the wing at the quarter chord location where the vortex is reformed (Figure 5.19c).

It can be seen how the adverse pressure gradient in front of the wing expands the vortex core, where the overall vorticity is reduced. At this point, it is believed that the vortex will break down. Although it is not possible to see the positive vorticity that Garmann and Visbal [22] mention at the core when the breakdown occurs, the expansion in decay in vorticity is believed to be the vortex breakdown. This condition is likely met in the simulation, but the resolution from the STB method is not high enough to capture this phenomenon.

Furthermore, it can be seen that on top of the wing, the vortex is reformed and has a higher vorticity than in front of the wing. This result affirms what was previously discussed about the vortex rearranging on top of the wing as a consequence of the favourable pressure gradient. Finally, it is important to remark that the full discussion on vortex breakdown is done on the hub vortex and does not consider the root vortices. The resolution of the root vortices is not high enough to make conclusions on how they are behaving in presence of the wing, and as such, it is not discussed.

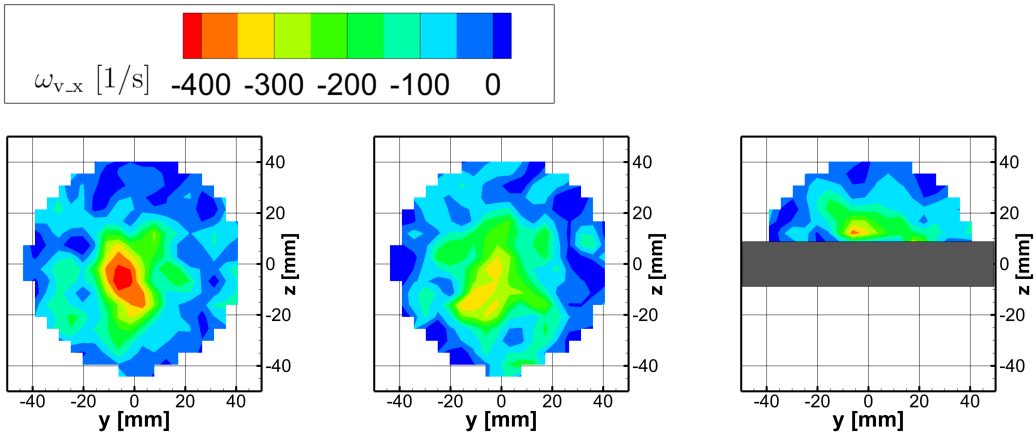

(a) Contour at x=140mm. **(b)** Contour at x=170mm. **(c)** Contour at x=200mm.

Figure 5.19: Phase averaged axial vorticity contours of the root vortex at various x locations, $\alpha = 0°$ and $\omega = 5200$RPM. Contours display vortex breakdown and reformation on top of the wing.

Although having the wing at $\alpha = 90°$ does not represent a realistic operating condition, observing the vortex breakdown becomes interesting when a higher adverse pressure gradient is generated. Figure 5.20 presents the axial vorticity and swirl angle contours when the wing is placed at 90 degrees. It can be seen that the higher adverse pressure causes the vortex to break further upstream (around x = 120 mm compared to x = 170 mm at any other AoA). Moreover, the axial vorticity distribution shows how the increased pressure gradient causes the breakdown to have a sudden expansion, which causes a rapid dispersion of the vorticity.

Additionally, the swirl angle contours give insight into the achieved swirl angles in the vortex structure. It can be seen that the critical value of swirl angle $\theta_{sw} = 50°$, mentioned in section 2.4, is reached later than where the vortex is considered to start the breakdown (orange and red regions in Figure 5.20b). It is important to remember that this value is a critical value at which vortex breakdown will occur, but it is not the only possible cause for it to break down. In this specific case, it can be seen that the vortex breakdown occurs before the critical value is reached as a consequence of the pressure gradient.

Moreover, the case at $\alpha = 90°$ gives a clear insight into the capabilities to observe vortex breakdown through LPT. The breakdown is more clearly seen when looking at the core's vorticity in Figure 5.21. The vortex core is concentrated far upstream at x = 100mm (Figure 5.21a). Further downstream, where the breakdown begins to occur (Figure 5.21b) the core expands, and the peak in vorticity inside the core is reduced considerably. Finally, when the core is observed at x = 150 mm (Figure 5.21c) it can be seen that the vorticity has dissipated, and the vortex core is no longer clearly defined anymore. In contrast to the rest of the cases, the positive vorticity (in blue) inside the core upon breakdown, mentioned by Garmann and Visbal [22], can be seen from both the y and x planes(Figure 5.20a and Figure 5.21c respectively).

It can be concluded that the STB method gives a good insight into the root vortex structure, with the capacity to show the breakdown of the vortex. Moreover, it has the capability of differentiating the hub vortex from the root vortices and its behaviour along the axial direction.

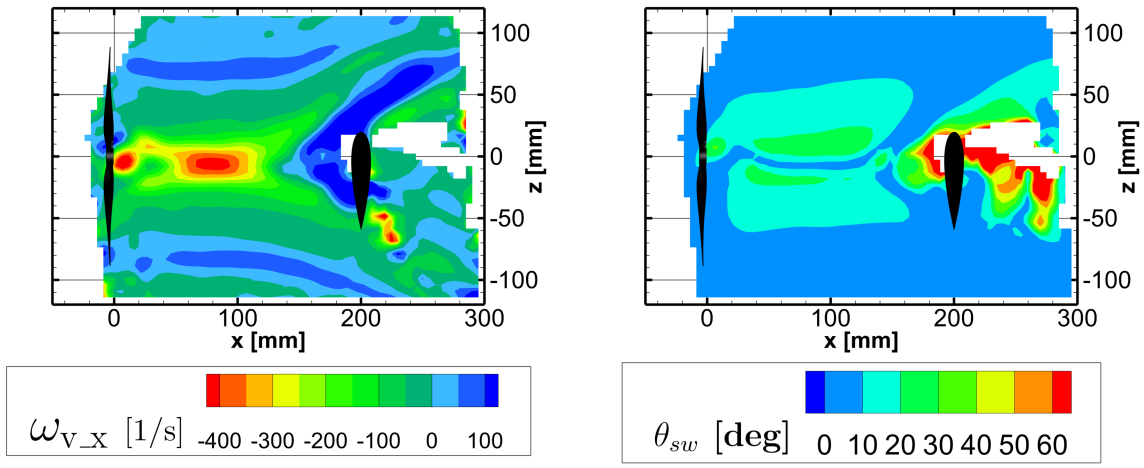

(a) Axial vorticity contour at y = 100mm.

(b) Swirl angle contour at y = 0mm$\alpha = -10°$.

Figure 5.20: Root vortex time averaged contours of axial vorticity and swirl angle at $\alpha = 90°$, $\omega = 5200$RPM and y = 0mm.

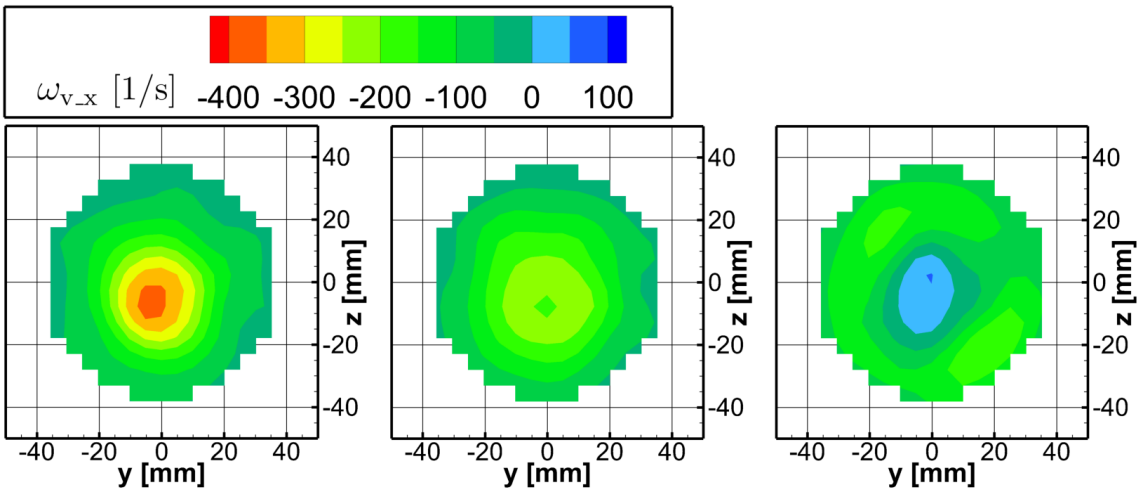

(a) Contour at x=100mm. **(b)** Contour at x=120mm. **(c)** Contour at x=150mm.

Figure 5.21: Time averaged axial vorticity contours of the root vortex at various x locations, $\alpha = 90°$ and $\omega = 5200$RPM.

6

Conclusions & Recommendations

In this chapter, conclusions and recommendations for future work based on the obtained results will be discussed. The research objectives and questions are presented again, and the conclusions intend to answer the latter based on the observed results.

6.1. Conclusions

The objective of this research was to reconstruct the flow field around a wing-propeller configuration, resembling a scaled-down version of the Cessna Skymaster 337 pusher propeller and horizontal tailplane configuration. The reconstruction was carried out employing Large Scale PIV and Lagrangian Particle Tracking in a low turbulence wind tunnel environment at a 1:10 scaled version of the aircraft. The results showed that the flow field could be reconstructed with a high spatial and temporal resolution, and as such, some conclusions from the experimental campaign were drawn.

As a guide to the conclusions, the research questions initially presented in chapter 1 are revisited, with each of them being addressed individually. This approach allows for a comprehensive response to each question, contributing to the formation of a conclusive assessment of the overarching research objective. This systematic examination not only underscores the research's significance but also demonstrates the depth of understanding achieved during the study.

Q I. *To what extent can the Lagrangian Particle Tracking method characterise a propeller-wing interaction flow?*

Q I.i. **What particle concentration can be achieved after the propeller?**

The experimental campaign showed that high particle concentration values can be achieved after the propeller disc. The initial expectations were that a considerable amount of particles would be affected when passing through the propeller disc. The research proved the case to be the opposite, showing that concentration values can be higher inside the propeller disc than outside. On top of that, the rotational velocity imposed by the propeller proved to improve the spread of particles more evenly further downstream inside the streamtube.

Moreover, the achieved concentration values between C = 1 particle/cm^3 and C = 7 particles/cm^3 proved to be of the same order of magnitude as the initially calculated value between C = 7.8

particles/cm^3 and C = 19.5 particles/cm^3 and that the lower obtained value is a consequence of the seeding system rather than the propeller disc.

Finally, it can be concluded that the particle concentration distribution is highly affected by the seeding system itself. The experimental campaign proved that the propeller does not have a detrimental effect on this factor but rather improves the particle distribution. Subsequently, this behaviour will most likely be encountered when testing at a full-size aircraft, as the propeller rotational velocity is lower. Nevertheless, as a consequence of the larger flowfield, particle concentration values might also decrease.

Q I.ii. **What is the velocity resolution achieved for a wing-propeller configuration?**

The experimental methodology involving the STB method and post-processing done through phase average and VIC# methods proved to achieve high velocity resolution. Both methods were compared with an uncertainty analysis at a 95% confidence interval and presented a velocity uncertainty lower than 3% throughout the flowfield.

In this aspect, the phase average methodology proved to have higher precision than the VIC# methodology, with values less than half of the uncertainty throughout the flowfield. This results from the higher available particle information for each resolved phase when implementing a temporal bin.

Q I.iii. **Can the vortex dynamics shed by the propeller be resolved?**

Three field reconstruction methods (Binning with polynomial interpolation, Phase Average and VIC#) were compared on their capabilities to reconstruct the propeller flowfield accurately. All three methods showed an accurate flow reconstruction and the capability to show the vortex system shed by the propeller.

Moreover, out of the three, the phase average method showed the best overall performance when a periodic flow is analysed. Providing a smooth reconstruction of the tip helical vortices, a clear differentiation between the root and hub vortices of the propeller, not commonly seen in the aerospace field, and a high spatial resolution. All without compromising on the computational effort, proving to be as much as 2,000 times faster to reconstruct a single time-instant compared to VIC# while using 50 times more information.

Nevertheless, the other two methods should not be undermined as they represent great alternatives to the phase average for different applications. The binning is a simple yet reliable way to analyse the flowfield in the initial approach. It could reconstruct the main characteristics of the flow, although the amount of noise would make the post-processing a tedious task. On the other hand, the VIC# proved to reconstruct the flow in a time-resolved manner accurately. Although computationally expensive, it is the best alternative to reconstruct a non-periodic flow and should not be undermined.

As mentioned, the concentration values may decrease once the flow field is extended to the full-scale aircraft. In this case, it is possible that the vortex system is not as fully reconstructed

as in the scaled-down version. However, having a larger propeller will also increase the size of the vortical structures. This will likely allow the particles to follow high-velocity phenomena such as the vortex breakdown.

Q II. *How robust is the method to characterise wing-propeller flow characteristics?*

Q II.i. **How accurate is load determination through the control volume approach based on LPT method, compared to other methods?**

The propeller thrust and torque were computed through a control volume approach based on conservation of momentum. Results show that both parameters provide typical uncertainty values when calculated based on the PIV measurements, and the resulting values coincide with the reference values provided by the propeller's manufacturer and the tested values at the wind tunnel. It is important to remark that the results were accurate for all cases except for the torque calculation when the advance ratio was increased. Likely, the in-plane velocity reconstruction in this case was not as accurate as at lower values of J. As such, at advance ratios, results should be treated with extra care.

The technique showed that accurate results require a full reconstruction of the streamtube flowfield, and as such, it should be implemented far downstream of the propeller. Results showed that at axial positions of $\mathrm{x}/D > 1$, the flowfield stabilises, and the computed values begin to converge. Measuring at such axial position values will likely pose a challenge when testing in the full aircraft with the impossibility of removing the horizontal stabiliser.

It can be concluded that PIV-based experiments have a great potential to determine rotors' thrust and torque in a straightforward approach. The technique's non-invasive nature allows for the performance of thrust and torque measurements without altering the test model to install loading cells or balances.

Q II.ii. **Can the wing's induced effects be observed on the vortex structure through the LPT measurements?**

The wing's effect on the slipstream's vortex structure was analysed for several wing angles of attack. The adverse pressure gradient created by the wing upstream of the leading edge proved strong enough to cause a breakdown on the root vortex. This phenomenon was visualised for all angles of attack, forming a double spiral breakdown that causes two smaller vortices to form on either side of the wing. With an exception at $\alpha = 90°$ where the higher adverse pressure gradient caused an earlier and stronger breakdown, dissipating the vorticity faster upon breakdown.

Moreover, the wing's induced velocities affected the tip helical vortices when these approached close to the surface. At positive AoA, the vortices gap between each set increased due to the increase in velocity, whereas the gap decreased at negative angles of attack.

Lastly, the effect of the pylon must be considered as it displayed disruption in the visualisation of the tip vortices. As such, a similar effect may be seen when performing similar measurements with different structures upwind. Moreover, the increase in scale could increase phenomena such as the reverse in vorticity at the breakdown location, allowing the method to capture this phenomenon.

Q II.iii. **Can the propeller's induced effects on the wing be observed through the LPT measurements?**

When the flow over the wing was observed, upwash and downwash caused by the propeller rotation were identified. The effect of the up- and downwash had the strength to affect the effective AoA as much as 16° at some locations of the flowfield. However, the effective change in the wing's AoA proved to be smaller and did not surpass 10°.

At high AoA, the effect showed an angle increase that stalled the wing locally and was identified through trailing edge separation on the suction side of the wing. Finally, it can be concluded that the flowfield is reconstructed in an accurate enough manner to identify what effect the propeller is inducing on the wing by being placed at its slipstream.

6.2. Further Recommendations

During this research, some limitations were identified, and some additional parameters would prove to enhance the results obtained. Consequently, the following recommendations are posed for future research on PIV-based wing-propeller interaction flow.

1. Although the concentration values were high enough to reconstruct the flowfield, the lack of data on the concentration upwind of the propeller does not allow to quantify how many particles are lost passing through the propeller disc. As such, the flowfield should be extended to calculate the concentration before and after the propeller disc. Moreover, extending the flowfield further downstream would also allow visualising how the vortex behaves after the wing. Allowing to identify if it truly dissipates on top of the wing or if it keeps moving downstream.

2. The pylon's wake did not allow to accurately identify the helical tip vortices at the region where the wing was experiencing upwash. Although the effect is likely similar to the downwash region, using a propeller spinning in the opposite direction would give an exact comparison of how the tip vortices are affected by the up- and downwash of the rotation independently.

3. Having the cameras on one side of the wing reduced the field of view, impeding the reconstruction on the other side of the wing. As such, a rearrangement of the cameras is proposed in which the wing is observed from the spanwise direction. In this way, the flow could be reconstructed on both sides of the wing, obtaining time-matching information on the effects on the suction and pressure side of the wing.

4. The calculated torque value, when the advance ratio value was increased, showed some deviation from the expected value. As such, a test at higher advance ratio values of the

propeller is proposed to asses whether the exception was a disruption in that specific run of this experimental campaign or whether the method should be adjusted for higher advance ratios.

5. As mentioned, the propeller's thrust was calculated, considering the drag generated by the pylon and nacelle. Consequently, the calculated values of the thrust are lower than the real ones. To increase accuracy, it is proposed to perform a run at every freestream velocity used without the propeller spinning. By doing this, the value of the drag can be computed and added to the produced thrust of the propeller.

6. Although the manufacturer of the propeller provides the performance data of the propeller, it is provided for the isolated propeller, which does not necessarily behave in the same way. To improve the validation of this data, it is proposed to test the actual torque and thrust of the propeller as installed for the PIV measurements.

References

[1] E. Commission. *Reducing emissions from aviation*.

[2] EASA. *European Aviation Environmental Report 2022*. 2022.

[3] N. van Arnhem, R. de Vries, R. Vos, and L. L. M. Veldhuis. "Aerodynamic Performance of an Aircraft Equipped with Horizontal Tail-Mounted Propellers". In: *AIAA Aviation 2019 Forum* (2019). Publisher: American Institute of Aeronautics and Astronautics Inc. (AIAA). DOI: 10.2514/6.2019-3036.

[4] T. Sinnige. "Aerodynamic and Aeroacoustic Interaction Effects for Tip-Mounted Propellers: An Experimental Study". PhD thesis. Delft University of Technology, 2018. DOI: 10.4233/UUID:214E1E9A-C53E-47C7-A12C-B1EB3EC8293B.

[5] F. Scarano, S. Ghaemi, G. C. A. Caridi, J. Bosbach, U. Dierksheide, and A. Sciacchitano. "On the use of helium-filled soap bubbles for large-scale tomographic PIV in wind tunnel experiments". In: *Experiments in Fluids* 56.2 (2015), p. 42. ISSN: 0723-4864, 1432-1114. DOI: 10.1007/s00348-015-1909-7.

[6] D. Schanz, A. Schröder, S. Gesemann, D. Michaelis, and B. Wieneke. "'Shake The Box': A highly efficient and accurate Tomographic Particle Tracking Velocimetry (TOMO-PTV) method using prediction of particle positions". In: 2013, pp. 1–13.

[7] W. Terra, A. Sciacchitano, and Y. H. Shah. "Aerodynamic drag determination of a full-scale cyclist mannequin from large-scale PTV measurements". In: *Experiments in Fluids* 60.2 (2019), p. 29. ISSN: 1432-1114. DOI: 10.1007/s00348-019-2677-6.

[8] F. Taccaliti. "Aerodynamic and Structural Characterisation of a Hinged Folding Wingtip". PhD thesis. Delft University of Technology, 2022.

[9] D. F. Kurtulus, F. Scarano, and L. David. "Unsteady aerodynamic forces estimation on a square cylinder by TR-PIV". In: *Experiments in Fluids* 42.2 (2007), pp. 185–196. ISSN: 1432-1114. DOI: 10.1007/s00348-006-0228-4.

[10] W. Terra, A. Sciacchitano, and F. Scarano. "Aerodynamic drag of a transiting sphere by large-scale tomographic-PIV". In: *Experiments in Fluids* 58.7 (2017), p. 83. ISSN: 0723-4864, 1432-1114. DOI: 10.1007/s00348-017-2331-0.

[11] Ampaire. *Janes Ampaire Electric EEL*. Janes. URL: https://customer.janes.com/display/JAWAC114-JAWA (visited on 02/27/2023).

[12] Voltaero. Publisher: Online. URL: https://www.voltaero.aero/en/ (visited on 02/21/2023).

[13] J. Herzog. *Cessna 337D Super Skymaster N991DM OTT 2013 05*. 2017.

[14] J. Brandt and M. Selig. "Propeller Performance Data at Low Reynolds Numbers". In: *49th AIAA Aerospace Sciences Meeting including the New Horizons Forum and Aerospace Exposition*. 49th AIAA Aerospace Sciences Meeting including the New Horizons Forum and Aerospace Exposition. Orlando, Florida: American Institute of Aeronautics and Astronautics, 2011. ISBN: 978-1-60086-950-1. DOI: 10.2514/6.2011-1255.

[15] P. M. Sforza. "Chapter 10 - Propellers". In: *Theory of Aerospace Propulsion (Second Edition)*. Ed. by P. M. Sforza. Aerospace Engineering. Butterworth-Heinemann, 2017, pp. 487–524. ISBN: 978-0-12-809326-9. DOI: 10.1016/B978-0-12-809326-9.00010-5.

[16] MIT. *11.7 Performance of Propellers*. URL: https://web.mit.edu/16.unified/www/FALL/thermodynamics/notes/node86.html (visited on 10/04/2023).

[17] L. L. M. Veldhuis. "Propeller Wing Aerodynamic Interference". PhD thesis. Delt: Delft University of Technology, 2005.

[18] N. van Arnhem, R. de Vries, T. Sinnige, R. Vos, G. Eitelberg, and L. L. M. Veldhuis. "Engineering Method to Estimate the Blade Loading of Propellers in Nonuniform Flow". In: *AIAA Journal* 58.12 (2020), pp. 5332–5346. ISSN: 0001-1452, 1533-385X. DOI: 10.2514/1.J059485.

[19] W. D. Thompson. "Aerodynamics of the Cessna Tandem Twins". In: 3rd Annual Business Aircraft Conference (1967). Wichita, Kansas: Society of Automotive Engineers, 1967, p. 670243. DOI: 10.4271/670243.

[20] J. P. Campbell and T. A. Hollingworth. *The Effect on Stability and Control of a Pusher Propeller Behind Conventional Tail Surfaces as Determined by Tests of a Powered Model in the Free-Flight Tunnel.* Langley Field, Va: National Advisory Committee for Aeronautics NACA, 1943.

[21] M. Figat and P. Piątkowska. "Numerical investigation of mutual interaction between a pusher propeller and a fuselage". In: *Proceedings of the Institution of Mechanical Engineers, Part G: Journal of Aerospace Engineering* 235.1 (2021), pp. 40–53. ISSN: 0954-4100, 2041-3025. DOI: 10.1177/0954410020932796.

[22] D. J. Garmann and M. R. Visbal. "Interactions of a Trailing Vortex with a Downstream NACA0012 Wing". In: *47th AIAA Fluid Dynamics Conference*. 47th AIAA Fluid Dynamics Conference. Denver, Colorado: American Institute of Aeronautics and Astronautics, 2017. ISBN: 978-1-62410-500-5. DOI: 10.2514/6.2017-3319.

[23] C. Alba, A. Elham, B. German, and L. L. Veldhuis. "A Surrogate-Based Multi-Disciplinary Design Optimization Framework Exploiting Wing-Propeller Interaction". In: *18th AIAA/ISSMO Multidisciplinary Analysis and Optimization Conference*. 18th AIAA/ISSMO Multidisciplinary Analysis and Optimization Conference. Denver, Colorado: American Institute of Aeronautics and Astronautics, 2017. ISBN: 978-1-62410-507-4. DOI: 10.2514/6.2017-4329.

[24] T. Sarpkaya. "Vortex Breakdown in Swirling Conical Flows". In: *AIAA Journal* 9.9 (1971). Publisher: American Institute of Aeronautics and Astronautics, pp. 1792–1799. ISSN: 0001-1452. DOI: 10.2514/3.49981.

[25] A. M. Mitchell and J. Délery. "Research into vortex breakdown control". In: *Progress in Aerospace Sciences* 37.4 (2001), pp. 385–418. ISSN: 03760421. DOI: 10.1016/S0376-0421(01)00010-0.

[26] J. M. Delery. "Aspects of vortex breakdown". In: *Progress in Aerospace Sciences* 30.1 (1994), pp. 1–59. ISSN: 0376-0421. DOI: 10.1016/0376-0421(94)90002-7.

[27] T. Sarpkaya. "Effect of the Adverse Pressure Gradient on Vortex Breakdown". In: *AIAA Journal* 12.5 (1974), pp. 602–607. ISSN: 0001-1452, 1533-385X. DOI: 10.2514/3.49305.

[28] T. Sarpkaya. "On stationary and travelling vortex breakdowns". In: *Journal of Fluid Mechanics* 45.3 (1971). Publisher: Cambridge University Press, pp. 545–559. ISSN: 1469-7645, 0022-1120. DOI: 10.1017/S0022112071000181.

[29] J. H. Faler and S. Leibovich. "Disrupted states of vortex flow and vortex breakdown". In: *The Physics of Fluids* 20.9 (1977), pp. 1385–1400. ISSN: 0031-9171. DOI: 10.1063/1.862033.

[30] M. Raffel, C. E. Willert, F. Scarano, C. J. Kähler, S. T. Wereley, and J. Kompenhans. *Particle Image Velocimetry: A Practical Guide*. Cham: Springer International Publishing, 2018. ISBN: 978-3-319-68851-0 978-3-319-68852-7. DOI: 10.1007/978-3-319-68852-7.

[31] P. Cueto Corral, P. González Martínez, J. Miret Marco, and P. Valls Badia. *Laboratory Exercise Report - Flow Measurement Techniques*. Delft: Unpublished, 2022.

[32] G. E. Elsinga, F. Scarano, B. Wieneke, and B. W. van Oudheusden. "Tomographic particle image velocimetry". In: *Experiments in Fluids* 41.6 (2006), pp. 933–947. ISSN: 1432-1114. DOI: 10.1007/s00348-006-0212-z.

[33] F. Scarano. "Tomographic PIV: principles and practice". In: *Measurement Science and Technology* 24.1 (2013), p. 012001. ISSN: 0957-0233, 1361-6501. DOI: 10.1088/0957-0233/24/1/012001.

[34] B. Wieneke. "Volume self-calibration for 3D particle image velocimetry". In: *Experiments in Fluids* 45.4 (2008), pp. 549–556. ISSN: 1432-1114. DOI: 10.1007/s00348-008-0521-5.

[35] J. Bosbach, M. Kühn, and C. Wagner. "Large scale particle image velocimetry with helium filled soap bubbles". In: *Experiments in Fluids* 46.3 (2009), pp. 539–547. ISSN: 1432-1114. DOI: 10.1007/s00348-008-0579-0.

[36] G. C. A. Caridi, D. Ragni, A. Sciacchitano, and F. Scarano. "HFSB-seeding for large-scale tomographic PIV in wind tunnels". In: *Experiments in Fluids* 57.12 (2016), p. 190. ISSN: 0723-4864, 1432-1114. DOI: 10.1007/s00348-016-2277-7.

[37] D. E. Faleiros, M. Tuinstra, A. Sciacchitano, and F. Scarano. "Generation and control of helium-filled soap bubbles for PIV". In: *Experiments in Fluids* 60.3 (2019), p. 40. ISSN: 1432-1114. DOI: 10.1007/s00348-019-2687-4.

[38] R. J. Adrian. "Dynamic ranges of velocity and spatial resolution of particle image velocimetry". In: *Measurement Science and Technology* 8.12 (1997), pp. 1393–1398. ISSN: 0957-0233, 1361-6501. DOI: 10.1088/0957-0233/8/12/003.

[39] D. Schanz, S. Gesemann, and A. Schröder. "Shake-The-Box: Lagrangian particle tracking at high particle image densities". In: *Experiments in Fluids* 57.5 (2016), p. 70. ISSN: 0723-4864, 1432-1114. DOI: 10.1007/s00348-016-2157-1.

[40] LaVision. *Flow Master Shake the Box (4D PTV) Manual*. 2022.

[41] J. F. G. Schneiders, R. P. Dwight, and F. Scarano. "Time-supersampling of 3D-PIV measurements with vortex-in-cell simulation". In: *Experiments in Fluids* 55.3 (2014), p. 1692. ISSN: 1432-1114. DOI: 10.1007/s00348-014-1692-x.

[42] J. F. G. Schneiders and F. Scarano. "Dense velocity reconstruction from tomographic PTV with material derivatives". In: *Experiments in Fluids* 57.9 (2016), p. 139. ISSN: 1432-1114. DOI: 10.1007/s00348-016-2225-6.

[43] I. P. Christiansen. "Numerical simulation of hydrodynamics by the method of point vortices". In: *Journal of Computational Physics* 13.3 (1973), pp. 363–379. ISSN: 0021-9991. DOI: 10.1016/0021-9991(73)90042-9.

[44] Y. J. Jeon, M. Müller, and D. Michaelis. "Fine scale reconstruction (VIC#) by implementing additional constraints and coarse-grid approximation into VIC+". In: *Experiments in Fluids* 63.4 (2022), p. 70. ISSN: 1432-1114. DOI: 10.1007/s00348-022-03422-9.

[45] A. Ramesh. "Evaluating the feasibility of studying propeller-wing interaction through ground-based high-speed experimental taxi-tests". PhD thesis. Delft: TU Delft, 2022.

[46] C. Jux, F. Scarano, and A. Sciacchitano. "Aerodynamic pressure reconstruction on generic surfaces from robotic PIV measurements". In: *Proceedings of the 13th International Symposium on Particle Image Velocimetry* (2019). Publisher: Universitat der Bundeswehr Munchen. DOI: 10.18726/2019_3.

[47] B. W. van Oudheusden. "PIV-based pressure measurement". In: *Measurement Science and Technology* 24.3 (2013). Publisher: IOP Publishing, p. 032001. ISSN: 0957-0233. DOI: 10.1088/0957-0233/24/3/032001.

[48] J. D. Anderson. *Fundamentals of aerodynamics*. Sixth edition. McGraw-Hill series in aeronautical and aerospace engineering. New York, NY: McGraw Hill Education, 2017. 1130 pp. ISBN: 978-1-259-12991-9.

[49] D. Ragni, B. W. van Oudheusden, and F. Scarano. "3D pressure imaging of an aircraft propeller blade-tip flow by phase-locked stereoscopic PIV". In: *Experiments in Fluids* 52.2 (2012), pp. 463–477. ISSN: 0723-4864, 1432-1114. DOI: 10.1007/s00348-011-1236-6.

[50] P. J. Pritchard. *Fox and McDonald's Introduction to Fluid Mechanics*. Eight Edition. John Wiley & Sons, 2011. ISBN: ISBN-13 978-0-470-54755-7.

[51] R. Smedts. "Fixed pitch propeller performance". PhD thesis. Eindhoven: Eindhoven University of Technology, 2015.

[52] F. M. A. Mitrotta, J. Sodja, and A. Sciacchitano. "On the combined flow and structural measurements via robotic volumetric PTV". In: *Measurement Science and Technology* 33.4 (2022), p. 045201. ISSN: 0957-0233, 1361-6501. DOI: 10.1088/1361-6501/ac41dd.

[53] N. Agüera, G. Cafiero, T. Astarita, and S. Discetti. "Ensemble 3D PTV for high resolution turbulent statistics". In: *Measurement Science and Technology* 27.12 (2016). Publisher: IOP Publishing, p. 124011. ISSN: 0957-0233. DOI: 10.1088/0957-0233/27/12/124011.

[54] F. M. A. Mitrotta. "Experimental Fluid-Structure Interaction of a Flexible Plate Under Gust Excitation: A Wind-tunnel Investigation by Means of Robotic Volumetric PIV". In: (2020).

[55] A. De paula. "The airfoil thickness effects on wavy leading edge phenomena at low Reynolds number regime". PhD thesis. 2016.

[56] L.-Z. Wang, C.-Y. Guo, Y.-M. Su, and T.-C. Wu. "A numerical study on the correlation between the evolution of propeller trailing vortex wake and skew of propellers". In: *International Journal of Naval Architecture and Ocean Engineering* 10.2 (2018), pp. 212–224. ISSN: 20926782. DOI: 10.1016/j.ijnaoe.2017.07.001.

[57] R. Gordnier and M. Visbal. "Numerical simulation of the impingement of a streamwise vortex on a plate". In: *28th Fluid Dynamics Conference*. Fluid Dynamics and Co-located Conferences. American Institute of Aeronautics and Astronautics, 1997. DOI: 10.2514/6.1997-1781.

A

Wind tunnel test matrix

Test matrices displaying the tested values with the expected rotational velocity measured at the lab and the actual calculated value in Hz through the spectral analysis. Beware, the frequency value in Hz has to be divided into two as it represents the calculated value with both blades.

Table A.1: Test matrix without wing.

Run	Lab ω [RPM]	u_0 [m/s]	Frequency [Hz]
1.1	4200	5.1	141.6
1.2	5250	5.1	175.7
1.3	6000	5.1	200.2
1.4	5250	3	175.7
1.5	5250	8	175.7

Table A.2: Test matrix with wing.

Run	Lab ω [RPM]	u_0 [m/s]	α [°]	Frequency [Hz]
2.1	5250	5.1	0	175.7
2.2	5250	5.1	5	175.7
2.3	5250	5.1	10	175.7
2.4	5250	5.1	-5	175.7
2.5	5250	5.1	-10	-
2.6	5200	3	5	-
2.7	5200	8	5	-
2.8	4200	5.1	5	-
2.9	6000	5.1	5	-
2.10	5200	5.1	90	200.2